International Committee for Future Accelerators

Sponsored by the Particles and Fields Commission of IUPAP

Beam Dynamics Newsletter

No. 67

Issue Editor:
Y. Funakoshi

Editor in Chief:
W. Chou

August 2015

Contents

1   Foreword

1.1   From the Chair

Weiren Chou, Fermilab
Mail to: chou@fnal.gov

The International Committee for Future Accelerators (ICFA) met on August 19, 2015 at Ljubljana, Slovenia. Joachim Mnich, Research Director of DESY and ICFA Chair chaired the meeting.

John Womersley, chair of *The Funding Agencies for Large Colliders* (FALC) gave a report. A major topic was the status of ILC activities in Japan and a recent interim report published by the Advisory Panel, which was formed by the Ministry of Education, Science and Technology (MEXT) of Japan in May 2014. (http://www.mext.go.jp/component/b_menu/shingi/toushin/__icsFiles/afieldfile/2015/08/05/1360596_3.pdf) The report made three recommendations. Among them, a main point was that in order to justify the huge investment that would be required by the ILC project, a clear vision on the discovery potential of new particles has to be shown in addition to precision measurements of the Higgs boson and the top quark. Cost sharing with international partners including European countries and the United States is another major issue. The report also emphasizes the importance to have general understanding on the project by the public and science communities. From the report, it appears that no decision is possible until the LHC Run 2 data are available.

In addition to the ILC, future circular energy frontier colliders will be discussed at FALC, and neutrino programs are already a discussion topic.

IUPAP is forming an interim working group to recommend a mandate and membership for the proposed IUPAP Working Group on Accelerator Science. Several organizations have been asked to suggest members of the interim group, including ICFA, APS DPB, ACFA, IUPAP C12, etc.

As the designs of future colliders (ILC, CLIC, CEPC, FCC, etc.) and accelerators (ESS, ADS, IFMIF/EVEDA, etc.) require large power consumption and thus large operating costs, there is a proposal to form a new ICFA panel on Sustainable Accelerator and Collider Infrastructure to systematize and develop figures of merit, and also evaluate promising R&D activities which could lower power consumption. The panel mandate and membership will be discussed at the next ICFA meeting.

The ICFA Beam Dynamics Panel requested approval of the 55th ICFA Advanced Beam Dynamics Workshop on High-Intensity and High Brightness Hadron Beams (HB2016), which will take place July 3-8, 2016 at Scandic Hotel in Malmö, Sweden and be hosted by the European Spallation Source (ESS). ICFA approved this workshop.

The study on the Future Circular Colliders (FCC) has made good progress. There are more than 50 MOUs signed between CERN and other world-wide institutions. A milestone of this study will be to demonstrate a 16 Tesla superconducting magnet by the end of 2018. Meanwhile, the Preliminary Conceptual Design Report of a future collider in China, CEPC-SPPC, has been completed with ~500 authors world-wide. It forms the basis for a funding proposal to the Chinese government. Although it is not

known when a decision will be made by the government, positive indications have been received on some funding for continued studies.

The 9th International Accelerator School for Linear Colliders co-organized by the Linear Collider Collaboration (LCC), ICFA Beam Dynamics Panel and TRIUMF will take place Oct 26 – Nov 6, 2015 in Whistler, British Columbia, Canada. An updated curriculum and a list of teachers can be found in Section 4.1. All lecture slides will be made available on the school web site (http://www.linearcollider.org/school/2015/).

The editor of this issue is Dr. Yoshihiro Funakoshi, a panel member and a senior scientist at KEK, Japan. The theme is "*Future e+e- Ring Colliders.*" He collected 8 well-written articles, which cover four circular e+e- colliders: DAΦNE, SuperKEKB, CEPC and FCC-ee. The selection of this theme is timely as there is a world-wide renewed interest in our community in future circular colliders. Another issue dedicated to future circular hadron colliders (FCC-pp and SPPC) will appear in April 2017.

In this issue there is also an ICFA mini-workshop report (*High Field Magnets for pp Colliders*). I want to thank Yoshihiro for editing a newsletter of great value and good quality for the accelerator community.

1.2   From the Editor

Yoshihiro Funakoshi
KEK, 1-1 Oho, Tsukuba, Ibaraki 305-0801, Japan
Mail to: yoshihiro.funakoshi@kek.jp

I would like to thank all authors who have contributed to this issue of the ICFA Beam Dynamics Newsletter. The theme of this issue is "*Future e+/e- Ring Colliders*". The first electron-positron interactions were observed in 1964 with AdA. Half a century has passed since then. A number of glorious physics outcomes have been achieved with the e+/e- colliders and the technologies for this type of colliders have been well matured. However, the potential of the e+/e- colliders is very rich and there still remains some room to open our new horizons. Based on the success of PEP-II and KEKB, SuperKEKB aims at the luminosity near 10^{36} cm^{-2} s^{-1}. CEPC and FCC-ee will aim at the beam energy of 120 or 175 GeV. Outlines and challenges which we have to struggle with in these luminosity-extreme or energy-extreme machines are summarized in this issue. Another article reports the status of DAΦNE. Of a particular interest is the experiment on the crab-waist scheme at DAΦNE. This scheme is under study in the design of the future colliders.

In the section on workshop and conference reports, an ICFA Mini-workshop on "High Field Magnets for pp Colliders" is reported. This workshop was motivated by the upcoming needs of the 20-T level magnets for recently proposed circular pp collider, mainly CEPC-SPPC which is assumed to be constructed in the same tunnel as the CEPC e+/e- collider.

2   FUTURE e⁺/e⁻ RING COLLIDERS

2.1   DAΦNE Consolidation Program and Operation with the KLOE-2 Detector

Catia Milardi, David Alesini, Maria Enrica Biagini, Simone Bini, Manuela Boscolo, Bruno Buonomo, Sergio Cantarella, Antonio De Santis, Giampiero Di Pirro, Giovanni Delle Monache, Alessandro Drago, Luca Foggetta, Oscar Frasciello, Alessandro Gallo, Riccardo Gargana, Andrea Ghigo, Francesco Guatieri, Susanna Guiducci, Franco Iungo, Carlo Ligi, Andrea Michelotti, Luigi Pellegrino, Ruggero Ricci, Ugo Rotundo, Giancarlo Sensolini, Angelo Stella, Alessandro Stecchi and Mikhail Zobov
LNF-INFN, Via E. Fermi, 40 I-00044 Frascati (Rome), Italy

Dmitry Shatilov
BINP SB RAS, Novosibirsk, Russia

Alexander, Valishev
Fermilab, Batavia, USA

Mail to: catia.milardi@lnf.infn.it

2.1.1   Introduction

After a long preparatory phase, including a wide hardware consolidation program, the Italian lepton collider DAΦNE, is now systematically delivering data to the KLOE-2 experiment.

In approximately 200 days of operation 1 fb^{-1} has been given to the detector limiting the background to a level compatible with an efficient data acquisition.

Instantaneous and maximum daily integrated luminosity measured, so far, are considerably higher with respect to the previous KLOE runs, and are: $L_{ist} \sim 2.0 \times 10^{32}$ cm^{-2}s^{-1}, and $L_{\int day} \sim 12.5$ pb^{-1} respectively.

A general review concerning refurbishing activities, machine optimization efforts and data taking performances is presented and discussed.

The DAΦNE [1] accelerator complex consists of a double ring lepton collider working at the c.m. energy of the Φ-resonance (1.02 GeV) and an injection system. The collider is based on two independent rings, each ~97 m long, sharing an interaction region, where a detector is installed. The full energy injection system including an S-band linac, 180 m long transfer lines and an accumulator/damping ring provides electron–positron injection in topping-up mode during luminosity delivering.

Long radiation damping times, low collision energy and high stored currents make achieving high luminosity at DAΦNE a quite challenging task. In fact, best performances in terms of luminosity have been attained only after several radical modifications [2,3], with respect to the original design, and after implementing the new *Crab-Waist* collision scheme [4,5,6].

The highest instantaneous luminosity, $L = 4.5 \times 10^{32}$ cm^{-2}s^{-1}, has been measured at DAΦNE during a test run with a table-top experimental apparatus without solenoidal field. Such luminosity, two orders of magnitude higher than the best ever achieved at other colliders working at the same c.m. energy, opened new perspectives for the KLOE experiment [7]. Integrating the high luminosity collision scheme with a large detector, having a strongly perturbing solenoidal field, posed new challenging issues concerning layout, beam acceptance and coupling correction. A new interaction region has been designed, and has been equipped with a transverse betatron correction mechanism, based on rotated quadrupoles and anti-solenoids, independent for the two beams [8].

Operations for the KLOE detector have been organized in two stages. First the new interaction region has been installed, tested and the luminosity, already measured in the pre-*CrabWaist* configuration, has been reproduced and slightly improved, $L = 1.52 \times 10^{32}$ cm^{-2}s^{-1} [9]. Then, in the first seven months of 2013, the accelerator complex has been shut down again mainly to upgrade the detector, KLOE-2, which in view of a higher luminosity, had extended its physics search program, and to implement a general consolidation program concerning the machine hardware.

The KLOE-2 setup includes new tracking and calorimeter devices close to the interaction region. A very light tracker, consisting of a cylindrical gas electron multiplier, has been installed in the tight space between the drift chamber and the spherical beam pipe. Crystal calorimeters have been inserted in front of the collider low-β quadrupoles, thus increasing the acceptance for photons emitted under a very low angle, a key issue for rare decay studies. Dedicated detectors have been inserted one inside the experimental apparatus and the other after the first dipole in the long arc in each ring in order to study scattered electron and positron produced in γ-γ reactions.

Such upgrade imposed the extraction of the Interaction Region from inside the detector and the disassembly of the low-β section. As a consequence the collider had to be commissioned again nearly from scratch. After achieving reasonable performances, an eight months period has been dedicated to the optimization of the experiment data taking. In this phase all the activities have been addressed to demonstrate that DAΦNE was able to provide high rate, high quality physics events to KLOE-2 experiment, in a stable and reproducible way over the long term.

2.1.2 DAΦNE Consolidation Program

When KLOE was reinstalled on the collider Interaction Region (IR), at the end of 2010, the DAΦNE infrastructure had been working since more than 17 years.

Commissioning, aimed at setting up the collider, was affected by many, relevant and time consuming faults, and pointed out some shortcomings in the interaction region mechanical design.

In fact, several sub-systems, relying on obsolete technologies, suffered from spare part shortage. Some components got seriously damaged. It is the case of some bellows in the IR, which had lost electrical continuity causing anomalous beam induced heating of one of the two defocusing quadrupoles, resulting in a harmful random vertical beam tune-shift. The mechanical structure of the Interaction Region (IR) had shown to be inadequate to steadily support the heavy defocusing quadrupoles cantilevered inside the detector. As a consequence the two beams were oscillating in phase at 10 Hz in the vertical plane.

In this context, the shutdown scheduled in 2013, intended mainly to install new detector layers inside the KLOE detector (KLOE-2) [10], offered a very convenient opportunity to undertake a wide consolidation program involving several subsystems as well as to revise the IR mechanical design [11].

Many other machine improvements have been implemented during the following operation periods, profiting from season and maintenance shutdowns, and the unexpected faults, whose occurrence is, anyhow, diminishing in number and importance.

2.1.2.1 *Mechanical Upgrade*

A major effort has been done to upgrade the Interaction Region mechanical structure and the vacuum chamber around the Interaction Point.

The vacuum chamber around the Interaction Point (IP) has been replaced. The new one has tapered transition between the thin ALBEMET sphere and the Al beam pipes, and includes reshaped bellows with new designed RF contacts, see Fig. 1.

Figure 1: IP spherical vacuum chamber.

Replacing the bellows solved the low-β defocusing quadrupole heating problems, recovering working point stability during operations.

Two cooling pipes have been added on the tapers and new semi-cylindrical thin (35 μm) beryllium shields have been placed inside the sphere. Two additional Beam Position Monitors (BPM) have been installed on both sides of the IP, for a more accurate beams overlap and to perform transverse betatron coupling studies.

The IP chamber and the low-β defocusing quadrupoles are suspended at the two sides of the detector. The whole support structure is critical for the stability of the assembly. The design of supports, of the vacuum chambers and equipment, as well as for the magnetic and diagnostic elements have been revised to host the new detector components and the hugely increased number of cables and pipes for gas and coolant, as well as to stand additional weight, see Fig. 2, and improve alignment precision.

Figure 2: The DAΦNE IR with the new detector layers ready to be inserted in KLOE-2.

In particular, a pair of additional carbon fiber composite legs has been designed and superimposed to the existing ones, and some rubber pads previously inserted below the cradle support have been removed, to strengthen the structure and increase its rigidity, see Fig. 3.

Figure 3: Additional carbon fiber composite legs (central black poles) superimposed to the original low-β support structure.

As a result the spectrum of the vertical beam oscillation has changed. The main harmonic has been shifted toward higher frequencies, ~15 Hz, and its amplitude reduced by about a factor three, see Fig. 4 showing the e^+ and the e^- oscillation spectra respectively, before and after inserting the new legs.
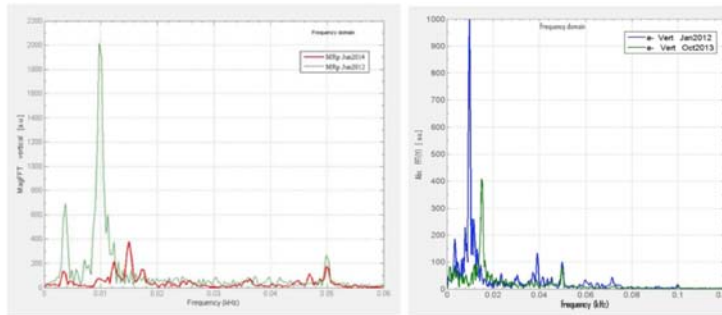
Figure 4: Natural e$^+$ beam oscillation spectrum around the nominal orbit as recorded at the BPBPL201 before (green left) and after (red left) revising the low-β support structure. Same analysis for the e$^-$ beam oscillation spectrum as recorded at the BPBEL201 before (blue right) and after (green right) the upgrade.

About the steelwork structure around the IR, some reinforcing plates have been added to the H-shaped girders, including new grounding anchorage with adjustable bolts for the tail of the girders itself.

The screw holes in the jaw of four scrapers, installed two in the e$^-$ and two in the e$^+$ ring at either ends of the IR, have been filled by adding shielding copper extensions, in order to avoid HOM trapping. Since after having detected some anomalous heating events in operations, a visual inspection of the components, revealed clear signs of discharges. Moreover the jaw limit switches have been moved to increase the collimator stroke, thus achieving a more efficient suppression of the background hitting the experimental detector. In total the jaw insertion length has been increased by 2.5 mm, corresponding to a 30% increase with respect to the previous stroke.

Several other developments have been implemented:

- More and better placed CCR holes for alignment have been added.
- Newly designed mechanics (cams and kinematics) now allows a better control of the angular rotation of the low-β focusing quadrupoles from outside the detector.
- Temperature probes have been added on the Interaction Region vacuum chamber.
- Toroidal shields have been added around the IP to reduce the background hitting the detector.
- New Beam Position Monitors have been installed along the rings.

2.1.2.2 *Ancillary Plants Control System Revamping*

The control system of several utility plants serving the accelerator has been renovated. The systems involved have been the Fluids plants (cooling and HVAC, compressed air), the RF plants, the Vacuum plants and the safety system of the magnets over-temperature control subsystem. 15 PLC substations have been replaced. Control system of the Fluids plants has been re-engineered, substituting the whole PLC system.

The control logic of the new system has been modified to take into account the relevant reduction of the AC power demand of the largest magnets (Wigglers, Septa). Replacement of obsolete items drove the change of the PLCs controlling the Vacuum plants (valves and gauges) and the RF plants and interlocks (klystrons, cavities,

circulators and loads), but in this case the dismissed equipments have been kept to be used as spare parts for the magnets over temperature control subsystem.

In this refurbishment also the SCADA has been renewed allowing the remote control of all the subsystems to facilitate and speed up faults diagnosis during the current machine operation. The Supervisor was developed with Movicon SCADA and customized upon specific requests.

2.1.2.3 *High Pressure Cooling System Optimization*

The water flow rate in the high pressure cooling system serving the wiggler magnets has been reduced by a 33%, by adding a variable frequency drive in the circuit. This allowed definitively avoiding destructive effects induced by cavitation, eroding the copper of the wiggler coils and leading to water leakage. Recovering from this kind of faults required, in general, 2-3 days stop in the operations, and forced to shut down some dipoles and all the wigglers in the main rings in order to access and solder the damaged coils. In addition to the damage in terms of machine uptime, such problems were deteriorating permanently the wiggler coils threatening the magnets long term operativeness.

Cooling system optimization has been possible since in 2010 the poles disposition of the DAΦNE wigglers has been revised [12] achieving, among other, a considerably increase of the magnetic field obtained at a given current. As a consequence the nominal operation current of the wigglers has been remarkably reduced, which allowed, in turn, to relax the cooling system parameters.

2.1.2.4 *Control System Upgrade*

The DAΦNE Control System (DCS) has been deeply modified in order to dismiss obsolete components and improve responsiveness and reliability.

In its original design, the system live data resided in a central VME shared memory and the communication channels were based on point-to-point optical links, realized with VME boards. This architecture granted high bandwith and low latency but – on the other hand – was heavily hardware dependent, requiring the use of VME embedded processors for any purpose.

The new design of the DCS hinges on the redirection of the whole data flow to the Ethernet network and the adoption of an *Object Caching* service (*Memcached*) for hosting the live data. This utterly decouples software services from hardware, opening the system to different hardware choices.

Most of the front-end VME boards (serial communication boards, DAQs, ADCs, etc.) have been replaced by network devices, which allowed for the porting of many control programs to remote Linux virtual machines. In particular, the adoption of *serial device servers* instead of serial communication boards, permitted to increase the number of daisy chain lines (RS-422) employed in connecting the magnets' power supplies and consequently to shorten the machine switch (from positrons to electrons and vice-versa).

The DCS upgrade also aimed at replacing the original distributed front-end VME processors (forty-five 68030 custom boards, running MacOS 7) with Intel boards, running Linux, see Fig. 5. At the present, 19 Virtual Machines and 7 new Linux VME processors host 70 control processes and only 10 of the former VME processors are left.
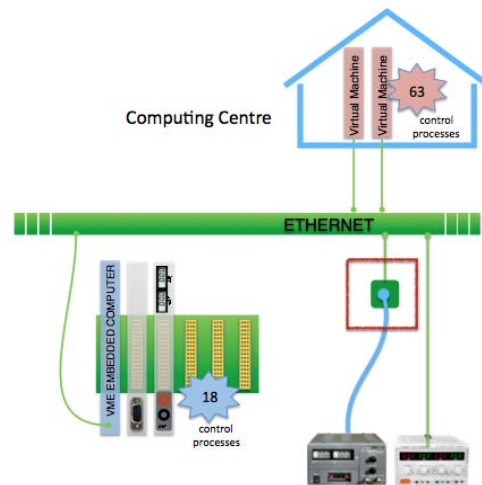
Figure 5: DAΦNE control system new layout.

New Linux servers have been setup for the core services (NFS, DHCP, diskless boot, MySQL, memcached) and for the SunRay™ thin-clients employed as consoles. The system hosting the virtual machines has been set-up with Red Hat Cluster Suite and XEN 3.2014.

The Network Uplink with the Computing Centre has been enhanced (10 G) in order to improve the command/data flow among virtual machines and front-end devices.

The upgrade has also concerned both the *hardware* and the *software* of many front-end systems, in order to take advantage of the new DCS structure. The DAΦNE subsystems that have gone through major changes are: RF Slow Control, Main Ring Scrapers, Programmable Delays, Power Supplies, Main Rings and Damping Ring Kickers, Beam Charge Monitors, Spectrometer, Vacuometers, Vacuum Pumps and Clearing Electrodes.

After the upgrade, the DCS proved to be performable and reliable and its overall uptime - in real operating condition - significantly increased.

2.1.2.5 *Cryogenic Plant*

The cryogenic plant, serving the superconducting solenoid of the experimental apparatus and the four anti-solenoids installed on the collider rings, has been completely overhauled and some specific parts have been mended or replaced. Some o-rings sealing in the helium transfer lines have been replaced with soldered connections. Two partially damaged Joule-Thomson needle valves have been reworked. A remotely controlled pneumatic valve has been added in the liquid nitrogen line. PT100 thermometers were installed in the nitrogen line of the anti-solenoids transfer lines, close to the gas flow controllers. The obsolete remote PC for the plant control has been replaced as well as the operator interface panel. The listed activities were aimed at preventing accidental freezing at the controller level, and at ensuring remote procedures for refilling the anti-solenoids. Nevertheless, other long shutdown periods have been necessary, afterwards, to recover from an oil contamination at the level of the cold-box, and to undertake an extraordinary maintenance of the compressor, which is working since 750000 hours, well beyond its expected working lifetime.

2.1.2.6 *Linac*

All the LINAC components have been overhauled paying special attention to the four RF power plants. In this context several exhausted components such as filter capacitors, thyratrons and high power pulse discrete elements have been replaced, and a new designed RF driver system has been installed aiming at achieving a better stability in terms of delivered power.

New vacuum pumps and ancillaries have been added on the four main waveguides downstream the SLEDs, in order to reduce discharge occurrences.

Concerning the RF-vacuum devices in the LINAC accelerating sections, the residual pressure considerably improved by replacing all the RF loads. The vacuum safety system gating valves and some in-vacuum diagnostic elements such as flags and BPMs have been also replaced.

All the ceramic windows, placed downstream the klystron ones to decouple the LINAC vacuum, were almost at the end of their operating-life and have been preventively substituted.

As a special case, the RF power plant 'D', driving the last four accelerating sections, required an extraordinary mending effort, even beyond the 2013 shutdown. Several parts had to be replaced such as: the klystron, the waveguide elbow interfacing the klystron, the SLED and many ancillary components.

Some bugs in the Helmholtz Coil power supplies have been detected and fixed. The PLC control system has been upgraded, and its parts underwent an accurate revision involving: water ducts, flux-meters and water pumping system, leading to replacement of many components. The LINAC control system has been revised and upgraded in order to be compliant with the renewed Ethernet architecture (new routers and VLAN relying on fiber connections) and to profit from new network features. In this context a new control application, based on dedicated multiplexed DAQ, has been designed and implemented for the 14 LINAC BPMs.

2.1.2.7 *Other Consolidation Activities*

Many other remarkable activities have been done.

The magnetic field of the *IR defocusing quadrupoles* has been measured detecting discrepancies of the order of few % only with respect to *ab initio* characterization.

The 32 power supplies powering a family of corrector magnets have been replaced with updated devices.

The HV power supplies polarizing the *e-cloud clearing electrodes* have been substituted with devices providing twice the original voltage and having negative polarity. This allows achieving a complete neutralization of the *e-cloud* generated by a positron current of the order of ~1. A, and reducing the generator delivered current.

More robust *feedthroughs* have replaced the ones originally used for the electrodes installed inside the wiggler magnets of the e^+ ring.

Two *new vacuum chambers* have been built and installed near the injection sections of both rings. Each new beam pipe is carrying eight button BPMs to be used for orbit measurements and as feedback pickups.

One of the two klystrons, stored in the DAΦNE hall to serve, in the case, as a spare part for the RF plants of the DAΦNE main rings, lost vacuum insulation.

A thorough analysis pointed out that purchasing a spare tube, same as the damaged one, was considered unworthy since costs and time required for this acquisition resulted

to be simply unaffordable. The only viable way to recover the broken tube consisted in finding and repairing the vacuum leakage in house. The repaired tube has been installed in the e⁻ ring power plant in winter 2015 to replace another broken unit, and after a brief period of conditioning, it has reached the nominal performance required for running the machine and it is presently in operation.

Concerning the bunch-by-bunch feedback systems, a *new horizontal kicker* with a doubled stripline length has replaced the original one on the electron ring, providing larger shunt impedance at the low frequencies typical of the unstable modes. This allows doubling the feedback damping rate for the same setup (gain, power amplifier, etc.). A dedicated virtual LAN for all feedback units provides a faster real-time data processing. Hardware has been upgraded and Linux software updated to be compliant with the most recent netware and software releases.

2.1.3 DAΦNE Main Rings Tuning

Operations, in general, received powerful impulse from the consolidation activities.

The work done on the IR mechanical structure, for instance, had a huge impact on many main rings crucial issues such as: impedance budget, optics and beam dynamics. Similarly the numerous mending actions involving almost all the DAΦNE subsystems have been essential in restoring a good uptime, a fundamental prerequisite to undertake reliable measurements and for fine tuning. In a word, without these upgrades configuring machine for collisions, tuning luminosity and, as a matter of fact, testing the Crab-Waist collision scheme with a large detector would have not been possible.

2.1.3.1 *Colliding Rings Optics*

The IR layout [8] implementing Crab-Waist collisions for the KLOE-2 detector includes a low-β section based on permanent magnet quadrupole doublets. The quadrupoles are made of SmCo alloy: the first one from the IP has a gradient of 29.2 T/m, the second 12.6 T/m. The first is horizontally defocusing and is shared by the two beams; due to the off-axis beam trajectory, it increases the horizontal crossing angle from ~25 to ~ 50 mrad. In addition two anti-solenoids are installed symmetrically with respect to the IP in each ring. The new ring optics account for all these features, and, at the same time, assure suitable betatron oscillation amplitude at the *Crab-Waist* Sextupoles (*CW*-Sextupoles), and proper phase advance [4] between these magnets and the IP.

2.1.3.2 *Transverse Betatron Coupling Correction*

The permanent magnet focusing quadrupoles of the low-β are rotated around their longitudinal axes as well as the three electromagnetic quadrupoles installed on each one of the four IR branches. These rotations, together with the four anti-solenoids, provide an efficient compensation mechanism for the coupling due to the solenoid of the experimental apparatus [8]. Moreover the rotations of the low-β focusing quadrupoles, independent for the two rings, are used for transverse betatron coupling fine tuning. The procedure relies on transverse beam size measurements as evaluated by a calibrated synchrotron light monitor, and he response matrix measured by varying corrector magnets. Presently a very good coupling correction has been achieved for the e⁺ beam, κ ~ 0.4%, with all the skew quadrupoles off, while a further optimization is needed for

the e$^-$ beam. Nevertheless by tuning the skew quadrupoles a transverse betatron coupling in the range 0.2% ÷ 0.3% can be achieved in both rings [13].

2.1.3.3 *Main Rings Optics and Working Point Studies*

Main rings optics studies profited a lot from working point stabilization, which has been recovered by replacing broken bellows, close to the IP. This was causing anomalous heating (up to 50 ÷ 60 ^{0}C) in the low-β defocusing quadrupole downstream the e$^-$ beam, and in turn, a random significant oscillation of the tunes in the main rings, especially the vertical one. Fixing this aspect allowed to undertake reliable and systematic machine measurements, aimed at methodical optimization of main rings lattice, working point and collisions.

Working point simulations at DAΦNE are performed by using the *Lifetrack* simulation code. *Lifetrack* is a weak-strong particle tracking code, developed for simulating equilibrium density distributions in lepton colliders [14]. The fully symplectic 6D treatment of beam-beam interaction allows to simulate configurations with very large crossing angle, and crabbing of weak and strong bunches either. Main code features, in the equilibrium distribution case, allows computing: 3-D density of the weak beam, specific luminosity, beam lifetime, dynamical aperture and Frequency Map Analysis [15]. Moreover, latest code developments implement a detailed machine lattice model, via element-by-element tracking in thin lens approximation. The optics description for both weak and strong beam can be imported directly from MAD-X [16] model files. Such approach enables to properly treat element misalignments and related orbit distortions, chromatic aberrations, lattice nonlinearities, betatron and synchrobetatron coupling, with the same formalism used for ordinary optics simulations.

The working points initially devised for the DAΦNE main rings were: $\nu_x^- = 5.098$, $\nu_y^- = 5.164$ and $\nu_x^+ = 5.1023$, $\nu_y^+ = 5.139$, which, according to simulations, provide good luminosity and lay in a rather large stable area. In fact, with this optics a luminosity of 1.88×10^{32} has been achieved.

This configuration, in its early stage, when the highest achievable luminosity was at last 1.5×10^{32} cm^{-2}s^{-1}, has been used for a test run using 10 colliding bunches. The study, see Fig. 6, lasted for about 10 hours, during which a peak luminosity of $L = 2.55 \times 10^{31}$ cm^{-2}s^{-1} has been repeatedly measured with currents of the order of $I^- \sim 0.096$ A, and $I^+ \sim 0.126$ A, without any particular optimization effort. Since single bunch current is comparable with the one used during nominal high current, high number of bunches operations, this experiment provides a nice environment to disentangle the main beam-beam contribution to the maximum achievable luminosity, from the components due to collective effects dominating the DAΦNE beam dynamics. In the specific case the measurement indicates that a luminosity of the order of $L = 2.5 \times 10^{32}$ cm^{-2}s^{-1} is in principle achievable.
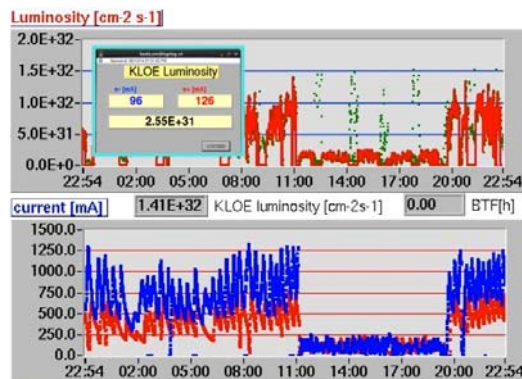
Figure 6: 10 bunches luminosity test.

In spite of the positive achievements, still some limitation persisted, affecting mainly the e$^-$ beam in terms of injection efficiency, beam lifetime and e$^-$ beam induced background. New simulation outlined that moving the e$^-$ ring tunes to new values ($\nu_x^- = 5.13$, $\nu_y^- = 5.17$) would have led to improve dynamical aperture by 2-3σ, suppressing at the same time the growth of the bunch vertical tail and achieving a moderate increase in terms of specific luminosity too [17]. Changing the working point required to compute and implement a new optics, which, in turn, imposed to optimize the transverse feedback systems. The new configuration led to very positive results. The contribution of the e$^-$ beam to the total machine background was reduced by 30% and 20% [18], as can be seen from the left graph in Fig. 7, which shows a comparison between machine background hitting the KLOE-2 calorimeter, in the region around the exit of the electron beam, as a function of the instantaneous luminosity. The KLOE-2 trigger rate also profited from the new electron ring optics, as it is evident from the right plot in Fig. 7. The observed reduction of the trigger rate had a twofold positive effect. First, the data throughput decreased, since the contribution of the machine background hitting the KLOE-2 sub-detectors to the event size is smaller, and because the events acquisition rate is smaller. Second, the dead time induced by the activation of the KLOE-2 trigger is smaller, allowing for a more efficient data taking.

In addition to the background reduction, after short period spent on collider fine-tuning, the best peak luminosity, $L_{peak} = 2.0 \times 10^{32}$ cm^{-2} s^{-1}, and the best daily integrated luminosity, 12.5 pb^{-1}, ever measured with the KLOE-2 detector have been attained in a stable and reproducible way. Repeating the 10 colliding bunches test would be very instructive, but for now the data taking schedule imposes drastic limits on the time available for machine studies.
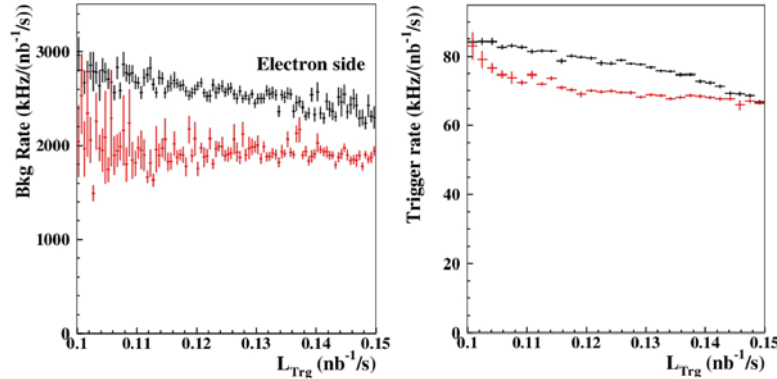
Figure 7: Comparison between machine background hitting the KLOE-2 calorimeter, in the region around the e⁻ beam exit, as a function of instantaneous luminosity (left), and KLOE-2 trigger level (right) for previous (black dots) and current (red squares) e⁻ machine working point. KLOE-2 trigger provides the instantaneous luminosity measurement. The reduction of background rate as a function of luminosity for the previous DAΦNE optics is mainly due to dynamical effect induced by the high current (~1A) needed to reach high luminosity. The reduction in the KLOE-2 trigger rate observed in the right panel has a similar behaviour as the background rate.

2.1.4 Beam Dynamics

Machine operation at high current strongly depends on vacuum conditions. Since the main rings beam pipe has been opened, repeatedly, in several sections a quite long time has been spent to recover a reasonable dynamic vacuum level.

Highest currents stored, so far, are 1.7 A and 1.2 A, for e⁻ and e⁺ beam, respectively. These currents are the highest ever achieved after installing the new IR for the KLOE-2 detector, based on the *Crab-Waist* collision scheme.

The three independent bunch-by-bunch feedback systems [19] installed on each DAΦNE ring are continuously working being essential for high current multi-bunch operations. The e⁺ vertical feedback is now using a new ultra-low noise front-end module, designed in collaboration with the SuperKEKB feedback team, aimed at reducing the noise contribution to the transverse vertical beam size in collision.

Presently beam dynamics in the e⁺ ring is clearly dominated by the e-cloud induced instabilities, whose effects are suppressed by means of powerful bunch-by-bunch transverse feedback systems [20], by solenoids wound all around the straight sections and by on purpose designed electrodes [21] installed inside dipole and wiggler vacuum chambers. The electrodes have been already checked in 2012, during the KLOE preliminary run. Several measurements and tests demonstrated their effectiveness in thwarting the e-cloud effects [22]. These first studies have all been done by biasing the striplines with a positive voltage in the range 0÷250 V. However simulations indicate that a factor two higher voltage is required to completely neutralize the *e-cloud* density due to a e⁺ current of the order of 1 A. For this reason, during the 2013 shutdown, the electrode power supplies have been replaced with devices providing a maximum negative voltage of 500 V. The change of polarity was intended to limit the current delivered by the power supplies. The new setup has been tested storing a ~ 700 mA current in 90 bunches spaced by 2.7 ns, and measuring the horizontal and vertical tune spread along the batch with the electrodes on and off. Results show a clear reduction of

the tune spread in both planes, but especially in the horizontal one [23]. It's worth mentioning that presently three out of the four electrodes installed in the wiggler magnets have been short-circuited since they were not working properly. Moreover a random vertical oscillation of the e+ beam orbit, affecting the collider fine tuning and data delivery, has been correlated with the electrodes operation. Orbit perturbations with amplitude in the range ±0.5 mm have been already observed before the 2013 shutdown, albeit with lower occurrence, and have been ascribed to the electrodes for two experimental reasons. First, oscillation phase can be decomposed in terms of the phases characterizing the orbit variations measured switching on the electrodes one by one. Second, the effect has been cured, after achieving a reasonable dynamic vacuum level, by tuning the electrode working voltage in order to limit the current delivered by the power supply. However, the mechanism causing this effect has not yet been completely understood.

Another positive result in mitigating the detrimental effects induced by the e-cloud has been obtained lengthening the bunch by reducing the voltage of the RF cavity of the e$^+$ ring. Fig. 8 presents the behavior of the pressure rise with the stored current, measured by two vacuum gauges installed on different arcs, as a function of the RF cavity voltage.
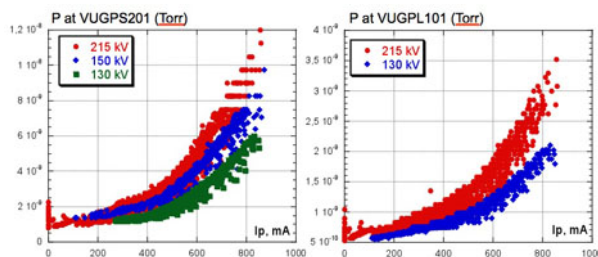
Figure 8: Pressure rise versus stored e$^+$ current in two different arcs of the e$^+$ ring as a function of the RF cavity voltage.

The e$^-$ beam exhibits a microwave instability threshold (TMCI), appearing above a current of the order of ~10 mA per bunch, resulting in a widening of the transverse beam sizes. Such effect is quite moderate in single beam operation and becomes more harmful in collision due to the beam-beam interaction. The instability might be limited by implementing an optics providing a higher value of the momentum compaction a_c.

In general beam dynamics also profited from upgrading collimators and replacing the bellows installed in the IR close to the low-β section. In fact some of them were seriously damaged and were causing random discharges.

2.1.5 *Crab-Waist* Collisions

A detailed comparison of the beam parameters corresponding to the record luminosities achieved in some topical stages of the DAΦNE activity is presented in Table 1.

Maximum instantaneous luminosity is now a ~33% higher with respect to the past KLOE run, regardless it has been obtained by colliding beams having lower currents and lower number of bunches. This improvement is consistent with the maximum daily integrated luminosity, which is now ~28% higher with respect to 2005.

Despite these positive results, instantaneous luminosity is still a factor 2 lower than the peak value measured during the Crab-Waist test run. Anyhow daily integrated luminosity differs, in defect, from the best attained in 2009 by a ~20% only.

Table 1: Beam currents and number of bunches used for collisions: during the test run of the new Crab-Waist collision scheme, while giving data to a detector without solenoidal field, during the KLOE run in 2005 and in the present configuration which integrates the Crab-Waist collision scheme with the KLOE-2 detector having high perturbing solenoidal field.

Parameter	Crab-Waist test run (2009)	KLOE run (2005)	KLOE-2 Crab-Waist (2015)
L_{peak} [cm^{-2}s^{-1}]	$4.53 \cdot 10^{32}$	$1.5 \cdot 10^{32}$	$2.0 \cdot 10^{32}$
I^- [A]	1.52	1.4	1.03
I^+ [A]	1.0	1.2	1.03
N_b	105	111	103
$L_{\int day}$ [pb^{-1}]	15	9.8	12.5

Several solid arguments, based on experimental and theoretical considerations, indicate that the higher instantaneous luminosity measured with the KLOE-2 detector is due to the beneficial effects introduced by the *Crab-Waist* collision scheme.

A comprehensive numerical study has been performed in order to investigate the effectiveness of the crab waist collision scheme in presence of the strong solenoidal fields introduced by the KLOE-2 detector [17]. Beam-beam simulations have been carried out taking into account the real DAΦNE nonlinear lattice including the detector solenoidal fields, IR quadrupole rotations, compensating anti-solenoids etc. The numerical results clearly show that, in DAΦNE, the detector solenoid does not determine any relevant reduction in terms of crab waist collision scheme effectiveness.

Indeed, *CW*-Sextupoles have been used since the beginning of the collider commissioning with KLOE-2, then their strength has been gradually increased along with the nonlinear beam dynamics optimization.

Experimental test [13], done switching off the *CW*-Sextupoles, lead to achieve a luminosity slightly in excess of 10^{32} cm^{-2}s^{-1}, and outlined harmful effects such as: beam lifetime reduction while injecting the opposite beam, transverse beam blow-up at high current and unprecedented background level, both in coasting and injection regime. All these phenomena are perfectly consistent with the lack of a compensation mechanism for the synchro-betatron resonances affecting collisions in large Piwinsky angle regime.

The beneficial effect of the *CW*-Sextupoles can be clearly seen by looking at the luminosity, lifetime and the detector background by varying the *CW*-Sextupoles strength see Fig. 9.
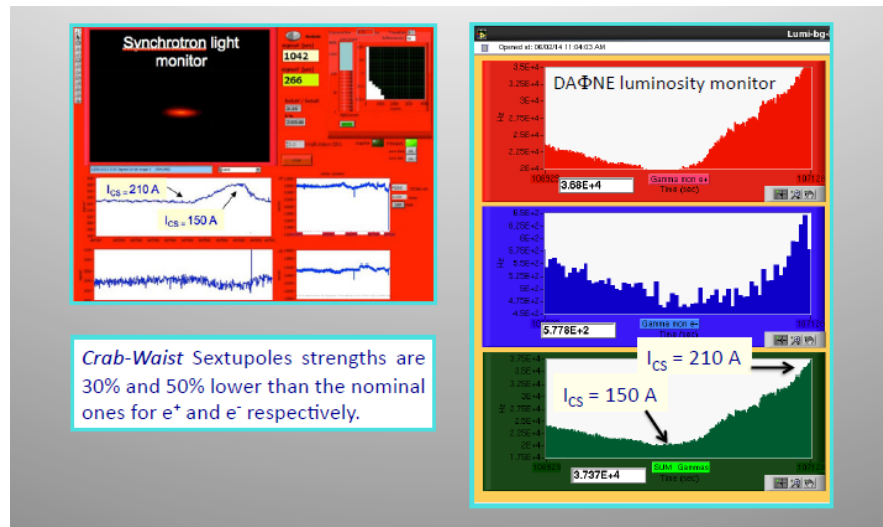
Figure 9: Decreasing the *CW*-Sextupoles strengths the vertical beam sizes, as measured at the synchrotron light monitor, increase (left panel); at the same time the luminosity grows, as reported by the DAΦNE fast luminosity monitor (right panel upper and central frame) and by the KLOE detector luminosity monitor (right panel lower frame).

However the full potential of the crab waist collision scheme has not yet been exploited due to several limiting factors already discussed in the previous paragraphs.

In fact future programs foresee to improve DAΦNE performances by:

- improving *CW*-Sextupoles alignment on the beam orbit and optimizing their strengths
- refining transverse betatron coupling correction
- pushing the microwave instability threshold toward higher single bunch current value by means of new optics configuration having higher α_c and higher chromaticity
- vacuum conditioning and beam scrubbing to diminish the e-cloud impact on e$^+$ beam dynamics
- further feedback noise reduction
- tuning the interplay between RF 0-mode feedback and longitudinal feedback.

2.1.6 DAΦNE Data Delivering

On mid November 2014 a plan has been agreed with the KLOE-2 collaboration team in order to start a preliminary data-taking campaign. The most relevant point of the plan stated the collider had to deliver 1 fb^{-1} in 8 months long continuous operations.
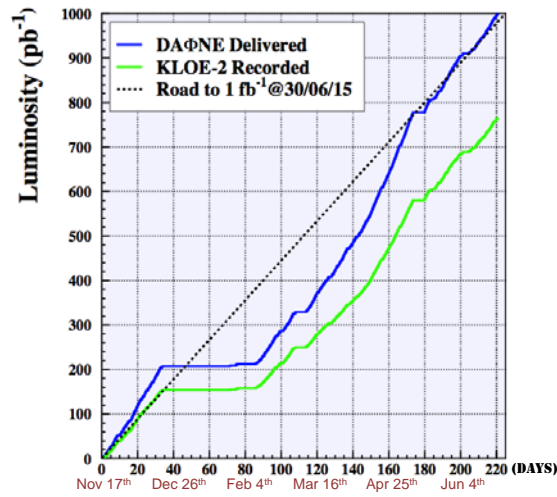
Figure 10: Delivered (blue line) and acquired (green line) luminosity presented together with the scheduled plan (black dotted line).

Data taking results are summarized in Fig. 10. In the first month of operations the integrated luminosity growth rate was well above the predefined guideline. After that, the 23 days long stop, scheduled for winter holiday prolonged to mid-February due to delays in completing some activities, and to several faults occurring in sequence and having different relevance. Main faults involved the cooling system of the KLOE magnet power supply and the klystron of the RF plant serving the electron ring. Although the first problem required long time, a lot of measurements and chemical wash of the circuit to be fixed, it did not pose any concern on the collider program feasibility. The latter, on the contrary, was quite threatening, since it required the installation and testing of the klystron previously mended in house and stored in the DAΦNE hall. The whole operation, including: faulty klystron removal, spare device installation and conditioning, took about 10 days. Whereupon a stable electron beam with a current $I^- \sim 1.6$ A has been stored and used for collisions. Tests performed on the broken klystron pointed out a leakage in the insulation vacuum, very much similar to the one already repaired, which was fixed as well.

In the following three months DAΦNE had long, stable operations, in which achieved its best performances in terms of instantaneous and integrated luminosity.

Collider optimization, progressive vacuum melioration, luminosity fine tuning, higher number of colliding bunches and improved control over e-cloud induced effects led instantaneous luminosity to reach the value of 1.88×10^{32} cm^{-2} s^{-1} by mid-March 2015. Thence, after adopting a new more suitable working point in the electron ring, according theoretical simulation, a reproducible peak luminosity of the order of 2.0×10^{32} cm^{-2} s^{-1} has been achieved by the end of April.

Stability of the collider setup is confirmed by record results concerning long term integrated luminosity. In fact, 71 bp^{-1}, see Fig. 11, have been delivered in a week of operation.

Delivered (week)	Acquired on disk (week)	
71 pb⁻¹	53 pb⁻¹	
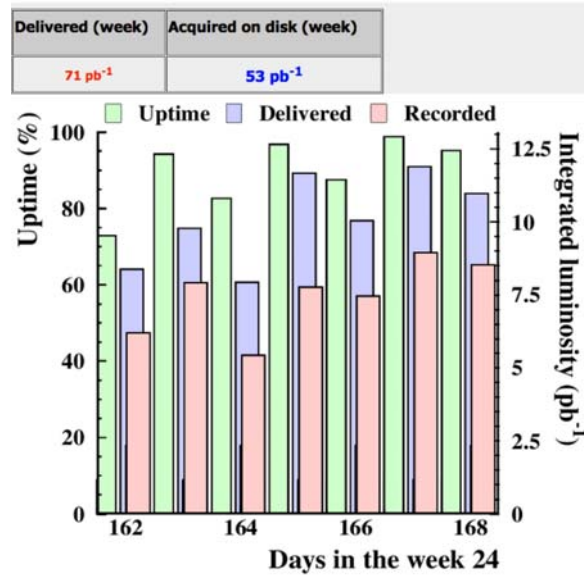
Figure 11: Best weekly delivered (violet bin) and integrated (red bin) luminosity, presented together with the machine uptime (green bin) defined as the percent fraction of the day the collider has been delivering luminosity, suitable for acquisition, in excess of ~ 0.1 10^{32} cm⁻² s⁻¹.

This promising result when accounted together with the 251 pb⁻¹ delivered in 30 consecutive days, see Fig. 12, clearly indicates that the KLOE-2 run, aimed at collecting about 5 fb⁻¹ total integrated luminosity, is feasible and can be completed in a time lapse of the order of 2-3 years.
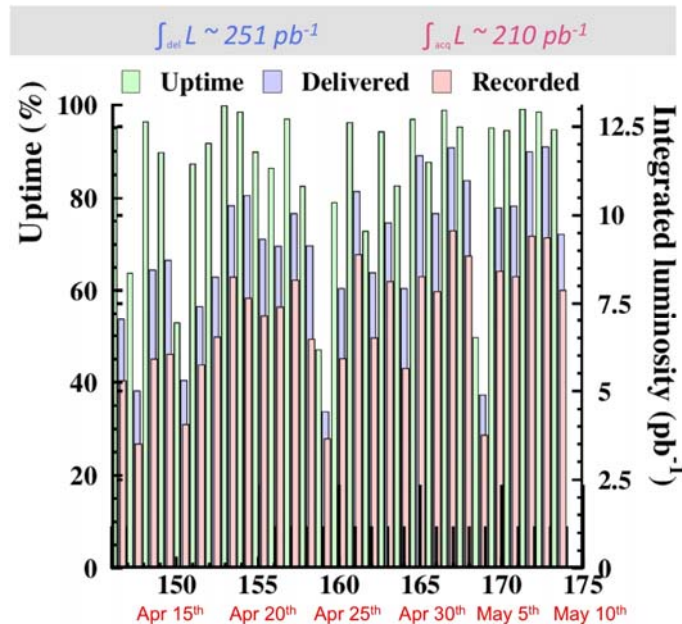
Figure 12: Best monthly delivered (violet bin) and integrated (red bin) luminosity, presented together with the machine uptime (green bin).

Furthermore long term integrated luminosity can still be improved, even without changing currents and number of colliding bunches, as suggested by the best hourly

integrated luminosity measured averaging over two hours, which is $L_{\int 1hour} \sim 0.54$ pb^{-1}, see Fig. 13, regardless some minor faults occurring during the run and some inefficiency in the injection process.
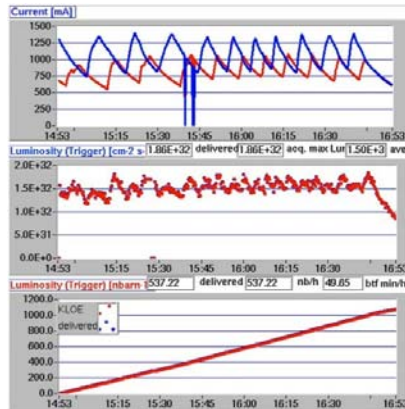
Figure 13: Best hourly integrated luminosity.

Collider uptime, presented in Fig. 11 and Fig. 12, is defined as the percent fraction of the day in which the collider has been delivering luminosity, suitable for acquisition, in excess of $\sim 0.1 \times 10^{32}$ cm^{-2} s^{-1}. A quite strict definition indeed. Nevertheless average uptime, in the interval presented, is always well above 80%, a value representing the upper limit usually achieved in particle accelerators like DAΦNE.

Another issue of primary importance, second only to the integrated luminosity rate, is the background hitting the experimental apparatus. Background produced by the beams colliding at DAΦNE is essentially due to the Touschek effect. It has a very high impact on all subsystems involved in the data acquisition: DAQ boards, KLOE-2 networks, data buffering, mid-term (disk) and long-term (tape) support consumption. Although the present background rate is compatible with an efficient detector data taking, it is about a factor two higher with respect to the old KLOE run (2005). Special concern was given by the component due to the e- beam, which has been considerably reduced varying optics in the e$^-$ ring.

In the last two months integrated luminosity growth rate slowed a little bit down due to periodic maintenance, safety checks and the exceptionally high atmospheric temperatures forcing several subsystems to work in critical condition.

In summary, 1.0 fb^{-1} has been delivered to the experiment in approximately 200 days of activity according the scheduled plan. Moreover integrated luminosity delivering rate, background level and collider uptime are compatible with an efficient data taking of the KLOE-2 detector.

2.1.7 Conclusion

The DAΦNE collider has recently achieved very positive results: instantaneous luminosity and integrated luminosity rate are now the highest ever measured in operations with an experimental apparatus including high field detector solenoid, confirming the *Crab-Waist* collision scheme effectiveness in achieving high luminosity even in presence of a large detector.

Machine uptime profited from the several consolidation activities implemented, and presently can assure a long term data taking to the detector.

Beside the present promising results, several limiting factors have been outlined and understood, and still many parameters can be ameliorated to improve the collider performances.

The KLOE-2 collaboration has started its data acquisition campaign, and the collider has already delivered 1fb^{-1} according the scheduled plan.

2.1.8 References

1. G. Vignola et al., "Status Report on DAΦNE", Frascati Phys. Ser. 4:19-30, 1996; C. Milardi et al., "Status of DAΦNE", Frascati Phys. Ser. 16:75-84, 1999.
2. C. Milardi et al., "DAΦNE Operation with the FINUDA Experiment", EPAC04, pp. 233-235, arXiV:physics/0408073.
3. A. Gallo et al., "DAΦNE Status Report", EPAC06, Conf.Proc. C060626 (2006) 604-606.
4. P. Raimondi et al., "Beam-Beam Issues For Colliding Schemes with Large Piwinski Angle and Crabbed Waist", arXiV:physics/0702033.
5. C. Milardi et al., "Present Status of the DAΦNE Upgrade and Perspectives", Int.J.Mod.Phys.A24:360-368, 2009.
6. M. Zobov et al., "Test of Crab-Waist Collisions at DAΦNE Phi Factory", Phys. Rev. Lett. 104, 174801 (2010).
7. C. Milardi et al, "DAΦNE Developments for the KLOE-2 Experimental Run", IPAC10, p. 1527, Conf.Proc. C100523 (2010) TUPEB006.
8. C. Milardi *et al*., "High Luminosity Interaction Region Design for Collisions Inside High Field Detector Solenoid", 2012 *JINST* 7 T03002.
9. C. Milardi et al, "DAΦNE Tune-Up for the KLOE-2 Experiment", IPAC11, Conf.Proc. C110904 (2011) 3688-3690.
10. KLOE-2 Collab., LNF - 10/14(P) April 13, 2010.
11. C. Milardi et al, "DAΦNE General Consolidation and Upgrade", IPAC14, p. 3760, IPAC-2014-THPRI002.
12. S. Bettoni et al., "Multipoles Minimization in the DAΦNE Wigglers", IPAC10, Conf.Proc. C100523 (2010) THPE065.
13. C. Milardi et al, "DAΦNE Operation with the Upgraded KLOE-2 Detector, IPAC14, p. 1883, IPAC-2014-WEOCA03.
14. D. Shatilov, "Beam-Beam Simulations at Large Amplitudes and Lifetime Determination", Particle Accelerators 52:65-93, (1996).
15. D. Shatilov et al., "Application of Frequency Map Analysis to Beam-Beam Effects Study in Crab Waist Collision Scheme", Phys. Rev. ST Accel. Beams 14, 014001 (2011).
16. **http://cern.ch/madx**
17. M. Zobov et al., "Simulation of Crab Waist Collisions In DAΦNE with KLOE-2 Interaction Region", IPAC15, p. 229, arXiv:1506.07559.
18. A. De Santis, https://agenda.infn.it/conferenceDisplay.py?confId=9613.
19. A. Drago et al., "Recent Observation on a Horizontal Instability in the DAΦNE positron ring", PAC05, p. 1841, SLAC-PUB-11654.
20. A. Drago et al., "DAΦNE Bunch by Bunch Feedback Upgrade as SuperB Design Test", IPAC11, Conf.Proc. C110904 (2011) 490-492.
21. D. Alesini et al., "DAΦNE Operation with Electron-Cloud-Clearing Electrodes", Phys. Rev. Lett. 110, 124801 (2013).
22. D. Alesini et al., "Design and Test of the Clearing Electrodes for e-Cloud Mitigation in the e+ DAΦNE Ring", IPAC10, p. 1515, Conf.Proc. C100523 (2010) TUPEB002.
23. A. Drago, http://indico.cern.ch/event/306551/.

2.2 SuperKEKB Project at KEK

Yoshihiro Funakoshi

KEK, 1-1 Oho, Tsukuba, Ibaraki 305-0801, Japan

Mail to: yoshihiro.funakoshi@kek.jp

2.2.1 Concepts of SuperKEKB

2.2.1.1 *Physics Motivations*

The most important outcome of the physics experiment at KEKB/Belle was the detection of CP violation in B mesons predicted on the basis of the Kobayashi–Maskawa theory [1]. Prof. M. Kobayashi and Prof. T. Maskawa were awarded the 2008 Nobel Prize in Physics for this theory. The Belle experiment, carried out using KEKB, contributed greatly to confirmation of the theory. The physics goals of SuperKEKB/Belle-II, as a next generation flavour factory, are to search for phenomena of the new physics (NP), which cannot be explained by the standard model (SM) of the elementary particle physics, in the flavour sector at the precision frontier, and to further reveal the nature of QCD in describing matter [2]. The target integrated luminosity is set at 50 ab^{-1} considering machine feasibility. The design peak luminosity is 8×10^{35} cm^{-2} s^{-1} [2]. The integrated luminosity of 50 ab^{-1} will be accumulated in about 10 years.

2.2.1.2 *Some History*

The study of SuperKEKB started in 2001 when the KEKB commissioning was in an early stage. The initial design of SuperKEKB was based on so-called "high-current option" where the design beam currents were 9.4 and 4.1A for positron and electron beams, respectively [3]. In this option, very high beam-beam parameters of 0.3 or 0.5 were assumed with the crab crossing based on beam-beam simulations. As for the vertical beta function at IP was designed as about 3mm. The design peak luminosity was 5×10^{35} cm^{-2} s^{-1}. This option of design was finally given up for several reasons. The first, it turned out that the design bunch length of 3 mm cannot be achieved for the positron beam due to the CSR impedance and the vertical beta function of HER (electron) at IP cannot be squeezed to 3mm due to the hourglass effect. The second, the beam-beam parameters at KEKB with the crab cavities did not reach 0.15 which is the value predicted by the beam-beam simulation. The third, the horizontal emittance becomes very large due to the dynamic beta effect in this option where the horizontal tune is very close to the half-integer and as a result the horizontal beam size at the IR quardupole magnets become also very large and so the SR power from those magnets becomes huge. Due to those difficulties, we decided to change the design scheme from the "high-current option" to the scheme proposed for SuperB in Italy with the crab-waist scheme [4]. In case of SuperKEKB, the crab-waist scheme is not assumed in the design. We call this scheme "nano-beam scheme", since the vertical beam sizes at IP are near the order of nano meter. The KEKB operation was terminated on June 30th 2010. Just after this, the construction works toward SuperKEKB started. The upgrade works for the initial operation for SuperKEKB are approaching completion and the beam commissioning is supposed to start in Feb. 2016.

2.2.1.3 *Ideas of SuperKEKB and Choice of Machine Parameters [2]*

Some basic machine parameters are shown in Table 1 in comparison with those achieved at KEKB. LER and HER in the table stand for Low Energy Ring (positron) and HER Energy Ring (electron), respectively. To realize the "nano-beam scheme", we need a relatively large crossing angle and the small horizontal beam size at IP. For the small horizontal beam size at IP, the horizontal emittance and the horizontal beta function are chosen as small as possible. With those parameters, the length of the overlap region of the two beams at IP is as small as ~0.3mm. That value is compared with the value at KEK, ~6mm, which is basically determined by the bunch length. With this condition, it becomes possible that the vertical beta function at IP can be squeezed down to ~0.3mm. With this small β_y^*, the luminosity can be increased by factor 20. For further luminosity increase, the beam currents are increase by about a factor 2. Since almost same vertical beam-beam parameters are assumed, the luminosity of SuperKEKB is a factor 40 higher than that of KEKB.

Table 1: Basic machine parameter of SuperKEKB in comparison with those achieved at KEKB.

Parameter	Unit	SuperKEKB (LER/HER)	KEKB (LER/HER)
Beam energy E_b	GeV	4/7.007	3.5/8
Full crossing angle 2ϕ	mrad	83	22
Horizontal emittance ε_x	nm	3.2/4.6	18/24
Emittance Ratio ($\varepsilon_y/\varepsilon_x$)	%	0.27/0.25	0.88/0.66
Horizontal beta function at IP β_y^*	mm	32/25	1200/1200
Overlap length of two beams at IP	mm	~0.3mm	~6mm
Vertical beta function at IP β_y^*	mm	0.27/0.30	5/9/5.9
Beam current I_{beam}	A	3.6/2.6	1.64/1.19
Vertical beam-beam parameter ξ_y		0.088/0.081	0.129/0.090
Luminosity L	cm^{-2}s^{-1}	8×10^{35}	2.1×10^{34}

2.2.2 Brief Summary of Hardware Upgrade [2]

2.2.2.1 *RF System*

The main purpose of the RF upgrade is to support as twice as high beam currents compared with KEKB. At KEKB, normal conducting damped cavities named "ARES" were used in both rings. In HER, we also used single cell superconducting cavities (SCC). At SuperKEKB, we will keep this basic scheme. An idea for increasing beam currents is to add klystrons for cavities. At KEKB, two ARES cavities were fed by one klystron. At SuperKEKB, each ARES cavity is fed by one klystron. In LER, the number of klystrons will be increased from 10 to 18. In HER, the number of klystrons for ARES will be increased from 7 to 8. In addition, two klystrons for the crab cavities will feed two new SCCs. As for the HOM power, each cavity for SuperKEKB will have to handle about 3 times higher HOM power than that of KEKB. No modification for the ARES cavity will be needed, since it has much potential for HOM power handling. On the other hand, we need some modifications for SCCs. To reduce HOM power, a taper

chamber attached to a SCC and a gate valve will be replaced with those with larger bores. An additional damper made of SiC is also implemented between the SC cavities. As for the coupled bunch instability originated from the cavities, we will install a bunch-by-bunch feedback system in the longitudinal direction in LER, which was not needed at KEKB, to suppress the instability due to the HOM modes of the ARES cavities. To mitigate the effect of the bunch gap transient, the length of the abort gap is reduced from 5% (KEKB) to 2% of the ring. The analog low level RF system used at KEKB is replaced with a digital system. With the new system, better phase stability and more flexibility are expected.

2.2.2.2 *Magnet System*

The basic design concept for SuperKEKB is to use the KEKB tunnel and to reuse the components of KEKB as much as possible. In the LER arcs, the main dipole magnets of 0.89m are replaced with longer ones (4.0m) to lower the emittance with keeping other main magnets. We will preserve the KEKB arc cells in HER, since the length of the main dipole magnets is long enough and there is no room to lengthen them. In addition, the wiggler layout of LER is changed so that the peak value of the dispersion is reduced from ~10mm to ~5mm for lower emittance. As for HER, the wiggler magnets are newly installed for reducing the emittance. The KEKB/SuperKEKB arc cells are called "2.5π cells" which was invented at KEK. A remarkable feature of this lattice is that the emittance and the momentum compaction factor can be changed in a wide range by changing the strength of cell quadrupoles. At SuperKEKB, this tunability is used for minimizing the emittance. In the IR section, the lattice and all magnets are newly designed and replaced.

2.2.2.3 *Vacuum System*

Almost all beam pipes of LER are replaced with new ones with antechambers. The main purposes of the antechambers are to reduce the effects of the electron clouds and to give higher strength against intense SR. Other components of bellows chambers, gate valves, collimators, beam stoppers and so on are redesigned to fit the beam pipes and to give higher strength against a higher beam power. On the other hand, most of KEKB beam pipes of HER except for the IR section will be reused, since the beam energy of HER is lowered from 8GeV to 7GeV and the strength of SR is lowered in spite of a higher beam current. In LER, further countermeasures against the electron cloud effects will be applied such as solenoid magnets like for KEKB, TiN coating for suppressing the secondary electron emission, clearing electrodes in the wiggler magnet sections and grooved surface in bending magnet sections. Simulations show that the effects of the electron clouds will be completely suppressed by those countermeasures.

2.2.2.4 *IR*

With the larger crossing angle (83 mrad) than KEKB, the final focus quardupole magnets can be independent for the two rings. In case of KEKB, those were common to the two beams. This enables us to shorten L*. L* for LER and HER at SuperKEKB are 0.73m and 1.2m on both sides, respectively, whereas those of KEKB were 1.4m (left side) and 1.7m (right side). Also, this makes handling the intense SR from the quadruples easier. Success of SuperKEKB largely depends on how low values of IP beta-functions will be achieved with enough dynamic aperture. The IR superconducting

magnets consist of final doublet quadrupoles (QC1s and QC2s), correction winding coils attached on them, compensation solenoid coils, additional sextupole correction coils and compensation coils (sextupole, octupole, decapole and dodecapole) attached on QC1Es (QC1s for electrons) which compensate leakage fields from the QC1Ps (QC1s for positrons). The correction coils are dipoles, skew-dipoles, skew-quadrupole, sextupoles, skew-sextupoles and octupoles. Error fields originated from fabrication errors of the magnets are corrected by the coils. In addition, the octupole coils are used to enlarge a transverse dynamic aperture against effects of the fringe fields of the QC1s and the kinematic term of the IP drift space.

Figure 1 shows the IR optics of LER on the left side of IP. In both vertical and horizontal directions, the local chromaticity correction scheme is adopted. Skew quadruples (QKs) are needed to correct the x-y coupling originated from the detector solenoid.

Figure 1: IR optics of LER (left side of IP).

2.2.2.5   *Injector and Damping Ring*

At SuperKEKB, requirements to the injector are much severer than at KEKB. Since he beam lifetime is much shorter and the ring aperture is much narrower, the bunch intensity should be much higher and the beam emittance be much lower. To meet these requirements, we have been developing a high intensity and low emittance RF gun for the electrons. For the positrons, we redesigned the positron capture section with a flux-concentrator and newly introduce a damping ring. Its circumference is 136m and the beam energy is 1.1 GeV.

2.2.3   Beam Physics Issues

2.2.3.1   *Dynamic Aperture*

As is shown in Table 1, the most important parameter for the luminosity of SuperKEKB is the IP vertical beta function (β_y^*). Feasibility of the SuperKEKB design luminosity depends on whether thus low β_y^* is achievable or not. To get to the design values of β_y^*, the hardest obstacle is the reduction of dynamic aperture. A small dynamic aperture causes a short Touschek lifetime and/or poor injection efficiency. At SuperKEKB, the dynamic aperture is mainly restricted by the nonlinear terms from the drift space near IP, so called kinematic terms, and the Maxwellian fringe fields of QC1s magnets. By optimizing IR optics including the local chromaticity corrections, octupole correctors in IR, sextuple magnets in IR and in the arcs and skew-sextupole magnets in the rings, we get the Touschek beam lifetime of ~ 600 s for both rings without machine errors nor the beam-beam interaction. Even with the machine errors, the injector seems to possibly compensate the particle losses with the design luminosity. Table 2 shows a summary of the beam lifetime and the loss rate of particles in comparison with the KEKB case.

Table 2: Summary of beam lifetime and loss rate.

	KEKB (Design)		KEKB (Operation)		SuperKEKB (Design)	
	LER	HER	LER	HER	LER	HER
Radiative Bhabha	21.3h	9.0h	6.6h	4.5h	28min.	20min.
Beam-gas	45h [a]	45h [a]			24.5min. [b]	46min. [b]
Touschek	10h	-			10min.	10min.
Total	5.9h	7.4h	~133min.	~200min.	6min.	6min.
Beam current	2.6A	1.1A	1.6A	1.1A	3.6A	2.6A
Loss rate	0.12mA/s	0.04mA/s	0.23mA/s	0.11mA/s	10mA/s	7.2mA/s

a) Bremsstrahlung, b) Coulomb scattering

2.2.3.2   *Beam-beam Related Issues*

It turned out that the dynamic aperture is seriously reduced with the beam-beam interaction at SuperKEKB as is discussed in other articles in this Newsletter [5][6]. A particle with some large horizontal amplitude collides with the other beam at a longitudinally shifted position where the vertical beta function is some large. This process induces the vertical oscillation and the dynamic aperture is reduced as a result. These phenomena might be avoided, if the crab-waist scheme works. However, it seems that the crab-waist scheme itself reduces the dynamic aperture seriously and does not work at SuperKEKB as is discussed in Ref [5]. This is an unsolved issue at SuperKEKB.

Another issue is related to the achievable luminosity. The design luminosity of SuperKEKB was determined by a beam-beam simulation [7]. Afterward, we found that the luminosity is degraded by combined effects of the beam-beam interaction and a lattice nonlinearity and the space charge effect as is discussed in Ref [6]. This is also an unsolved problem so far and we will need further mitigations and/or compensations.

2.2.3.3 *Low Emittance Tuning*

The design vertical emittance of SuperKEKB shown in Table 1 is very small compared to those of existing colliders. The low vertical emittances have been achieved in SR machines. However, low emittance tuning in colliders is much more difficult, since there exists IR including the detector solenoid and the beam-beam interaction. An important point of the low emittance tuning is how to correct machine errors. Extensive simulations have been done assuming machine errors. Table 3 shows a list of machine errors used in the simulations. The machine errors were created randomly with Gaussian distributions. The method of the machine error corrections was the same as that used at KEKB. We corrected closed orbits, an x-y coupling, a beta-beat, and dispersions. The x-y coupling, the beta-beat and the dispersions were corrected iteratively. This method corrects each observable iteratively rather than correcting all observables simultaneously with a big matrix. The simulations showed that the design values of the vertical emittance would be attainable with the correction method.

Table 3: Machine errors assumed at SuperKEKB.

Components	Offset $\sigma_x = \sigma_y$ (µm)	Rotation σ_ϕ (µrad)	*Strength* $\Delta K/K$
Normal Quadrupoles	100	100	2.5×10^{-4}
Sextupoles	100	100	22
Bending magnets	0	100	0
IR quadrupoles (QC1s, QC2s)	0	0	0
BPM	0	10×10^3	2µm (resolution)

2.2.3.4 *IP Orbit Control [8]*

In order to maintain an optimum beam collision condition in a double ring collider such as KEKB or SuperKEKB, it is essential to have an orbit feedback system at the IP. At KEKB, we used the beam-beam deflection to detect the orbit offset at the IP both in horizontal and vertical directions [9]. At SuperKEKB, we will adopt nano-beam scheme. In this scheme, the horizontal beam-beam parameter is very small and we cannot rely on the beam-beam deflection method for the orbit feedback at IP in the horizontal direction. Instead, we will adopt the dithering system for the horizontal orbit feedback used at PEP-II [10]. In the vertical direction, we will use the beam-beam deflection like at KEKB. However, the orbit control is much more difficult than at KEKB. Since the vertical emittance is much lower and the vertical beta functions at QC1s are much larger than KEKB, small vibrations of QC1s affect the beam collision. To cope with this problem, we have developed a fast orbit feedback system which gives the rejection gain of ~ -17dB at 25Hz. In addition, coherency of mechanical vibrations of QC1s for the electron and positron on the same side of the IP, which are located in the same cryostat, is very important. If those magnets vibrate coherently, the orbits of the two beams change in the almost same way at the IP and the beam collision is kept. We fully rely on this coherency.

2.2.3.5   *Detector Beam Background*

At SuperKEKB with a factor of 40 larger luminosity, detector beam background will also increase drastically. The important processes for the background are the Touschek scattering, the beam-gas scattering, the radiate Bhabha process, the 2-photon process and the synchrotron radiation. Extensive simulations done using SAD and GEANT4 shows that an impact of the background on detector performance (occupancy, tracking/PID performance etc.) is tolerable with the design luminosity, if we set collimators properly and install the radiation shields on the QCS magnets. Assuming 10 years operation at the design luminosity, most of the detector components are safe for radiation damage except for TOP PMT (Photo-Multiplier Tube) photocathode lifetime, which needs a factor of 2 reduction further. Here, TOP stands for "Time Of Propagation" counter located in a barrel part of Belle-II and used for the particle identification.

2.2.4   Commissioning Schedule

The beam commissioning of SuperKEKB will be done in three steps. In the first step (Phase 1), the beam operation will be done without a physics detector (Belle-II) and the IR superconducting magnets. No beam collision is done in this phase. The main tasks in this phase are a basic machine commissioning and the vacuum scrubbing. In addition, some other machine studies such as the low emittance tuning, a study on the detector beam background with a dedicated detector for this purpose and a study on beam instabilities. The Phase 1 commissioning will start in Feb. 2016 in the present plan. A period of the Phase 1 operation is about 5 months.

In the second step (Phase 2), the Belle-II detector and the IR superconducting magnets are installed. However, the vertex detectors will not be installed in this phase. A full machine commissioning will start in this phase. The target peak luminosity is 1×10^{34} cm^{-2} s^{-1}, which is the design luminosity of KEKB. The missions of the commissioning in this phase are to establish a condition where Belle-II can take data stably and to understand the detector beam background before installation of the vertex detectors. In addition, some physics experiment will also be done in this phase. In the present plan, the Phase 2 operation will start in June 2017 and continue for about 5 months expect for the summer shutdown. The commissioning of the damping ring will be done between Phase 1 and Phase 2 periods.

The Phase 3 operation will start in autumn in 2018 in the present plan and continue for many years. The target peak luminosity is 8×10^{35} cm^{-2} s^{-1} and we aim to accumulate 50 ab^{-1} by around 2022.

2.2.5   References

1. T. Abe et al., "Achievements of KEKB", Prog. Theor. Exp. Phys. 2013, 03A001.
2. T. Abe et al., Technical Design Report of SuperKEKB, in preparation and to be published as a KEK report. An preliminary version is seen in "https://kds.kek.jp/indico/event/15914/" .
3. Y. Funakoshi, "SuperKEKB Project", "Acclerator" Vol.6, No.1 (2009). in Japanese.
4. P. Raimondi, "Status on SuperB effort", 2nd LNF Workshop on SuperB, 16-18 Mar. 2006, LNF, Frascati, Italy.
5. A. Morita, "Crab waist scheme for SuperKEKB", in this Newsletter.
6. D. Zhou, H. Koiso, A. Morita, K. Ohmi, K. Oide, H. Sugimoto and Y. Zhang, "Beam

Dynamics Issues in the SuperKEKB", in this Newsletter.
7. K. Ohmi, private communications.
8. Y. Funakoshi, H. Fukuma, T. Kawamoto, M. Masuzawa, T. Oki, S. Uehara, H. Yamaoka, P. Bambade, D. E. Khechen, D. Jehanno, V. Kubytskyi, C. Rimbault,, S. D. Anderson, S. Gierman, M. Kosovsky, J. Seeman, C. M. Spencer, M. Sullivan, O. Turgut, U. Wienands, "Interaction Point Orbit Feedback System at SuperKEKB", in proceedings of IPAC2015, Richmond, VA, US (2015).
9. Y. Funakoshi, M. Masuzawa, K. Oide, J. Flanagan, M. Tawada, T. Ieiri, M. Tejima, M. Tobiyama, K. Ohmi, and H. Koiso, "Orbit feedback system for maintaining an optimum beam collision", Phys. Rev. ST Accel. Beams 10, 101001 (2007).
10. A. S. Fisher et al., SLAC-PUB-12608, July 2007.

2.3 Crab Waist Scheme for SuperKEKB

Akio Morita
KEK, 1-1 Oho, Tsukuba, Ibaraki 305-0801 Japan
Mail to: akio.morita@kek.jp

2.3.1 Introduction

The SuperKEKB [1] is an asymmetric-energy double-ring collider to achieve 40 times higher luminosity than that of the KEKB B-factory [2]. To achieve such high luminosity, the SuperKEKB interaction region (IR) is designed for large Piwinski angle collision scheme so called "nano-beam scheme". For the nano-beam scheme, the beta functions at the interaction point (IP) are designed to 32mm / 0.27mm (horizontal / vertical) for the low energy positron ring (LER) and 25mm / 0.30mm for the high energy electron ring (HER), respectively. In order to realize 1/20 times smaller beta-function at the IP than that achieved by the KEKB B-factory, the SuperKEKB IR is designed to use both super-conducting quadrupole doublets for final focus and horizontal/vertical local chromaticity correctors for compensating large natural chromaticity.

The dynamic aperture is restricted by strong nonlinearity of final focus magnets. On the other hand, Touschek lifetime required to be longer than 600 seconds without machine error in order to store design beam current. The achievement of the design target lifetime of the LER is difficult because of relatively large transverse aperture requirement 30 sigma in typical case. In order to obtain enough transverse aperture for the design target lifetime, both chromaticity corrector sextupoles and octupoles implemented on the final focus system are optimized. As the result of this optimization, the Poincare map of the LER is strongly deformed and the amplitude around QC2* quadrupole (the QF-type quadrupole of the final focus quadrupole doublets) is compressed to clear the horizontal physical aperture bottleneck.

The target lifetime is almost achieved without beam-beam effect shown in Fig.1.
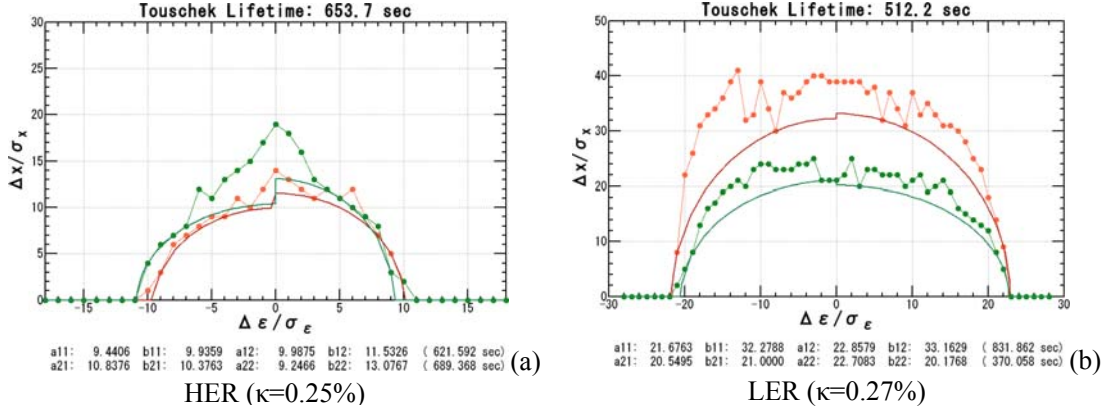
Figure 1: Dynamic aperture and Touschek lifetime of SuperKEKB nominal lattice without beam-beam effect. Horizontal and vertical axes show longitudinal and transverse amplitude of initial particle, respectively. Two lines are correspond with the different initial phases.
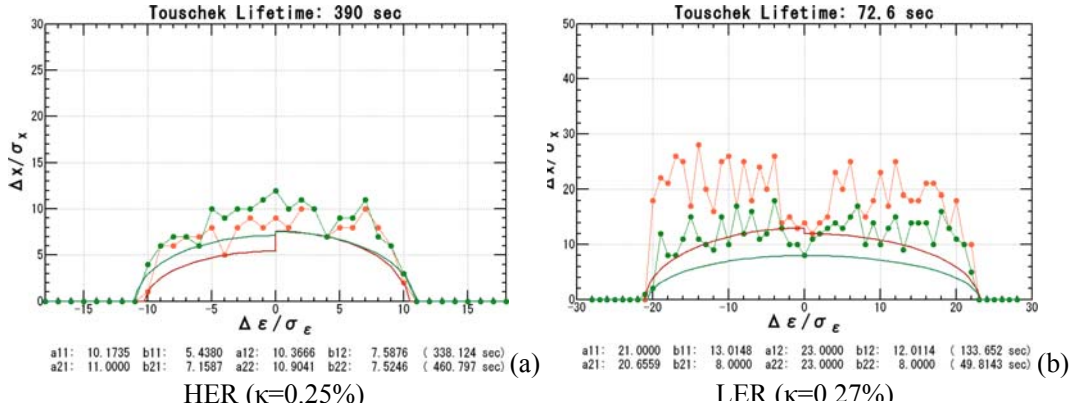
Figure 2: Dynamic aperture and Touschek lifetime of SuperKEKB nominal lattice with beam-beam effect.

On the other hand, the LER lifetime is remarkably degraded by beam-beam effect shown in Fig.2. The HER Touschek lifetime with beam-beam effect is recovered by optimizing chromaticity corrector sextupoles. However, the parameter set for the LER to achieve enough lifetime is not found by the sextupole and octupole parameter survey.

We report a trial result of introducing crab waist scheme [3] into the SuperKEKB lattice in this article.

2.3.2 Improvement of Dynamic Aperture with Beam-beam by Using Crab Waist

The crab waist lattice model is constructed by inserting two thin insertion devices so called crab waist unit. The crab waist unit (CWU) is constructed by a thin sextupole put between two thin linear phase rotators. These linear phase rotators are configured to satisfy following conditions.

- The beta-functions at crab waist sextupole is given as the simulation condition.
- The alpha-functions at crab waist sextupole equal 0.
- The phase advances between the IP and the crab waist sextupole are adjusted

with the proper phase for ideal crab waist.
- The map of CWU converges on the identity map in the limit when K2 of the crab waist sextupole approaches 0.

In the ideal crab waist model, the location of the CWU is configured to sandwich the beam-beam interaction element at the IP between two CWUs. Thus, the ideal crab waist does not change the dynamic aperture without beam-beam effect, because the non-linearity of the crab waist sextupole pair is perfectly canceled by these configuration condition. Figure 3 shows the significant improved dynamic aperture with beam-beam effect by applying the ideal crab waist with LER lattice. The improvement by the ideal crab waist is not perfect, however, it achieves half of design target lifetime that is achieved by optimization by using chromaticity correction sextupoles, octupoles and tune working point.

On the other hand, the dynamic aperture of the realistic crab waist model is shown in Fig.4. In this realistic lattice model, the CWUs are inserted into the feasible location, NIKKO and OHO straight sections, where are separated from TSUKUBA interaction region by arc cells.

| a1: 19.3574 | b1: 26.1399 | a2: 21.0000 | b2: 27.5772 | (554.712 sec) |
| a1: 19.5826 | b1: 13.9197 | a2: 20.0000 | b2: 17.0803 | (196.736 sec) |
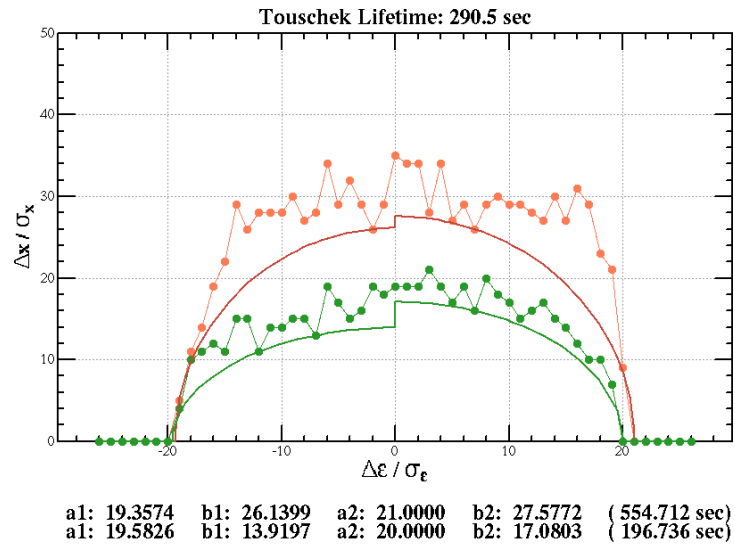
Figure 3: Dynamic aperture and Touschek lifetime of SuperKEKB LER nominal lattice with beam-beam effect and ideal crab waist.
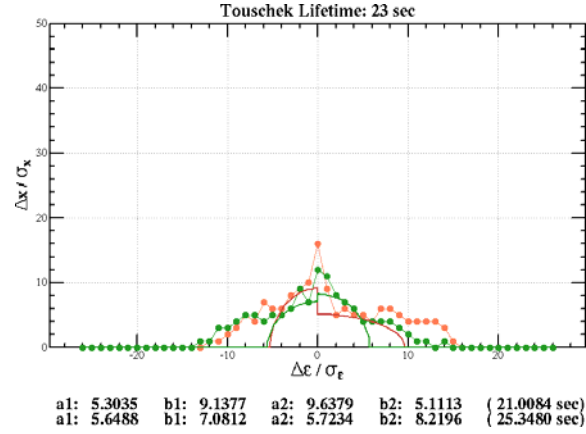
Figure 4: Dynamic aperture and Touschek lifetime of SuperKEKB LER nominal lattice with beam-beam effect and crab waist at feasible location.

In this feasible crab waist configuration, the dynamic aperture is degraded compared with the dynamic aperture without crab waist shown in Fig.2b. Under the weak limit of crab waist sextupole strength, the improvement of the dynamic aperture with beam-beam effect is observed. However, the crab waist sextupole strength dependency of the improved dynamic aperture suggests the upper bound of the aperture improvement by crab waist. In this model, the dynamic aperture without beam-beam effect is limited when K2 parameter of crab waist sextupole exceeds the threshold strength. In the nominal SuperKEKB lattice, this threshold strength of the crab waist sextupole is lower than the theoretical optimum strength and the limited LER dynamic aperture is too narrow to obtain the design target lifetime 600 seconds.

In order to apply crab waist scheme to the SuperKEKB lattice, the dynamic aperture degradation by crab waist have to be resolved.

2.3.3 Nonlinearity Blocking Crab Waist

For investigating the insert location dependency of the CWU, the IR model of the SuperKEKB LER nominal lattice, that contains the solenoid field, the tilted off-axis final focus quadrupole doublets and many higher order multipole fields, is too complex. The simplified lattice for investigation is prepared by removing the non-essential IR multipole fields. Therefore the final focus system of the simplified lattice has only the normal quadrupole doublet fields. Its optics function is re-matched to adjust the Twiss parameters at the IP with the design values.

The following figures show the on-momentum dynamic apertures of the simplified lattice with beam-beam effect and the CWUs. Five different crab waist configuration are listed as follows:

a) The CWUs are inserted into both side of beam-beam interaction element.
b) The CWUs are inserted into the inner boundary of the QD-type final focus quadrupoles QC1*. The crab waist section contains the drift space around the IP.
c) The CWUs are inserted into the inner boundary of the QF-type final focus quadrupoles QC2*. The crab waist section contains the QD-type final focus quadrupoles QC1*.
d) The CWUs are inserted between the QD-type final focus quadrupole QC2* and the suppressor bending magnet for the local chromaticity corrector section. The

crab waist section contains the final focus quadrupole doublets.

e) The CWUs are inserted into the feasible locations NIKKO & OHO straight section.

(a)Ideal location   (b) Inner edge of QC1*   (c)Inner edge of QC2*

(d)Outside of QC1/2*   (e)Feasible location
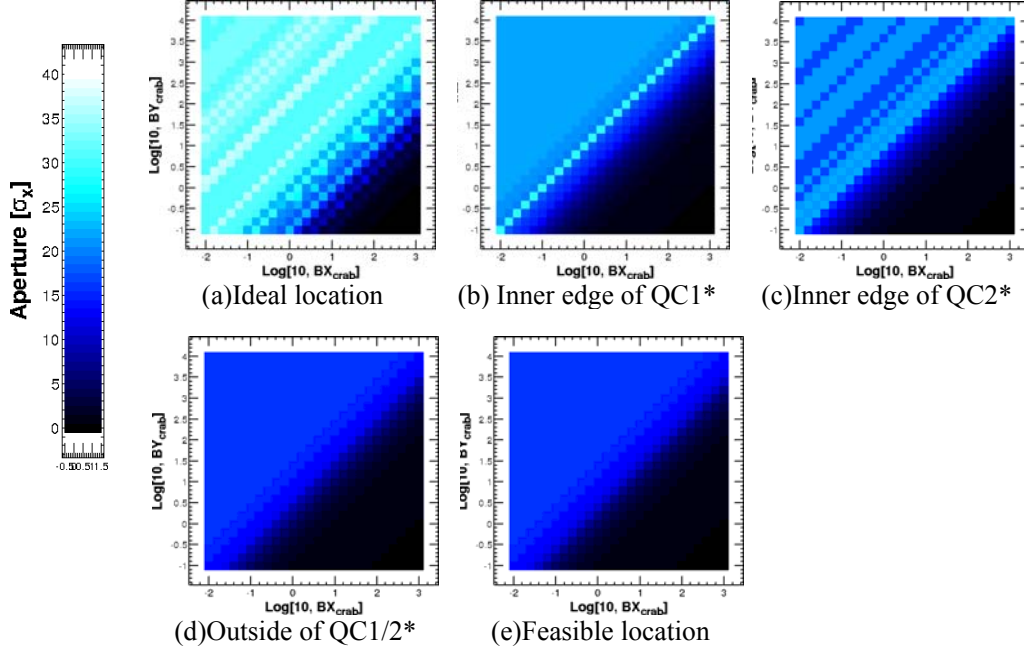
Figure 5: SuperKEK LER on-momentum dynamic aperture with beam-beam effect in different crab waist configurations. Horizontal and vertical axes show horizontal and vertical beta-function at the crab waist sextupole, respectively. The color of the cell shows the on-momentum dynamic aperture.

The on-momentum dynamic aperture of the ideal crab waist shown in Fig.5a decreases when β_y / β_x ratio approaches 0, however, the on-momentum aperture keeps wide enough for the design target lifetime when β_y / β_x ratio is large enough. This behavior and the study results removing the nonlinear term suggest that the $\beta y / \beta_x$ ratio dependency of the on-momentum dynamic aperture is explained by breaking the cancellation between two crab waist sextupoles as the result of the interference between the side effect term of the crab waist sextupole $\Delta P_x = K2(x^2 - y^2)$ and the nonlinear term of beam-beam interaction map.

The on-momentum dynamic aperture of the crab waist containing the drift space around the IP shown in Fig. 5b has the maximum aperture 30 sigma on the line $\beta_y / \beta_x =$ 10. The flat aperture region above β_y / β_x ratio threshold exists, however, its aperture is narrower than that of the ideal case shown in Fig.5a. In this configuration, the on-momentum dynamic aperture required for the design target lifetime could be achieved by adjusting β_y / β_x ratio at the crab waist sextupole.

In the case that the crab waist section contains the inner QD-type quadrupole of the final focus quadrupole doublet shown in Fig. 5c, the maximum aperture is reduced compared with the case shown in Fig. 5b. In this situation, the achievement of the design target lifetime is difficult, because the on-momentum dynamic aperture is narrower than 22 sigma.

From the comparison between two crab waist configurations that contain the final focus quadrupole doublet shown in Fig. 5d and Fig. 5e, the location dependency of the

CWU looks like weak in the case that the CWU is inserted into outside of the final focus quadrupole doublet.

From the comparison of the simplified crab waist lattice models, the major Touschek lifetime blocker for SuperKEKB LER lattice seems the nonlinearity of the final focus quadrupoles.

2.3.4 Summary

In the SuperKEKB lattice with the crab waist, the nonlinearity of the final focus quadrupole, which would be nonlinear Maxwellian fringe, limits the transverse aperture by breaking the sextupole nonlinearity cancellation between two crab waist sextupoles in large amplitude region. Therefore, either lattice redesigning or new nonlinearity compensation scheme for the final focus system is required in order to apply the crab waist scheme to the nominal SuperKEKB lattice.

2.3.5 References

1. Y. Ohnishi, "Accelerator design at SuperKEKB", Prog. Theor. Exp. Phys. (2013) 03A011, 10.1093/ptep/pts083, March 2013.
2. T. Abe, "Achievements of KEKB", Prog. Theor. Exp. Phys. (2013): 03A001, 10.1093/ptep/pts102, March 2013.
3. P. Raimondi, "Beam-beam issues for colliding schemes with large Piwinski angle and crabbed waist", LNF-07/003(IR), January 2007.

2.4 Beam Dynamics Issues in the SuperKEKB

Demin Zhou, Haruyo Koiso, Akio Morita, Kazuhito Ohmi, Katsunobu Oide, and Hiroshi Sugimoto
KEK, 1-1 Oho, Tsukuba, Ibaraki 305-0801, Japan
Yuan Zhang
IHEP, Beijing, China
Mail to: dmzhou@post.kek.jp

2.4.1 Introduction

Assuming 3D asymmetric Gaussian flat beams and neglecting hourglass effect, the luminosity of an electron-positron colliders is given by $\mathcal{L} = \mathcal{L}_0 R_\theta$ with

$$\mathcal{L}_0 = \frac{N_+ N_- f_c}{2\pi \sqrt{\sigma_{x+}^2 + \sigma_{x-}^2} \sqrt{\sigma_{y+}^2 + \sigma_{y-}^2}} \tag{1}$$

and the geometrical reduction factor

$$R_\theta = \frac{1}{\sqrt{1 + \frac{\sigma_{z+}^2 + \sigma_{z-}^2}{\sigma_{x+}^2 + \sigma_{x-}^2} \tan^2\left(\frac{\theta}{2}\right)}}, \tag{2}$$

where the subscripts of $+$ and $-$ respectively denote the positron and electron bunches, f_c is the bunch collision frequency, N is the bunch population, σ is the beam size in the horizontal (x), vertical (y) and longitudinal (z) directions, and θ is the full crossing angle. The transverse beam sizes at the interaction point (IP) are determined by $\sigma_{x,y}^* = \sqrt{\beta_{x,y}^* \epsilon_{x,y}}$, where ϵ is the beam emittance, and β is the beta function at the IP in each plane.

With the same assumptions for the luminosity formula, the beam-beam tune shifts for the electron beam are expressed by

$$\xi_{x-} = \frac{N_+ r_e \beta_{x-}}{2\pi\gamma_- \bar{\sigma}_{x+}(\sigma_{y+} + \bar{\sigma}_{x+})}, \tag{3}$$

$$\xi_{y-} = \frac{N_+ r_e \beta_{y-}}{2\pi\gamma_- \sigma_{y+}(\sigma_{y+} + \bar{\sigma}_{x+})}, \tag{4}$$

where r_e is the classical radius of electron, γ_- is the Lorentz factor for the electron beam, and $\bar{\sigma}_{x+} = \sigma_{x+}\sqrt{1 + \Phi_+^2}$ with Piwinski angle $\Phi_+ = \frac{\sigma_{z+}}{\sigma_{x+}}\tan\left(\frac{\theta}{2}\right)$. Reversing the signs of $+$ and $-$, the above equations also hold for the positron beam. For particles with zero longitudinal displacements in the electron beam, they feel a positron bunch with effective width of $\bar{\sigma}_{x+}$. The beam-beam tune shifts $\xi_{x,y}$ denote the strength of the interaction of colliding beams, and usually saturate at finite values while beam currents increase and transverse beam size blowup happens. With flat beams, usually the luminosity is mostly sensitive to the vertical beam sizes. For SuperKEKB, with large crossing angle and small vertical beta function, the beam-beam tune shift in the horizontal direction is much smaller than that in the vertical direction, namely $\xi_{x/y+} = 0.003/0.088$ and $\xi_{x/y-} = 0.001/0.081$ for positron and electron beams, respectively.

The SuperKEKB is designed with the strategy of so-called nanobeam scheme, which was originally proposed by P. Raimondi for SuperB [1]. The electron and positron beams collide with a horizontal crossing angle of $\theta = 83$ mrad. The horizontal emittances are $\epsilon_{x+} = 3.2$ nm and $\epsilon_{x-} = 4.6$ nm, taking into account the intra-beam scattering effects. The beam sizes at the IP are $\sigma_{x+} = 10.1\ \mu m$ and $\sigma_{x-} = 10.7\ \mu m$. The overlap area of the two beams is $\Delta s = \frac{2\sigma_x}{\theta} \approx 0.25$ mm, which is about 1/20 of the nominal bunch length. Another feature of SuperKEKB is the small vertical beta function at IP, which is squeezed to be $\beta_{y+}^* = 0.27$ mm and $\beta_{y-}^* = 0.3$ mm , comparable to the overlap area Δs. The vertical emittances are assumed to be $\epsilon_{y+} = 8.64$ pm and $\epsilon_{y-} = 12.9$ pm, taking into account various intensity-dependent and - independent effects. Comparing with its predecessor, the emittances of SuperKEKB rings are about 1/5 and 1/20, and the beta functions are about 1/40 and 1/50 of those of KEKB rings in the horizontal and vertical directions, respectively.

Since the KEKB rings, as reviewed in Refs. [2-4], have experienced many beam dynamics issues which affected the luminosity performance, it is expected that the luminosity performance of SuperKEKB, which will push the limit by a factor of 40, will be even more sensitive to various imperfections or perturbations, such as machine errors, lattice nonlinearity, intra-beam scattering, beam-beam interaction, space charge, impedance-driven instabilities, etc. Regarding to the beam dynamics issues associated to the electron-positron colliders, there are reviews in Refs. [5-7]. The progress of next generation B-factory projects has been reviewed in Refs. [8-10], and especially the most

recent status of SuperKEKB is discussed in Ref. [11]. This article is dedicated to discussing a few beam dynamics issues that might set challenges for the future commissioning of the SuperKEKB. For more information of other beam dynamics issues at SuperKEKB, such as intra-beam scattering, electron cloud effects, impedance effects, optics optimization, etc., the interested readers are directed to Refs. [12-16].

This article is extended from a conference paper presented at the 6th International Particle Accelerator Conference [17].

2.4.2 Beam Dynamics Issues

This section gives a brief overview of some important beam dynamics issues in SuperKEKB. Since most of these issues appear to be more prominent in the low energy ring (LER), we mainly use the LER for illustrations rather than the high energy ring (HER) in the following discussions.

2.4.2.1 *Intra-beam Scattering*

In the case of a low emittance ring with high bunch current, the effect of intra-beam scattering becomes significant, and can affect the equilibrium emittance, bunch length and energy spread. Figures 1 and 2 show these parameters as functions of the bunch population while keeping the nominal ratio of the vertical emittance fixed for SuperKEKB rings. The situations show similar emittance growth as that in SuperB [18]. Especially, in the LER there is an increase of more than 60% in the horizontal emittance, and about 5% in the bunch length and energy spread at the nominal bunch population of 9.04×10^{10}.
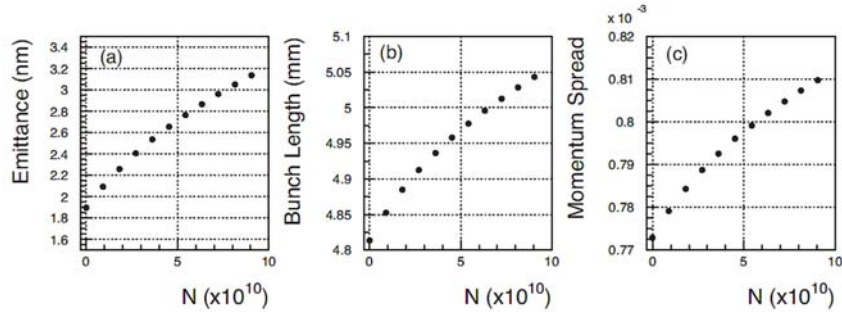
Figure 1: Effects of intra-beam scattering in the LER: (a) emittance, (b) bunch length, and (c) energy spread as a function of bunch population.
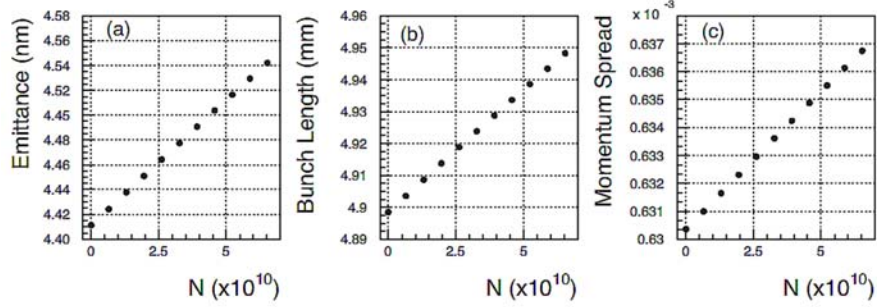
Figure 2: Effects of intra-beam scattering in the HER: (a) emittance, (b) bunch length, and (c) energy spread as a function of bunch population.

2.4.2.2 *Beam-beam Interaction*

It is well accepted that the 'sweet spot' in the tune space for achieving highest luminosity at an electron-positron collider usually locates at an area close to half integer. To search for the best working point in the tune space, luminosity scans are performed for both LER and HER, with the fractional tunes in the range of [0.5, 0.75] and the beam currents set to design values. The tune scan results of luminosity using a weak-strong model for the LER and HER are demonstrated in Fig. 3 with scaled colours, and Fig. 4 shows the relevant scans of vertical rms beam sizes. It is seen that the strong synchro-betatron resonances of $2v_x - Nv_s = Integer$ exist in the nanobeam scheme. This is due to the large crossing angle chosen for the purpose of mitigating hourglass effects. Furthermore, the resonances of $v_x + 2v_y + Nv_s = Intege$, $2v_y - Nv_s = Integer$, and $v_x - v_y - v_s = Intege$ also restrict the choice of working point. The working points have to be kept far enough from these strong resonances. In general, the luminosity is very sensitive to the vertical beam size. With higher beam energy, the electron beam in HER is more robust than the positron beam in LER with respect to the beam-beam driven synchro-betatron resonances. At present, both the main rings of the SuperKEKB are optimized with fractional tunes of [0.53, 0.57]. The working point is selected from islands isolated by the beam-beam resonance lines. But notice that the island areas might shrink when the lattice nonlinearity and machine errors strengthen those resonances [13].
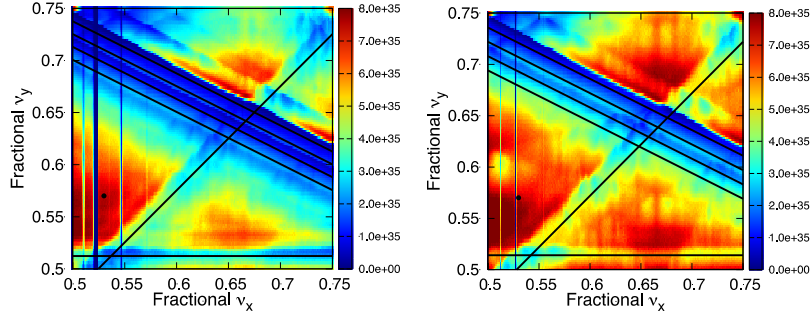
Figure 3: Tune scan of luminosity for the LER (left) and HER (right). The black dots and lines indicate the nominal working point and the various synchro-betatron resonances.
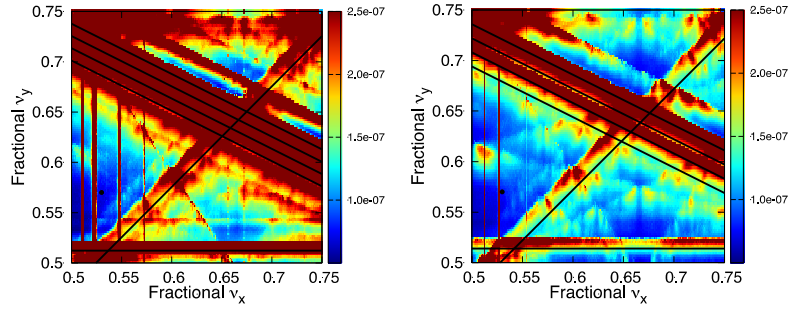
Figure 4: Tune scan of vertical rms beam size at IP for the LER (left) and HER (right). The black dots and lines indicate the nominal working point and the various synchro-betatron resonances.

2.4.2.3 *Lattice Nonlinearity*

For SuperKEKB, most of the unavoidable lattice nonlinearity is attributed to the interaction region resulting from the extremely small beta functions at IP and low emittances. For examples, the nonlinear terms from the drift space near IP, so called kinematic terms, and the Maxwellian fringe fields of final focus (FF) superconducting quadrupoles will become very important. The dynamic aperture (DA) limited by these terms in a circular collider has been studied in Refs. [19, 20]. The aperture in term of initial action variable is written as

$$J_y = \frac{\beta_y^{*2}}{(1+2|K_1|L^{*2}/3)L^*} A(\mu_y),$$ (5)

where L^* is the distance from the IP to the final quadrupole face, K_1 is the quadrupole strength, and $A(\mu_y)$ is a universal function in term of vertical phase advance μ_y, which has a meaning of tune shift in Ref. [20]. The relevant parameters are summarised for some colliders in Table 1, where the value of the scaling factor $J_y/A(\mu_y)$ indicates the difficulty of achieving large DA. It turns out that the SuperKEKB has the smallest β_y^*, and is likely the most challenging project. It is also noteworthy that, different from other projects, the FF quadrupole fringes of SuperKEKB are very strong and its effect on DA is even more severe than the kinematic terms.

Table 1: Important parameters limiting the dynamic aperture for some colliders. The parameters for CEPC and TLEP are typical design values.

Ring	β_y^* [mm]	K_1 [m^{-2}]	L^* [m]	J_y/A [μm]
SuperKEKB HER	0.3	-3.1	1.22	0.018
SuperKEKB LER	0.27	-5.1	0.76	0.032
CEPC	1.2	-0.176	1.5	0.76
TLEP	1	-0.16	0.7	1.36
KEKB	5.9	-1.779	1.762	4.22

In addition to the kinematic and FF quadrupole fringes, there are other important sources of lattice nonlinearity resulting from solenoids of 1.5 T field installed for particle detection. And anti-solenoid magnets, which almost overlay with FF quadrupoles, are adopted to compensate the detector solenoid fields. Due to the large crossing angle, the solenoid axis deviates from the beam axis, which generates unwanted fields acting on the beam. The fringe fields of the solenoids can induce the vertical emittance. The beam orbit is curved due to solenoid field in the LER. Consequently, the FF quadrupoles are shifted downside by 1.5 mm in the left side and 1.0 mm in the right side in order to reduce the dipole angle of the corrector coil to adjust the orbit as small as possible. The rotation of the FF quadrupoles around the beam axis and the skew quadrupole correctors are adopted to make the vertical dispersions and the X-Y couplings in IR as small as possible.

Furthermore, the natural chromaticity in SuperKEKB is very large, and approximately 80% of it in the vertical direction is generated by the FF system. So strong sextupoles are installed for chromaticity correction. To suppress the nonlinearity caused by the FF system, correction coils from dipole to octupole components are installed to each FF quadrupoles [21]. Even so, the IR is not transparent for off-momentum or large-amplitude particles. This is illustrated in Fig. 5. A particle is tracked through the LER with synchrotron radiation excitation and damping turned off. The initial conditions are varied by shifting the initial horizontal coordinates. When we observe the vertical motion in the phase space, we do see the vertical amplitude and even the closed orbit grow while the horizontal amplitude increases (see the middle in Fig. 5). This is a clear evidence of nonlinear horizontal-to-vertical coupling. We do the same tracking for a simplified lattice where we remove the solenoids, and simplify the arrangements on FF quadrupoles. It turns out the X-Y coupling disappears. So, we conclude that the solenoids do contribute to lattice nonlinearity in SuperKEKB.

2.4.2.4 *Space Charge*

The first-order space-charge tune shift experienced by particles performing small oscillations around the beam centroid in a uncoupled lattice and for a Gaussian bunch can be estimated by

$$\Delta \nu_i = -\frac{1}{4\pi}\frac{2r_e}{\beta^2\gamma^3}\int_0^C \frac{\lambda(s)\beta_i}{\sigma_i(\sigma_x+\sigma_y)}ds, \tag{6}$$

with β_x, β_y the beta functions, σ_x, σ_y the horizontal and vertical rms beam sizes, C the circumference of the ring, β the relative velocity, and $i = x, y$. The longitudinal peak density is $\lambda(s) = \frac{N}{\sqrt{2\pi}\sigma_z(s)}$ with gaussian bunch profile assumed. In the absence of linear coupling, the horizontal beam sizes are calculated from emittance via $\sigma_x^2 = \epsilon_x\beta_x + \langle\delta^2\rangle D^2$ with D the dispersion function.
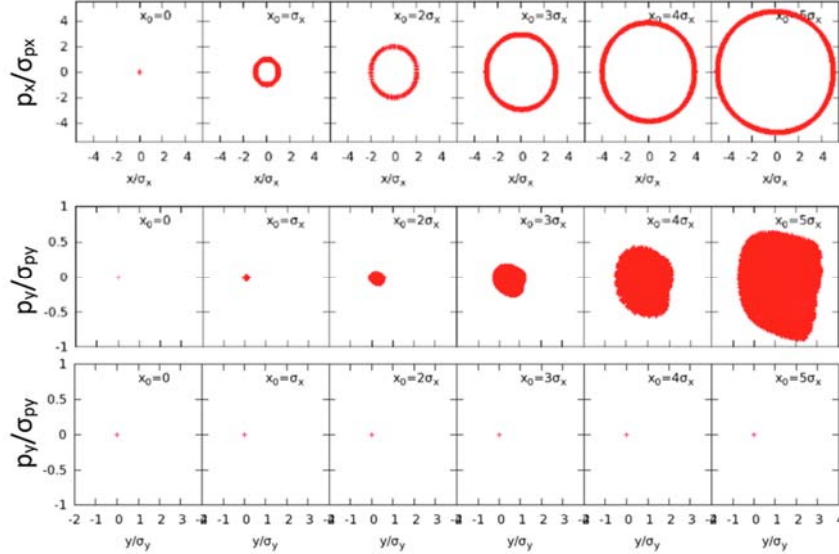
Figure 5: Poincare maps at the IP with increasing horizontal offset from the left to the right. Top: horizontal phase space. Middle: vertical phase space for a baseline lattice. Bottom: vertical phase space for a simplified lattice.

Table 2 summarizes the estimated beam-beam parameters $\xi_{x,y}$ and linear space charge tune shifts $\Delta\nu_{x,y}$ for SuperKEKB and KEKB rings, compared with the beam-beam tune shifts. It is seen that the space charge tune shifts are very small for KEKB. But for SuperKEKB LER, the space charge tune shift in the vertical direction is in the same level as beam-beam tune shift with opposite sign. Though the linear part can cancel each other, the amplitude-dependent tune shifts will not due to their different nonlinear behaviors. The betatron tune footprints for the LER with and without space charge are shown in Fig. 6. The simulations are done using SAD code [22] based a weak-strong model for space charge effect [23]. With working point set to be close to half-integer for seek of good luminosity, the particles will attracted to half-integer resonance and become unstable.

Table 2: Estimated beam-beam parameters and linear space charge tune shifts for the SuperKEKB and KEKB rings.

Parameter	SuperKEKB		KEKB	
	LER	**HER**	**LER**	**HER**
ϵ_x (nm)	3.2	4.6	18	24
ϵ_y (pm)	8.64	11.5	180	240
ξ_x	0.0028	0.0012	0.127	0.102
ξ_y	0.088	0.081	0.129	0.09
$\Delta\nu_x$	-0.0027	-4e-4	-5e-4	-3e-5
$\Delta\nu_y$	-0.094	-0.012	-0.0072	-4e-4
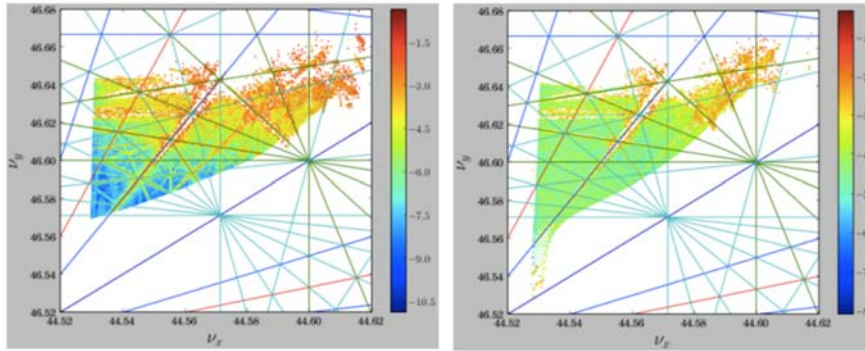
Figure 6: Betatron tune footprint for a baseline lattice of LER without (left) and with (right) space charge effect. Resonance lines from 4th to 7th orders are also plotted.

2.4.3 Interplay of Beam-Beam with Lattice Nonlinearity and Space Charge

2.4.3.1 *Lattice Nonlinearity*

Beam-beam interaction may interplay with lattice nonlinearity and cause luminosity loss [13], and its effect in some machines has been reviewed in Ref. [24]. To evaluate its effect, the SAD code is utilized to do element-by-element tracking simulations with the beam-beam element inserted at the IP. The total one-turn map used in the simulations can be represented by

$$M = M_{rad} \circ M_{bb} \circ M_0, \tag{7}$$

where M_{bb} and M_{rad} are maps for the beam-beam interaction and radiation damping/quantum excitation, respectively. And M_0 indicates the transfer map felt by a particle when it travels through normal magnetic and electromagnetic components along the ring. The lattice nonlinearity is naturally included in M_0 when a realistic lattice is loaded into the SAD code. Another method for the simulations with momentum-dependent lattice nonlinearity was discussed in Refs. [25, 26], where a symplectic formalism was developed to describe the perturbation maps for the chromatic aberrations. In that method, the momentum-dependent lattice nonlinearities are lumped to the IP and then used for tracking simulations.

The specific luminosity as a function of bunch current products is shown in Fig. 7. In the figure, the red solid lines indicate the results of using pure weak-strong model.

The blue dashed lines indicate results of using the weak-strong model plus perturbations of chromatic aberrations. The green dashed lines indicates results of using SAD code with weak-strong model. The cyan lines represent the design values of luminosity and beam current products. It is seen that remarkable loss of luminosity appears at high bunch currents due to interplay of beam-beam and lattice nonlinearity in the LER. Especially, the specific luminosity drops quickly at very low beam currents. These phenomena cannot be explained by the momentum-dependent lattice nonlinearity. One possibility is that amplitude-dependent nonlinearities play an important role in the LER. On the other hand, the luminosity loss due to interplay of beam-beam and lattice nonlinearity in the HER is not as serious as in the LER, and can be well attributed to the chromatic aberrations in the HER lattice.
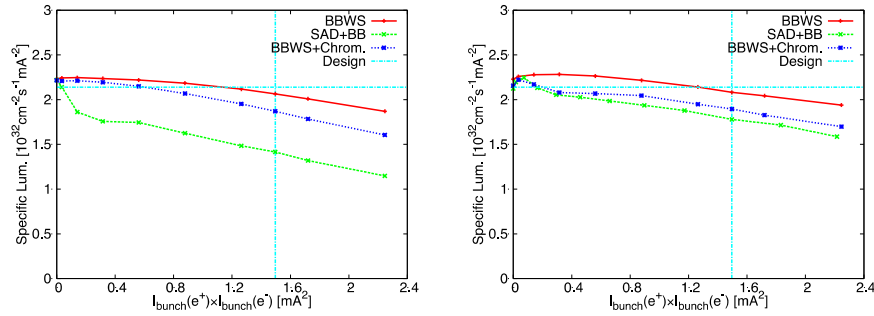
Figure 7: Specific luminosity as a function of bunch current products. Left picture is for LER, and right picture is for HER.

To further illustrate how lattice nonlinearity interplays with beam-beam interaction, the standard frequency map analysis (FMA) is performed for three cases: bare lattice, pure beam-beam, and beam-beam with lattice nonlinearity. The initial conditions are taken over a mesh in the horizontal (x) and vertical direction (y) inside an area of $10\sigma_x \times 10\sigma_y$, and the corresponding tune footprints are plotted in the tune plane. The color indicates the diffusion rate of the particle motion. Figures 8 shows the FMA results for LER and HER. In each figure, the dots starting from the origin [0.53, 0.57] indicate the footprints for a bare lattice; the black dots indicate footprints for pure beam-beam; the rest dots represent footprints for beam-beam with lattice nonlinearity. In the same figures, resonance lines up to eighth order are also plotted for reference.
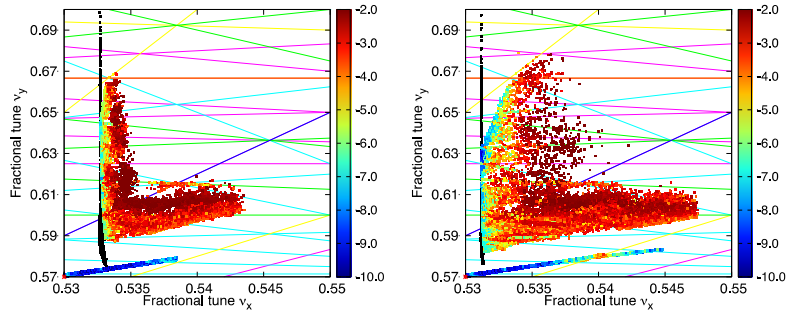
Figure 8: FMA plot in the plane of betatron tunes. Left picture is for LER, and right picture is for HER.

From the frequency maps, the footprints in tune space with the bare lattice show strong dependence on initial amplitude. These are the results of strong amplitude-

dependent lattice nonlinearity in both rings. The pure beam-beam interaction causes large spread in the horizontal tunes while very small spread in the horizontal tune. The footprints are strongly deteriorated by the interplay between lattice nonlinearity and beam-beam. Particles with initial amplitudes of several sigmas perform very chaotic motion with large diffusion rate. The resonances driven by beam-beam are not clearly seen when lattice nonlinearity is included, because the particle motions become strongly chaotic.

   Figures 9 and 10 show the dynamic aperture calculated by particle tracking using SAD for the LER and HER with and without beam-beam interaction [16]. For the LER, the DA is reduced significantly compared with that without the beam-beam effect. The Touschek lifetime is calculated from the fitted sizes of DA. Without beam-beam, the Touschek lifetime is about 600 s for both LER and HER, and almost satisfies the requirement from injection. But with beam-beam, the Touschek lifetime will reduce by around 10% and 85% for HER and LER, respectively. Moving the working point to be closer to half-integer can partially recover the lifetime for LER, but the loss rate is still more than 50%.
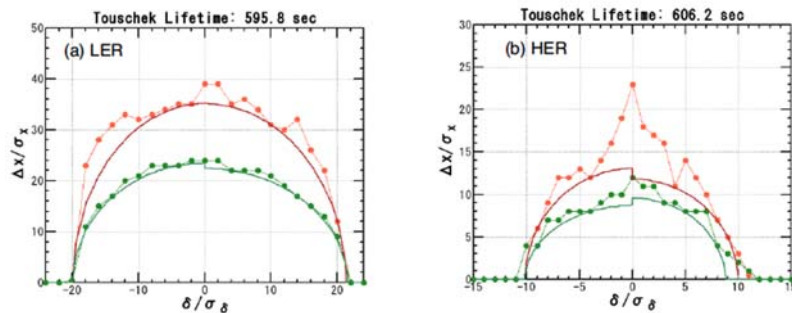
Figure 9: Dynamic aperture for LER (left) and HER (right) without beam-beam.
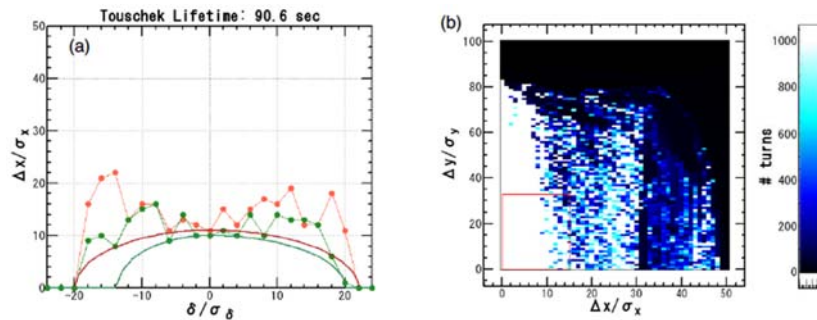
Figure 10: Dynamic aperture for LER with beam-beam in the horizontal-momentum plane (left) and in the horizontal-vertical plane (right). The red square indicates the required injection aperture.
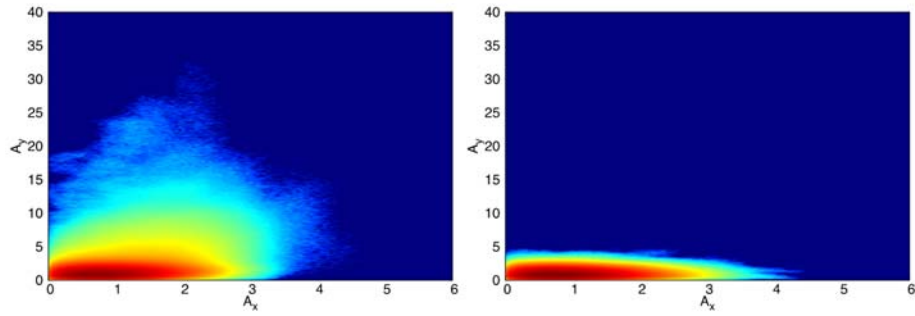
Figure 11: Beam tail simulated by BBWS without (left) and with (right) crab waist.

Beam-beam interaction with large crossing angle can generate beam tails [27] that is unwanted by the particle detector. From the comparison of beam tail simulations with pure beam-beam interaction and with lattice nonlinearity included, see the left figures of Figs. 11 and 12, the interplay of beam-beam and lattice nonlinearity does enhance the beam tail of the positron beam in LER. This will cause additional challenges to the collimation system for protection of particle detector.
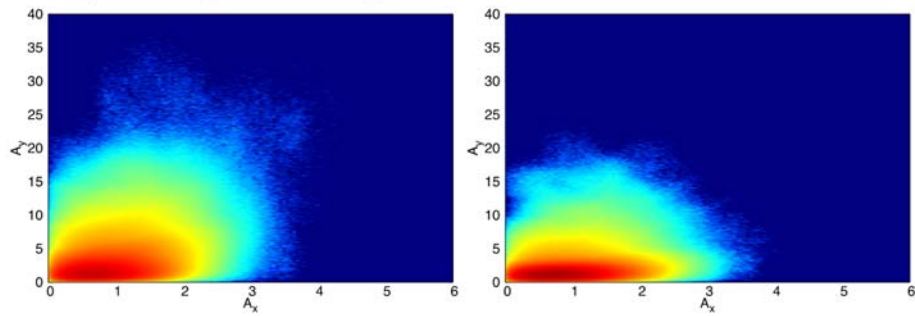
Figure 12: Beam tail simulated by SAD for a baseline lattice of LER without (left) and with (right) ideal crab waist.

2.4.3.2 *Space Charge*

As shown by the frequency map analysis in Fig. 6, the space charge forces drive the particles toward half-integer while beam-beam acts on the opposite direction. When these two forces add on each other, they will create strongly distorted footprints for the particles in the tune space (see Fig. 13). Note that here we used a weak-strong model for space charge, and the blow up in beam sizes is not taken into account. Therefore the simulations are not self-consistent, and overestimate the space charge effects.
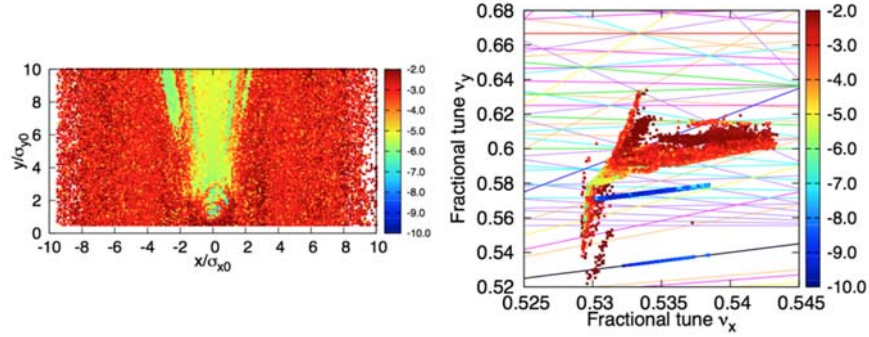
Figure 13: FMA for a baseline lattice with space charge. Left is for the physical space and right is for the tune space. Resonance lines up to 10th orders are also plotted.

The specific luminosity as a function of bunch current products are simulated using BBWS and SAD, as shown in Fig. 14. Adding to the lattice nonlinearity, space charge does cause additional luminosity loss, though its effect is overestimated due to the use of a weak-strong model. It is interesting to observe that space charge does compensate beam-beam effect at low beam currents (see the left of Fig. 14), where the nonlinear effects of these two forces are not significant. For a simplified lattice with solenoids removed and FF quadrupoles simplified, see the right of Fig. 14, the interplay of beam-beam with lattice nonlinearity and space charge relaxes in response to less nonlinearity. Therefore, it is concluded that the nonlinear fields from solenoids and consequent re-arrangements of FF quadrupoles play an important role at SuperKEKB.
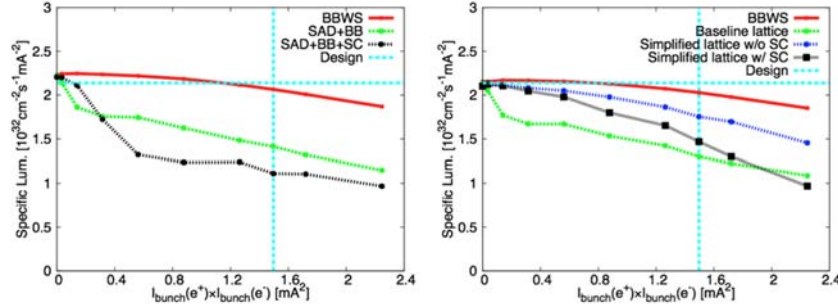
Figure 14: Specific luminosity as a function of bunch current products for the LER. The cyan lines indicate design values. The left and right figures have slight differences in nominal beam parameters.

2.4.3.3 *Detuned Lattice*

Detuned lattices will be used in the phase 2 operation of SuperKEKB without VXD detector. For these lattices of LER and HER, the vertical and horizontal beta functions at the IP will be 4 and 8 times the values of baseline lattice. We check the effects of beam-beam, lattice nonlinearity and space charge for the detuned lattice of LER, and the results are summarized in Fig. 15. It turns out both space charge and lattice nonliearity will be much less important for the detuned lattices. Achieving the target luminosity of 1×10^{34} cm^{-2}s^{-1} is very promising, and reaching the value of 1×10^{35} cm^{-2}s^{-1} might also be possible by increasing the beam currents.
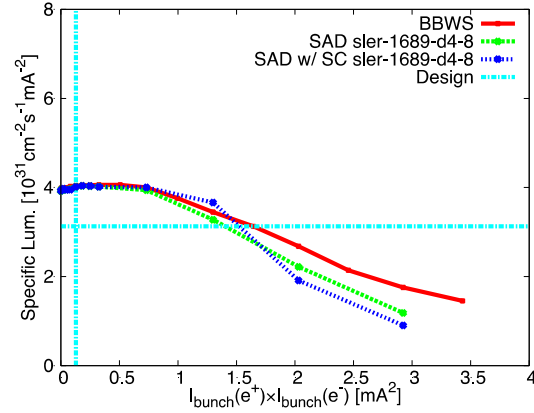
Figure 15: Specific luminosity as a function of bunch current products for the detuned lattice of LER. The cyan lines indicate design values.

2.4.4 Mitigation Schemes

The crab waist is the most promising technique for suppressing the beam-beam resonances in the nanobeam scheme [1, 5, 27]. As stated in Ref. [5], the crab waist transformation gives a small geometric luminosity gain (around 10% for SuperKEKB) due to the vertical beta function redistribution along the overlap area. However, the dominating effect comes from the suppression of betatron and synchro-betatron resonances arising from the vertical motion modulation by the horizontal betatron oscillations. This is demonstrated by the weak-strong simulations for the positron beam as shown in Figs. 11 and 16. At the same time, there will be more choices for working point in the tune space.

In the present design of SuperKEKB, crab waist is not adopted because the lattice nonlinearity in the IR is very strong and always cause severe loss of DA and lifetime when crab waist sextupoles are put into the real lattice. For detailed studies of crab waist scheme applied to SuperKEKB, see Ref. [16]. Even with the ideal crab waist put at the IP in a real lattice, the lattice nonlinearity still can weaken the its power in suppressing in the beam-beam tails, as shown in the right figure of Fig. 10. All studies strongly suggest that the nonlinear optimization of the real lattices is a must for successful application of crab waist to SuperKEKB. Unfortunately, this is not very successful up to now. We expect advanced nonlinear analysis techniques (see Ref. [28] for an example), applied to the SuperKEKB lattices. With the existing successful experiences of suppressing lattice nonlinearity by installing skew-sextupoles in KEKB [2, 3] and installing octupoles in DAΦNE [29], we will consider using additional octupoles and even higher-order multipoles in the nonlinear optimizations.

As shown in the discussions of the previous sections, a comparison of the simulations results for the detuned and baseline lattices lead us to conclude that all the nonlinear effects depend strongly on β_y^*. It is worthwhile to try to relax β_y^* at IP, and perform overall optimizations of the key machine parameters. In this procedure, we will probably lose something in beam-beam, but gain in other nonlinear effects. Finally, some compromise can be reached. Besides, a moderate bunch length variation should also be tried.

For space charge effects, compensation of the linear tune shift is not enough. The amplitude-dependent tune shift also needs to be compensated by dedicated magnets such as octupoles.
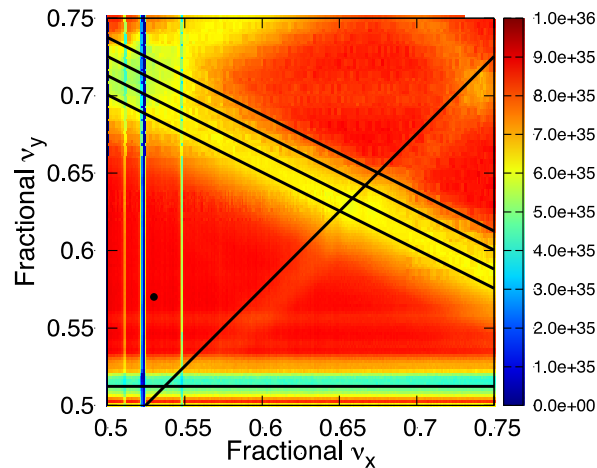
Figure 16: Tune scan of luminosity for LER with crab waist. The black dots and lines indicate the nominal working point and the various synchro-betatron resonances.

2.4.5 Summary and Future Plans

The recent design studies of SuperKEKB show that many beam dynamics issues might affect its final luminosity performance and set challenges to the beam commissioning. For examples, the lattice nonlinearity set limit to the dynamic aperture and Touschek lifetime, interplay with beam-beam and cause luminosity loss, and impede the success of applying crab waist. In the LER, space charge is a new issue and its importance has just been recognized recently.

To remedy these challenges, we plan to perform detailed analysis of lattice nonlinearity in SuperKEKB under an international collaboration program. Connecting the ongoing study efforts on SuperKEKB with the design efforts of future circular colliders will benefit both sides.

2.4.6 Acknowledgements

2.4.7 References

1. P. Raimondi, "Status on SuperB effort", 2nd LNF Workshop on SuperB, 16-18 Mar. 2006, LNF, Frascati, Italy.
2. Y. Funakoshi et al., "Achievements of KEKB", Prog. Theor. Exp. Phys. 2013, 03A001.
3. Y. Funakoshi et al., "Commissioning of KEKB", Prog. Theor. Exp. Phys. 2013, 03A010.
4. K. Oide, "KEKB B-Factory, The Luminosity Frontier", Prog. Theor. Phys., Vol. 122, No. 1, July 2009.
5. M. Zobov, "New generation electron-positron factories", Phys. Part. Nucl. 42 (2011)

782-799.

6. K. Oide, "Electron-Positron Circular Colliders", in "Reviews of Accelerator Science and Technology", Vol. 7 (2014) 35-48.
7. F. Zimmermann, "Collider Beam Physics", in "Reviews of Accelerator Science and Technology" Vol. 7 (2014) 177-205.
8. M. Masuzawa, "Next Generation B-Factories", FRXBMH01, IPAC'10, Kyoto, Japan, 2010.
9. M. E. Biagini, "Overview of B-Factories", WEYA03, IPAC'12, New Orleans, USA, 2012.
10. K. Akai, "Progress in Super B-Factories", TUYB101, IPAC'13, Shanghai, China, 2013.
11. T. Miura et al., "Progress of SuperKEKB", FRXC1, IPAC'15, Richmond, VA, USA, 2015.
12. Y. Ohnishi et al., "Accelerator design at SuperKEKB", Prog. Theor. Exp. Phys. 2013, 03A011.
13. D. Zhou et al., "Crosstalk Between Beam-beam Interaction and Lattice Nonlinearities in the SuperKEKB", TUPME016, IPAC'13, Shanghai, China, 2013.
14. K. Ohmi et al., "Study of Electron Cloud Effects in SuperKEKB", TUPRI020, IPAC'14, Dresden, Germany, 2014.
15. D. Zhou et al., "Impedance Calculation and Simulation of Microwave Instability for the Main Rings of SuperKEKB", TUPRI021, IPAC'14, Dresden, Germany, 2014.
16. "SuperKEKB Technical Design Report", 2014, to be published.
17. D. Zhou et al., "Interplay of Beam-Beam, Lattice Nonlinearity, and Space Charge Effects in the SuperKEKB Collider", WEYB3, IPAC'15, Richmond, VA, USA, 2015.
18. T. Demma and M. Pivi, "Collective Effects in the SuperB Collider ", IPAC'10, Kyoto, Japan, 2010.
19. K. Oide and H. Koiso, "Dynamic aperture of electron storage rings with noninterleaved sextupoles", Phys. Rev. E 47, 2010 (1993).
20. K. Ohmi, "Dynamic aperture limit caused by IR nonlinearities in extremely low beta B factories", TUPEB015, IPAC'10, Kyoto, Japan, 2010.
21. H. Sugimoto et al., "Design study of the SuperKEKB interaction region optics", TUOAB02, IPAC'14, Dresden, Germany, 2014.
22. http://acc-physics.kek.jp/SAD/.
23. M. Venturini and K. Oide, "Direct space-charge effects on the ILC damping rings: Task Force Report", LBNL-59511, February 2006.
24. Y. Zhang et al., "Review of crosstalk between beam-beam interaction and lattice nonlinearity in colliders", THAMH2, SAP2014, Lanzhou, China, 2014.
25. D. Zhou et al., "Simulations of beam-beam effect in the presence of general chromaticity", Phys. Rev. ST Accel. Beams 13, 021001 (2010).
26. Y. Seimiya et al., "Symplectic Expression for Chromatic Aberrations", Prog. Theor. Phys. (2012) 127 (6): 1099-1119.
27. D. Shatilov et al., "Beam-beam simulations for super B-factories with asymmetrical LER and HER lattice parameters", SB-NOTE-ACC-2008-02 (2008).
28. E. Forest et al., "Sources of amplitude-dependent tune shift in the PEP-II design and their compensation with octupoles", EPAC 1994 and LBL-35791 (1994).
29. M. Zobov, "Crosstalk between beam-beam effects and lattice nonlinearities in DAPhNE", arXiv:physics/0311129 [physics.acc-ph], 2003.

2.5   Status and Challenges of CEPC Accelerator Design

Yuan Zhang, Huiping Geng, Yiwei Wang and Dou Wang
IHEP, Beijing 100049, China
Mail to: zhangy@ihep.ac.cn, genghp@ihep.ac.cn, wangyw@ihep.ac.cn, wangd93@ihep.ac.cn

2.5.1   Introduction

After the discovery of a Higgs-like boson at CERN [1, 2, 3], many proposals have been made to build a Higgs factory to explicitly study the properties of this key particle. One of the most attractive proposals is the Circular Electron and Positron Collider (CEPC) project in China [4, 5, 6]. The present main parameters of CEPC are shown in Table 1.

CEPC is a ring with a circumference of 54.7 km to house an electron - positron collider in phase-I and be upgraded to a super proton-proton Collider (SPPC) in phase-II.

The designed beam energy for CEPC is 120 GeV. The target luminosity is ~10^{34} cm^{-2}s^{-1}. The main constraint in the design is the synchrotron radiation power which should be limited to 50 MW per beam, and beam lifetime which should be longer than 30 minutes.

CEPC will have arcs and straight sections between them.   RF cavities compensate the energy loss in the straight section, thus one can reduce energy variations from synchrotron radiation. SPPC needs long straight sections for collimators. The compromise between the requirements of the CEPC and the SPPC are to have 8 arcs and 8 straight sections; RF cavities will be distributed in each straight section.

Table 1: Main parameters of CEPC.

Parameter	Unit	value
Beam energy [E]	GeV	120
Circumference [C]	m	5,4752
Luminosity [L]	$cm^{-2}s^{-1}$	2.04×10^{34}
SR power/beam [P]	MW	51.7
Bending radius [ρ]	m	6094
Number of IP [N_{IP}]		2
Bunch number [n_B]		50
momentum compaction factor [α_p]		3.36×10^{-5}
Energy acceptance	%	2
cross-section for radiative Bhabha scattering [σ_{ee}]	cm^2	1.52E-25
lifetime due to radiative Bhabha scattering [τ_L]	min	50.61
Beam current [I]	mA	16.6
Bunch population [N_e]		3.79E+11
emittance-horizontal [$\acute{\epsilon}_x$]	m•rad	6.12E-09
emittance-vertical [ϵ_y]	m•rad	1.84E-11
coupling factor [κ]		0.003
Bunch length SR [$\sigma_{s.SR}$]	mm	2.14
Bunch length total [$\sigma_{s.tot}$]	mm	2.65
Betatron function at IP-vertical [β_y]	m	0.0012
Betatron function at IP-horizontal [β_x]	m	0.8
Transverse size at IP [σ_x]	μm	69.97
Transverse size at IP [σ_y]	μm	0.15
Beam-beam parameter [ξ_x]		0.118
Beam-beam parameter [ξ_y]		0.083
Hourglass factor [Fh]		0.68
Lifetime due to Beamstrahlung-Telnov [τ_{BS}]	min	1005
Lifetime due to Beamstrahlung [simulation]	min	47
RF voltage [V_{rf}]	GV	6.87
RF frequency [f_{rf}]	GHz	0.65
RF Energy acceptance	%	5.99
SR loss/turn [U_0]	GeV	3.11
Energy spread SR [$\sigma_{\delta.SR}$]	%	0.13
Energy spread BS [$\sigma_{\delta.BS}$]	%	0.09
Energy spread total [$\sigma_{\delta.tot}$]	%	0.16
Average number of photons emitted per electron during the collision [n_γ]		0.22

2.5.2 Beam-beam Effect

2.5.2.1 *Beamstrahlung*

When two head-on colliding electron and positron beams penetrate each other, every particle in each beam will feel the electromagnetic field of the other beam and will be deflected. This deflection process has some undesirable effects. Firstly, the deflected particle will lose part of its energy due to the synchrotron radiation, called as beamstrahlung, which will increase the energy spread of the colliding beams, and hence increase the uncertainty of the physical experiments. If the beamstrahung is so strong that particles' energy after collision is beyond the ring's energy acceptance, beam lifetime will be reduced. Secondly, the deflected particles will emit photons, hadrons, etc., which will increase the noise background level in the detector. Additionally, after the collision particles will change their flying direction with respect to the axis by a certain angle. If this angle is large enough the particles after the collision will interfere with the detection of small-angle events.

V. I. Telnov [7] pointed out that at energy-frontier e+e− storage ring colliders, beamstrahlung determines the beam lifetime through the emission of single photons in the tail of the beamstrahlung spectra. For the linear collider, the long tails of the beamstrahlung energy loss spectrum are not a problem because beams are used only once. For CEPC, if we want to achieve a reasonable beamstrahlung-driven beam lifetime of at least 30 minutes, we need to confine the particle density per bunch and also design a lattice with enough energy acceptance which is not smaller than 2%. We use the analytic formulas [7] to calculate the beamstrahlung lifetime and we also have done simulations. There exist clear differences between the two approaches.

2.5.2.2 *Radiative Bhabha Scattering*

In CEPC, lifetime due to radiative Bhabha scattering is also dominant. We use the following analytic formula to calculate the cross section of the radiative Bhabha process.

$$\sigma_{ee} = \frac{16\alpha r_e^2}{3}\left((\ln\frac{1}{\eta}+\eta-\frac{3}{8}\eta^2-\frac{5}{8})[\ln(\sqrt{2}\frac{a}{\lambda_p})+\frac{\gamma_E}{2}]+\frac{1}{4}(\frac{13}{3}\ln\frac{1}{\eta}+\frac{13\eta}{3}-\frac{3}{2}\eta^2-\frac{17}{6})\right),$$

$$a = \sqrt{2}\frac{\sigma_x\sigma_y}{\sigma_x+\sigma_y}.$$

(1)

Here, λ_p and γ_E denote the electron Compton wavelength and Euler's constant. The cross section of the radiative Bhabha scattering in CEPC is 1.52×10^{-25}cm^2. We also used the simulation code BBBrem to calculate the cross section: the results are very close to the ones from the analytic formula.

The beam lifetime due to radiative Bhabha scattering is expressed by:

$$\tau_L = \frac{I}{eLn_{IP}\sigma_{ee}f_0}$$

(2)

From the above expression, we can see that the lifetime is inversely proportional to the luminosity. For CEPC design, the lifetime due to radiative Bhabha scattering is 55 min with 2 IPs.

2.5.2.3 *Beam-beam Simulation*

2.5.2.3.1 Simulation Codes

We have used three simulation codes:
- LIFETRAC [8] - developed by Dmitry Shatilov at BINP (weak-strong code).
- BBWS/BBSS [9,10] - developed by Kazuhito Ohmi at KEK (BBWS is a weak strong code, and BBSS is a strong-strong code.).
- IBB- developed by Yuan Zhang at IHEP (strong-strong code).

2.5.2.3.2 Choice of Working Point

Since the working point is very important for luminosity optimization, a tune scan is necessary and the result obtained by BBWS is shown in Figure 1, where the highest luminosity per IP is about $1.9 \times 10^{34} cm^{-2} s^{-1}$.
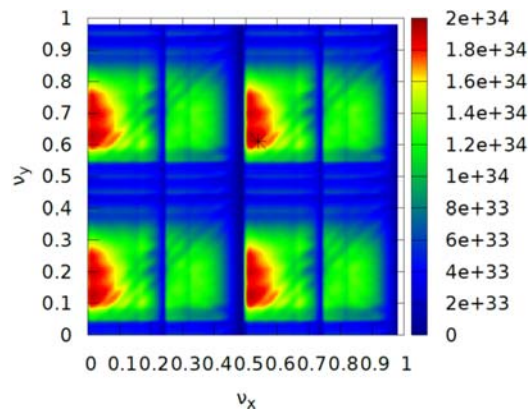
Figure 1: Luminosity per IP versus the transverse tune of half ring. The star mark is positioned at (0.54, 0.61).

The luminosity behavior is also checked with the strong-strong simulation (BBSS) at some working points, see Figure 2. It seems that (0.54, 0.61) for the half ring is a good choice, the luminosity per IP is about $1.7 \times 10^{34} cm^{-2} s^{-1}$.
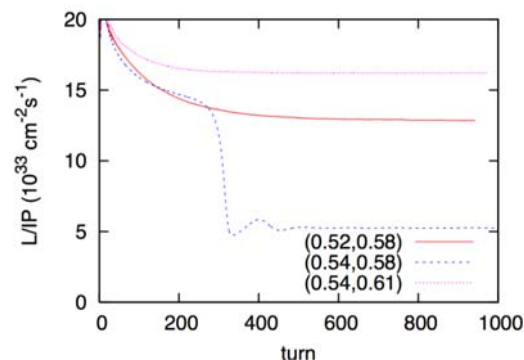
Figure 2: Luminosity behavior at different working points

2.5.2.3.3 Luminosity and Lifetime

How the luminosity, beam distribution and lifetime vary with the bunch current is very important and will help evaluate if the design goal are achievable. Figure 3 shows

the luminosity and beam-beam parameter versus bunch current. It is shown that the luminosity with the designed bunch current is about $1.7 \times 10^{34} cm^{-2} s^{-1}$. The effective beam-beam parameter is only about 0.045 with design parameters and the saturation is very clear near the design bunch current. The bunch length is nearly 3 times of βy*, which causes a strong hourglass effect.
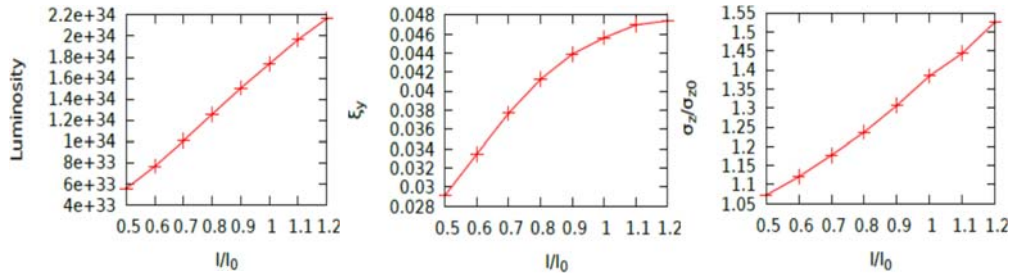
Figure 3: Luminosity/effective beam-beam parameter/bunch lengthing versus the bunch current. (LIFETRAC simulation).

Taking into account the limited momentum acceptance, the lifetime would be reduced by the larger energy spread, especially the long tail of beamstrahlung photon spectrum. The beamstrahlung lifetime is shown in Figure 4. LIFETRAC shows that it is about 85 min with momentum acceptance 0.02 at design bunch current. The BBWS's result is about 3 times longer.
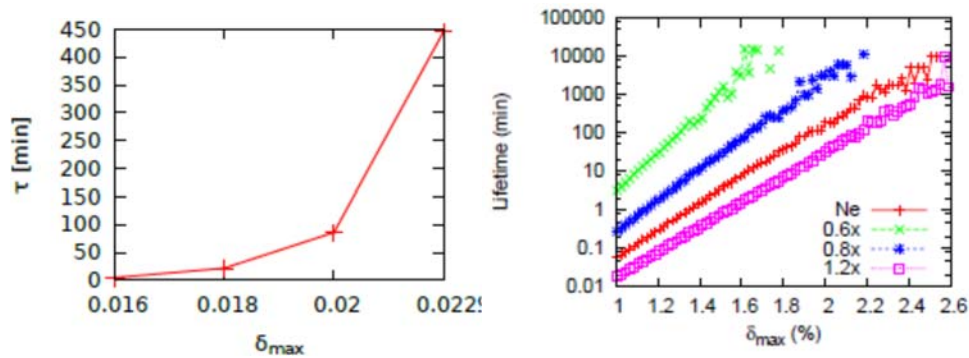
Figure 4: Beamstrahlung lifetime obtained by LIFETRAC (left) and from equilibrium distribution with BBWS(right) for different bunch populations. The horizontal axis is the momentum acceptance.

The transverse dynamic aperture also reduces the lifetime. Figure 5 shows the simulation result in the vertical direction. The lifetime is about 250/20 min for 50/40 σ_y by LIFETRAC. The BBWS result is about 6 times longer.

60
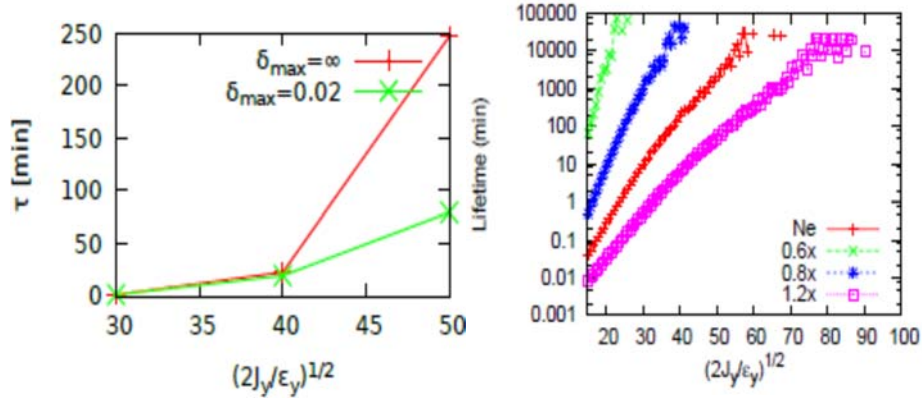
Figure 5: Lifetime limited by vertical aperture. The left hand figure is obtained by LIFETRAC for the design bunch current. The right hand figure is obtained from the equilibrium distribution with BBWS for different bunch populations.

Concerning dynamic effects, the beta function and emittance will be changed due to beam collision. The beam-beam simulation results shown in Figure 6 indicates the luminosity dependence on βy^* is quite different from the geometric luminosity. When βy^* is increased from 1.2 mm to 3 mm, the geometric luminosity (the light blue line) decreases as expected. But the luminosity from simulation for $\beta x = 0.8$ m (the red line) is increased to 2×10^{34} cm^{-2}s^{-1} because the actual βx from dynamic effects is reduced significantly.
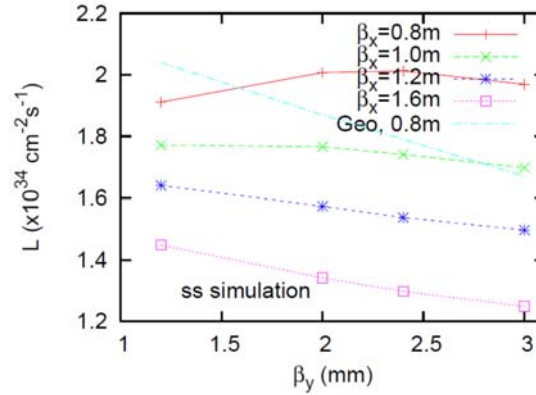
Figure 6: Dependence of Luminosity on βy^* for different values of βx.

As a summary, CEPC peak luminosity can reach $2 \times 10^{34} cm^{-2} s^{-1}$/IP based on beam-beam simulations. To ensure that the beam lifetime is reasonable, a dynamic aperture $20\sigma x \times 50\sigma y$ with $\delta max = 0.02$ is required.

2.5.3 Lattice

2.5.3.1 *Arc*

The circumference of the ring is about 54 km with 8 arcs and 8 straight sections. The layout of the ring is shown in Figure 7. There are four IPs in the ring, IP1 and IP3

will be used for CEPC, while IP2 and IP4 will be used for SPPC. The RF sections are distributed in each straight section.
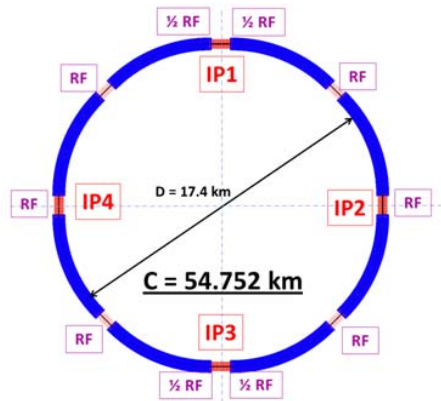
Figure 7: Layout of the CEPC main ring.

The lattice for CEPC arc has been chosen to use the standard FODO cells with 60 degrees phase advances in both transverse planes. The length of each bend is 19.6m, the length of each quadrupole is 2.0m. The total length of each cell is 47.2 m. The dispersion suppressors are formed by pulling out the bending magnets in the second last 60° FODO cell on each side of every arc section in CEPC ring. The twiss parameters of arc cell and dispersion suppressor are shown in Figure 8 and Figure 9 respectively. All the straight sections have almost same structure as arc with standard FODO cells.
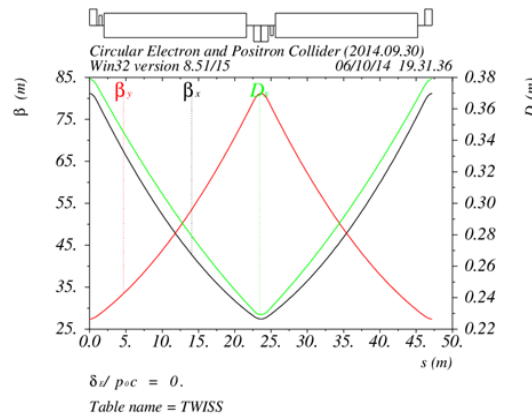
Figure 8: Twiss parameters of CEPC arc cell with 60/60 degrees phase advance.
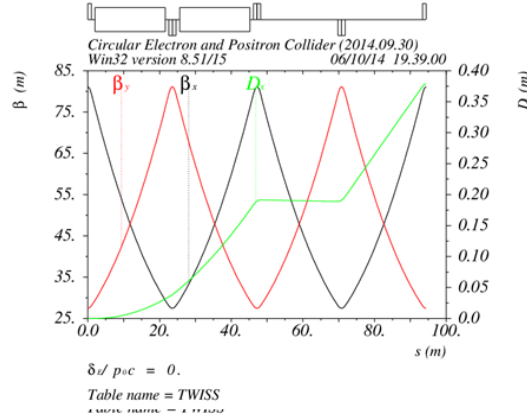
Figure 9: Twiss parameters of dispersion suppressor.

2.5.3.2   *Final Focus*

Producing low-β functions at the IP requires the design to locate the final focus quadrupole doublets as close as possible to the IP. The CEPC final focus (FF) has been designed with this principle, using the experience gained in designing the linear collider final focus. The design parameters for the β function at the IP are 800mm in the horizontal plane and 1.2mm in the vertical plane, with a distance (L*) between the IP and the first FF quadrupole magnet of 1.5 m.

Due to the large β values in the first FF doublets, the FF quadrupole magnets generate large chromaticity, which should be corrected as locally as possible. This is accomplished in the CEPC FF design by using a pair sextupoles in each plane, and each pair being connected with a -I transformation matrix. Two identical weak sextupole magnets are attached with the main local chromaticity correction sextupoles (with about 10% of their intensities) to correct the nonlinear effect of sextupole length.

The final focus system is a telescopic transfer line, starting from the IP, which includes: a final telescopic transformer (FT), chromaticity correction section in the vertical plane (CCY), chromaticity correction section in the horizontal plane (CCX) and matching telescopic transformer (MT). This is shown in Figure 10. We use the longitudinal cyclical symmetry of CCY and CCX to adjust the phase advances between the final doublet and the sextupoles to minimize second order chromaticity [11]. The chromatic functions along the final focus are also shown in Figure 10. The residual *WW* functions are W_xW_x=6.6, W_yW_y=5.6 and second order dispersion is $D_xD'_x$ = -0.15 m.
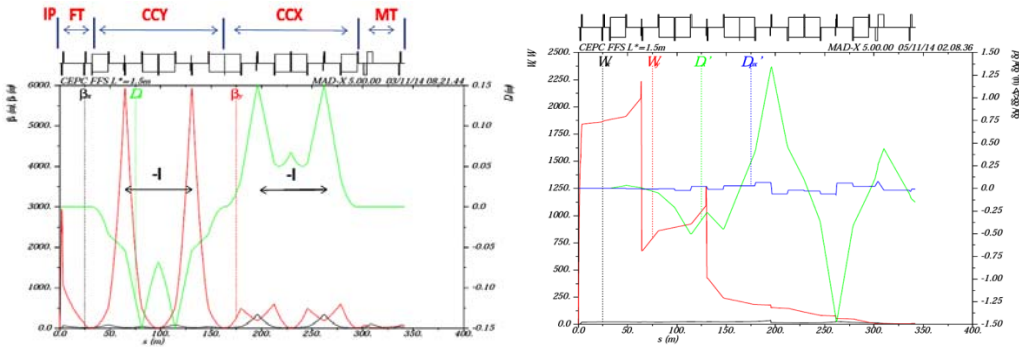
Figure 10: Lattice functions and chromatic functions of the final focus [12].

Inserting the final focus into the ring, the Twiss functions of the whole ring are shown in Figure 11, where the peak of β_y occurs at the two IPs. The two families of sextupoles in the ARC were re-matched to obtain as larger bandwidth as possible. The results of chromaticity correction are shown in Figure 12 (left).

As shown in the beam-beam simulation, the luminosity will not be reduced much when βy* is increased from 1.2mm to 3mm. We also got a preliminary IR design for βy*=3mm by simply re-matching the final telescopic transformer and the sextupoles. The results of chromaticity correction are shown in the right figure of Figure 12.
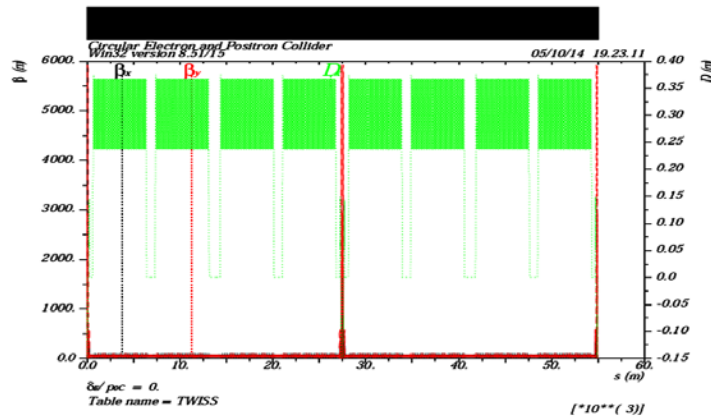
Figure 11: Lattice functions of the ring [12].
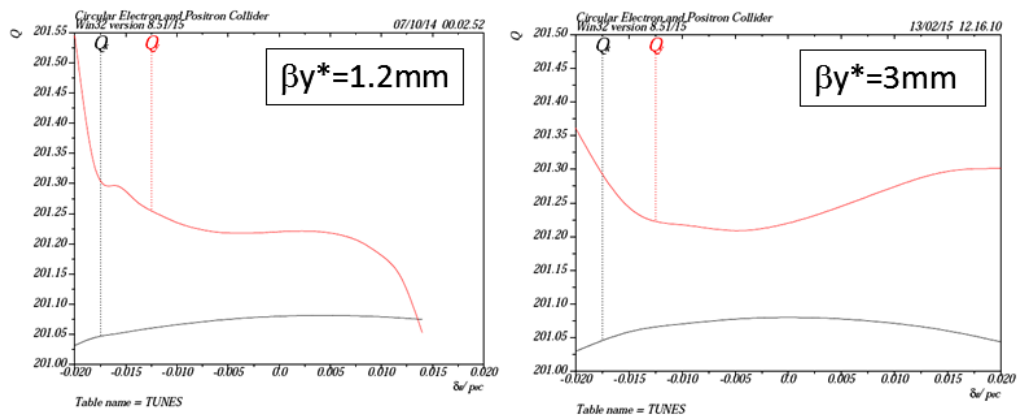
Figure 12: Tune vs. energy deviation [12].

2.5.3.3 *Dynamic Aperture*

The dynamic aperture (DA) for the whole ring was estimated numerically with the six-dimensional tracking code SAD [13]. The particles were tracked for 240 turns which corresponds to three transverse damping times, including synchrotron motion but without radiation damping, nor any magnet errors. The results of DA are shown in Figure 13. As expected, the dynamic aperture of 3mm βy* is larger than that of 1.2 mm βy*, but it's still small. So far, the dynamic aperture is a bottleneck for CEPC design study. Our goal is: 20σx×50σy for off-momentum particles (±2%). A lot of works need to be done for DA optimization.
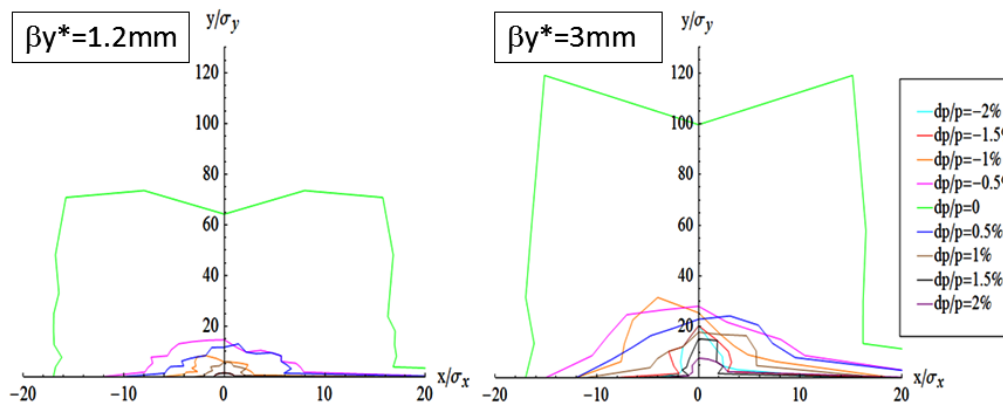
Figure 13: Dynamic aperture of CEPC [12].

2.5.3.4 *Pretzel Orbit*

CEPC is proposed as a single ring machine, so the two beams have to be properly separated at the parasitic crossing points. There are 50 bunches for each beam, thus there are 100 parasitic collision points. The two beams have to be separated at all the crossing points except for IP1 and IP3. We choose horizontal separation scheme for CEPC to avoid coupling between horizontal and vertical planes.

We use one pair of electrostatic separators to separate the beams at each arc section. One separator will be placed π/2 phase advance before the first crossing point in the arc

section, the other separator will be placed π/2 phase advance after the last crossing point in this arc section. With these 8 pairs of separators, all the crossing points in the arc section can be well separated. At IP2 and IP4, we need extra pairs of electrostatic separators to avoid beam collisions there. Two more pairs of separators will be placed π/2 phase advance before and after IP2 and IP4 to separate the beams at these two collision points. In total, ten pairs of electrostatic separators will be used in the CEPC ring to avoid all the parasitic collision points. The layout of the electrostatic separators and its orbit is shown in Figure 14. To allow for a reasonable beam lifetime, a maximum separation distance of 5σx is considered for CEPC. The resulted pretzel orbit in one arc section is shown in Fig. 15.
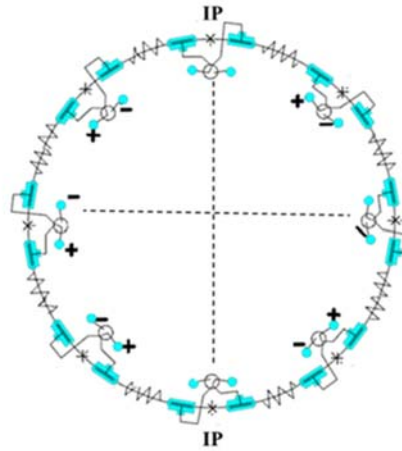
Figure 14: Pretzel scheme layout.
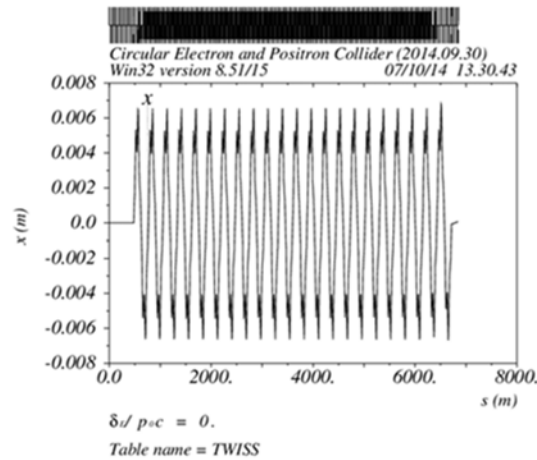
Figure 15: Pretzel orbit of electron beam in one arc section.

With pretzel scheme, the beam will not go through the center of magnets and see additional dipole and quadrupole field. To correct the distortion on dispersion and beta function, and hence restore the periodicity, we have to use 6 FODO cells to form a new period, and readjust the quadrupole strength to find the solution with the pretzel orbit. The price of correction of the lattice distortion from pretzel orbit is that, we need more families of quadrupoles which are freely tunable.

2.5.3.5 *Partial Double Ring Scheme*

Because the synchrotron radiation power is limited to 50 MW per beam in the CEPC, the number of bunches is limited to 50. In the baseline design, these 50 bunches are equally spaced, and the collisions are head-on. This design requires a pretzel orbit in order to avoid parasitic collisions in the arcs. From the experience of LEP and CESR, the pretzel orbit is difficult to operate and control, and is also difficult for injection.

In order to avoid the complicated pretzel scheme, we developed a new idea called partial double ring scheme which is shown in Figure 16. It will use a bunch train, namely, to put the 50 bunches close to each other as if it is a "macro" bunch. The two macro bunches, one each for electrons and positrons, circulating in the ring will only collide at the two interaction points (IPs) without any parasitic collision in the arcs. The length of the interaction regions will need to be made longer (~3 km each). The advantages of this alternative design compared with the single ring (pretzel) scheme are that it is more stable and more flexible, and also it has the potential for us to consider the crab waist collision scheme and further to reduce the beam power. Moreover, this scheme can help to increase the luminosity when CEPC run at the Z-pole, 45 GeV energy per beam, because Z operation will need more bunches than Higgs operation.

The studies for IR optics design and parameter choice are undergoing.
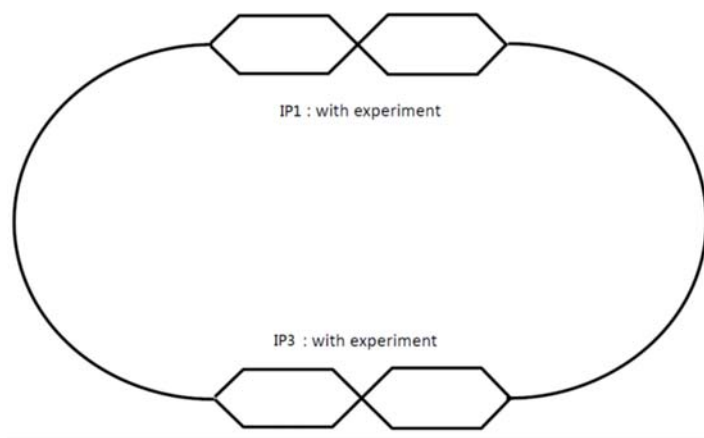
Figure 16: schematic diagram of CEPC with partial double ring.

2.5.3.6 *Detector Solenoid Compensation*

One of the key issues in high luminosity colliders is the control of coupling between horizontal and vertical planes. With the extremely small coupling (0.3%) required in the CEPC design, the coupling correction is of primary importance. The main source of betatron coupling is the detector solenoidal field. Hence an efficient local correction scheme for the coupling arising from the detector solenoid is mandatory. The distribution of the Solenoid Field Bz of CEPC detector is shown in Figure 17.

A solenoid rotates the normal transverse modes of the beam by an angle defined by the integral of the longitudinal field component along the beam orbit and inversely proportional to the beam rigidity Bρ:

$$\theta_r = \frac{1}{2B\rho} \int B_z (x) dx \qquad (3)$$

Compensation by two anti-solenoids placed on either side of the detector, with opposite magnetic field to make the total integral of *Bz* along the beam trajectory vanish, is sufficient only if no quadrupole is immersed in the field of solenoid. However, for CEPC, two final doublet quadrupoles (QD0 and QF1) are inserted into the detector and operated under the detector solenoid field of 3.5T in order to achieve the very small IP beta functions needed for high luminosity. The design for coupling correction is not easy. Our primary consideration is to wind anti-solenoid coils on QD0 and QF1 for local correction of longitudinal field, and also add additional anti-solenoid outside detector region to zero the total integral field. Still we may need to adjust the rotation and strength of nearby skew quadrupoles for residual coupling compensation.
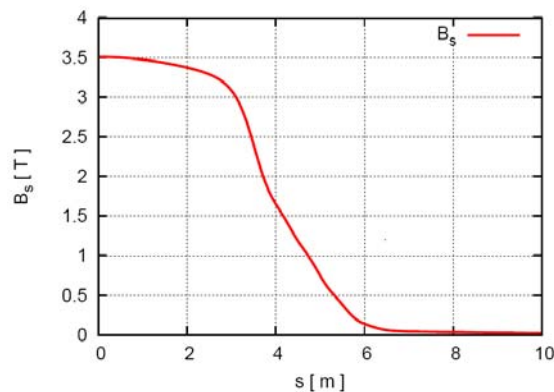
Figure 17: Distribution of the Solenoid Field Bz Along the Axis of the Detector.

2.5.4 References

1. Adrian Cho, "Higgs Boson Makes Its Debut After Decades-Long Search," Science 337 (6091): 141–143.
2. "Observation of a New Particle with a Mass of 125 GeV," http://cms.web.cern.ch/news/observation-new-particle-mass-125-GeV.
3. CMS collaboration, "Observation of a new boson at a mass of 125 GeV with the CMS experiment at the LHC," Physics Letters B, 716(1):30-61.
4. "Accelerators for a Higgs Factory: Linear vs. Circular (HF2012)," Fermi National Laboratory, 14-16 November, 2012.
5. S. Henderson. "Accelerators for a Higgs Factory," Report at HF2012, Fermilab, 14-16 November, 2012.
6. The CEPC-SPPC Study Group, CEPC-SPPC preliminary Conceptual Design Report, Volume II- Acceleraor, IHEP-CEPC-DR-2015-01, IHEP-AC-2015-01, March 2015.
7. V.I.Telnov, "Restriction on the Energy and Luminosity of e+e- Storage Ring due to Beamstrahlung", Phys.Rev.Letters 110,114801(2013).
8. D. Shatilov, "Beam-beam simulations at large amplitudes and lifetime determination", Particle Accelerators, 52, pp.65-93 (1996).
9. K. Ohmi, M. Tawada, Y. Cai, S. Kamada, K. Oide, and J. Qiang, "Luminosity limit due to the beam-beam interactions with or without crossing angle", Phys. Rev. ST Accel. Beams 7, 104401 (2004).
10. K. Ohmi, F. Zimmermann, FCC-ee/CepC Beam-beam Simulations with Beamstrahlung, Proceedings of IPAC2014, Dresden, Germany.
11. Yunhai Cai, private communication.
12. Y.W. Wang, S. Bai, H.P. Geng, T.J. Bian, X.H. Cui, D. Wang, J. Gao, Y.S. Zhu, A

preliminary design of the CEPC interaction region, TUPTY011, IPAC2015.

13. SAD. http://acc-physics.kek.jp/SAD/.

2.6 Status and Challenges of CEPC Accelerator Technical Systems

Jiyuan Zhai, Yi Sun, Zusheng Zhou, Li Shaopeng, Liu Yaping, Wen Kang,
Yingshun Zhu, Mei Yang, Changdong Deng, Haiyi Dong, Yanfeng Sui, Zhongjian Ma,
Yadong Ding, Jungang Li, Qingbin Wang, Qingjiang Zhang and Nan Li
IHEP, Beijing 100049, China
Mail to: zhaijy@ihep.ac.cn

2.6.1 Superconducting RF System

2.6.1.1 *Introduction*

The RF system accelerates the electron and positron beams, compensates for synchrotron radiation loss and provides sufficient RF voltage for energy acceptance and the required bunch length in the CEPC booster and collider ring. To deliver the target integrated luminosity, high-availability SRF components as well as rapid commissioning and efficient operation with minimal downtime are required. The SRF system is one of the most important technical systems of CEPC and is a key for achieving its design energy and luminosity.

The CEPC SRF system will be one of the largest and most powerful SRF accelerator installations in the world. Eight RF stations are placed in eight straight sections of the tunnel, and two of them split into two half stations at the interaction points IR1 and IR3. The total RF station length is approximately 1.4 km with 12 GeV of RF voltage. Table 1 shows the main parameters of the SRF system.

CEPC will use 384 five-cell 650 MHz cavities for the collider (main ring) and 256 nine-cell 1.3 GHz cavities for the Booster. The collider cavities operate in CW. The Booster cavities operate in quasi-CW mode.

During the conceptual design phase, significant effort is needed to identify high-risk challenges that require R&D. The highest priority items are: efficient and economical damping of the huge HOM power with minimum dynamic cryogenic heat load, achieving the cavity gradient with high quality factor in the vertical test and real accelerator environment, robust 300 kW high power input couplers that are design compatible with the cavity clean assembly and low heat load.

Table 1: CEPC superconducting RF system parameters.

Parameter	Unit	Main Ring	Booster (120 GeV)
Synchrotron radiation power	MW	103.42	2.46
Bunch charge	nC	60.64	3.2
Bunch length	mm	2.65	2.66
Bunch number	-	100	50
Beam current I	mA	33.2	0.87
RF frequency f_{RF}	MHz	650	1300
RF voltage V_{RF}	GV	6.87	5.12
Number of cavity	-	384	256
Cavity operating voltage V_c	MV	17.9	20
Cavity operating gradient E_{acc}	MV/m	15.5	19.3
Operating temperature	K	2	2
Q_0 at operating gradient	-	4E+10	2E+10
Q_{ext} of input coupler	-	2.2E+06	1E+07
Cavity bandwidth	Hz	295	130
RF power / cavity	kW	280	20
Number of RF power source / cavity	-	1	1
Number of cavity / module	-	4	8
Cryomodule length	m	10	12
Number of cryomodule	-	96	32
Cryomodules / RF section	-	12	4
RF section length	m	120	48
Total RF length	m	960	384

In parallel with design and key R&D, extensive development of SRF personnel, infrastructure and industrialization is essential for the successful realization of CEPC. The world's largest SRF infrastructure and talent pool should be built. Chinese industry should participate in the R&D and pre-production work as early as possible.

2.6.1.2 *High Q_0 Cavity*

The 650 MHz cavity baseline is bulk niobium operating at 2 K with Q_0=4E10 at 15.5 MV/m, and Q_0=4E10 at 20 MV/m for the acceptance vertical test. The 1.3 GHz cavity baseline is bulk niobium operating at 2 K with Q_0=2E10 at 19.3 MV/m, and Q_0=2E10 at 23 MV/m for the acceptance vertical test. New nitrogen-doping and flux expulsion technology for the high quality factor SRF cavity could be used to reach these targets. Thin film technology (such as Nb_3Sn) will be studied as an alternative. To avoid field emission, very clean cavity surface processing and string assembly is required. Electro-polishing is also needed.

2.6.1.3 *HOM and SOM Damping*

The large bunch spacing of CEPC results in very small beam spectral line spacing. Therefore it is impossible to detune the HOM modes away from the beam spectral lines with the large HOM frequency scattering from cavity to cavity caused by fabrication tolerances and RF tuning of the fundamental mode. The average power losses can be calculated as single pass excitation. As shown in Table 2, HOM power damping of 3.5 kW for each 650 MHz 5-cell cavity and 21 kW for each cryomodule is required for the CEPC main ring. Resonant excitation should be considered especially for the low frequency modes below cut-off.

Table 2: CEPC SRF cavity HOM power and heat load.

	Main Ring	Booster
HOM power / cavity	3.5 kW	5.3 W
HOM power / module	21 kW	56 W
HOM 2K heat load / module	13 W	5.9 W
HOM 5K heat load / module	39 W	3 W
HOM 80K heat load / module	390 W	43.8 W
Percent of total cryogenic load	22 %	11 %

About 80 % of the HOM power is above the cut-off frequency of the cavity beam pipe and will propagate through the cavities and finally be absorbed by the two HOM absorbers at room temperature outside the cryomodule. Each absorber has to damp about 10 kW of HOM power; thus the absorber can't be placed in the cryogenic region. Ferrite HOM absorbers developed for KEKB and SuperKEKB have achieved much higher power levels and can be used for the CEPC main ring. A LEP/LHC-type HOM coupler will be used for kW level power handling capability.

Cryogenic heat loads in different temperature regions of the main ring and Booster cryomodule are given in Table 2. HOM power dissipation in the main ring cryomodule is the main concern. Table 2 gives the preliminary upper limit estimate, which is also the design goal for the HOM heat load. The main ring cryomodule will use RF shielded bellows (copper plated) and gate valves, and flanged connections with gap-free gaskets to reduce the HOM power generation and dissipation. Assume 10 kW HOM power propagating through the beam tubes and bellows (thin copper film RRR=30, in the abnormal skin effect regime), the power dissipation is less than 2 W/m. The heat load at 5 K and in the 80 K region is dominated by HOM coupler cable heating. We will make careful calculation and engineering design to reduce the power dissipation.

The beam instability calculation gives the upper limit of the external quality factor of the HOMs with high R/Q of the main ring 650 MHz cavity, as shown in Table 3. Large HOM frequency spread from cavity to cavity (assume σ_f = 0.5 MHz and 5 MHz) will relax the Q_{ext} requirement. It is easy to reach these Q_{ext} values with the LEP/LHC HOM coupler for the modes below cut-off frequency and with the beam pipes for the modes above cut-off. Although the beam current is 1/40 of the main ring, the Booster has much weaker radiation damping especially during the low energy part of the ramp. The instability growth times are much shorter than the radiation damping time in the low energy region of the Booster. Both transverse and longitudinal feedback systems

will be needed to mitigate the multi-bunch instabilities. Another concern of the HOMs is that some modes far above cut-off frequency may become trapped among cavities in the cryomodule due to the large frequency spread.

Table 3: Damping requirements of prominent HOMs of 650 MHz 5-cell cavity.

Monopole Mode	f (GHz)	R/Q (Ω) [*]	Q_{limit} $\sigma_f = 0$ MHz	Q_{limit} $\sigma_f = 0.5$ MHz	Q_{limit} $\sigma_f = 5$ MHz
TM011	1.173	84.8	5.1E+5	2.9E7	5.8E7
TM020	1.350	5.5	6.8E+6	3.7E7	7.5E7
Dipole Mode	f (GHz)	R/Q (Ω/m) [**]	Q_{limit} $\sigma_f = 0$ MHz	Q_{limit} $\sigma_f = 0.5$ MHz	Q_{limit} $\sigma_f = 5$ MHz
TE111	0.824	832.2	2.3E+4	1.2E6	2.4E6
TM110	0.930	681.2	2.8E+4	1.5E6	3.0E6
TE112	1.225	36.2	5.2E+5	1.9E6	3.7E6
TM111	1.440	101.5	1.9E+5	1.0E7	2.0E7

[*] Longitudinal R/Q with the accelerator definition and $k_{// \text{mode}} = 2\pi f \cdot (R/Q) / 4$ [V/pC]

[**] Transverse R/Q: $k_{\perp \text{mode}} = 2\pi f \cdot (R/Q) / 4$ [V/(pC·m)]

Further design optimization of HOM properties of the main ring cavity is needed. For example, enlarge the iris diameter to decrease loss factors while keeping relatively high R/Q and low surface field of the fundamental mode, identifying trapped modes within the cavity and cryomodule, and reducing the cavity cell number or design asymmetry end cells to avoid trapped modes.

The other four pass-band modes of the operating mode of the multi-cell cavity (hereby we call them the Same Order Modes, SOMs) may also drive instabilities or extract significant RF power from the beam. SOM parameters of the Collider 650 MHz 5-cell cavity are given in Table 4, including the Q limit of the coupled bunch instability.

Since the SOMs are so close in frequency to the operating mode, they can't be damped in the same way as HOMs using HOM couplers or beam tubes. The SOMs' external Q of the HOM coupler is estimated to be around 1E10, similar with the cavity Q_0. While the input coupler can be used as the SOM coupler, the calculated external Q values are listed in the table, which are enough to damp the beam instability.

The SOM frequencies are nearly fixed and have very small spread between cavities when the operating mode is tuned to near 650 MHz during operation. The total SOM power is quite small when we consider the real cavity passband modes frequencies and the bunch time spacing of the collider. Even assuming resonant excitation (beam spectral lines coincide with all the SOM frequencies), the total SOM power is about 1 kW and with the input coupler damping, the power dissipated on the cavity wall is negligible (~ 0.1 W).

Table 4: SOMs damping of the 650 MHz 5-cell cavity by the input coupler.

Mode	f (MHz)	R/Q (Ω)	Q_{limit}	$Q_{input\ coupler}$	P_{SOM} (W)	$P_{SOM\text{-}res}$ (W)
$\pi/5$	632.322	0.02	4.5E+9	1.2E+07	1.3E-5	268.9
$2\pi/5$	637.099	0.00017	5.4E+11	3.3E+06	8.7E-7	0.6
$3\pi/5$	643.139	0.341	2.6E+8	1.7E+06	9.31E-3	638.9
$4\pi/5$	648.146	0.078	1.1E+9	1.2E+06	2.92E-4	105.8

2.6.1.4   *Power Coupler*

For CEPC, one of the key technologies is the very high power handling capability of the input power coupler for the main ring SRF cavity. Both the Q_0 and the accelerating gradient for CEPC SRF cavities are high, which requires that the coupler can be assembled with the cavity in a Class 10 cleanroom. In addition, considering the large number of couplers, heat load (both dynamic and static) is another important issue to be solved. The main challenges of the input power couplers are as follows: very high power handling capability (CW 300 kW), two windows for vacuum safety and cavity clean assembly, very small heat load, simple structure for cost saving, high yield and high reliability.

Considering the excellent performance, close frequency and IHEP experiences, BEPCII 500 MHz SCC coupler design is taken as the baseline. Several modifications are considered for the CEPC main ring SRF cavity: reduce the distance between the window and the coupling port, putting the window into the cryostat profile and thus having the window and cavity assembled in a Class 10 cleanroom, add one waveguide or cylindrical type warm window for vacuum safety, redesign the mechanical structure for higher power capacity and lower heat load.

2.6.2   **RF Power Source**

2.6.2.1   *Introduction*

Accelerators used for experiments in high-energy physics require very high power radio frequency sources to provide the energy needed to accelerate the particles. The RF power needs to be stable and predictable such that any variation in the supplied RF power has a limited and acceptable impact on the accelerated beam quality.

The RF power source delivers the energy to electrons for compensating the energy loss due to synchrotron radiation and interactions with beam chamber impedance, or ramping the electron beam to higher energy and establishes RF voltage to capture and focus the electrons into bunches. The beam and the RF station are two dynamic systems with a strong interaction, which complicates stability considerations for the composite system.

The CEPC collider beam power is about 100 MW, so the efficiency of amplifier is very important for cost of project implementation. The high power klystron is more attractive because of its potential for higher efficiency than solid state amplifier. Table 5 shows power demands comparison between klystron and solid state amplifier.

Table 5: Comparison power demands between klystron and SSA

Parameter	Unit	Klystron	SSA
Overall efficiency	%	50	40
Beam power	MW	100	100
DC input power	MW	200	250
RF overhead factor		1.3	1.3
AC input power	MW	260	325

2.6.2.2 *High Efficiency Klystron*

To get very high efficiencies, two main factors have to be considered: 1) It is necessary that all the particles, including those who experienced least modulation reach the core of the bunch. 2) The internal bunch structure has to be taken into account.

For CEPC klystron output power is not so high, the operation voltage can be a safe value. Advantage for single beam: reliable, low phase noise, some cutting-edge technologies can be used to improve efficiency, not so complicated. Approaches for high efficiency are as follows:

1) Low perveance

Perveance greatly determine the klystron efficiency.

Lower perveance→Weaker space charge effect→Stronger bunching with lower velocity spread→Higher efficiency.

But the voltage is limited so that lower perveance produce lower output power.

In CEPC klystron design, the voltage value can be accepted.

2) Using higher harmonic bunching cavities

Ideal bunching indicates that a sawtooth voltage can collect nearly all the electrons. Although the sawtooth voltage is hardly to realize in microwave band, it can be approximately obtained with harmonic superposition. Efficiency can be expressed as:

$$\eta = \frac{P_{out}}{P_0} = \frac{\dfrac{1}{2\pi}\displaystyle\int_0^{2\pi} V_{out}\cos(\omega t)I_{out}d(\omega t)}{V_0 I_0},$$

$$\omega t = \omega(t_0 + T) = \varphi_0 + \tau(\varphi), \quad \tau(\varphi) = 2\left(\sin\varphi + \frac{1}{2}\sin(2\varphi) + \dots + \frac{1}{n}\sin(n\varphi)\right)$$

3) Long drift space

When the drift length is larger than quarter reduced plasma wavelength, the space charge force will debunching the bunch ,which can produce two bunch center (like the 2nd harmonic effect).

To achieve very high efficiency, peripheral electrons should receive much stronger relative phase shift than the core electrons and this could happens only, if the core of the bunch experiences oscillations (COM) due to the space charge forces, whilst the peripherals approach the bunch center monotonously.

2.6.2.3 *Other High Efficiency RF Source*

Possible RF sources which have potentially high efficiency are IOT and Klystron. Recent report and status show the possibility to raise the RF source efficiency up to

more than 70%, and even in this efficiency, for the feedback-on operation, total efficiency goes down to around 50%.

In IOT, velocity modulation is performed in the region between the cathode and grid, and directly bunched beam is emitted across the grid and drifts to the output cavity.

Emitted current is limited in the certain phase which forms the bunch and therefore efficiency is high (~70%). Bunch current is proportional to input power, and hence proportional to output power. Therefore saturation occurs in the function of power-in and power-out.

High power level is limited around 100kW (CW), and more power level, multi-beam IOT or depressed collector approach is necessary and it is under R&D. Due to the output-cavity-only structure, gain is low as ~20dB, and for high power output aim, rather high power driver is required.

Frequency range of IOT is limited below 1.3 GHz, since the modulation is performed in the grid-cathode with the transit time effect.

Widely used in broadcast station and seems to be stable, SNS and other institutes have been considering the possible candidate as the RF source, but not succeeded yet. Thales and CPI made a team to develop this project. Therefore, we had better watch the R&D result and after the success, then offer strategy for IOT's possibility for CEPC project.

2.6.2.4 *Conclusion*

Though the klystron is a much matured electron device, there is a possibility to pursue the ambitious target of efficiency of 70-75% due to the recent progress of technology. There are three possible approaches or their combination to raise the efficiency as follows.

1) Multi-beam klystron approach
   Multi-beams of low perveance are used to increase the efficiency. Complicated design is required but there are examples in ILC project.
2) Multi-stage depressed collector klystron
   Extra useless energy is recovered in the collector, but complicated.
3) Adiabatic bunching klystron approach
   New approach, and there is possibility to use single medium perveance beam to raise the efficiency.

Since electron energy is low, space charge effect is dominant in the klystron. Sharp bunching is prevented due to the repulsive force. Space charge force is expressed by the term of perveance. Low perveance (low current, high voltage) beam has a weak space charge and then makes it possible to get high efficiency.

Dissipated power in the collector is recovered by backing to the generator, and total energy efficiency goes high. Generally the coasted beam energy spectrum is simple such as gyroklystron, this technology is effective. On the other hand, coasted beam spectrum of the klystron is complicated; this technology is not effective, especially for high power use.

In addition, the collector is divided into multistage, and brazing difficulty and radiation shield difficulty are solved. Carbon coat on the surface is needed to suppress the secondary electron emission.

2.6.3 Cryogenic System

2.6.3.1 *Introduction*

The CEPC has 640 superconducting cavities. In the Booster, there are 256 ILC type 1.3 GHz 9-cell superconducting cavities; eight of them will be packaged in one 12-m-long module. There are 32 such modules. In the collider ring, there are 384 650 MHz 5-cell cavities; four of them will be packaged into one 10-m long module. There are 96 of them.

All the cavities will be cooled in a liquid-helium bath at a temperature of 2 K to achieve a good cavity quality factor. The cooling benefits from the helium II thermophysical properties of large effective thermal conductivity and heat capacity as well as low viscosity. It is a technically safe and economically reasonable choice. The 2 K cryostat will be protected against heat radiation by means of two thermal shields cooled to temperatures from 5 K to 8 K and from 40 K to 80 K, respectively.

The cryogenic system is designed for fully automatic operation during extended periods. Reliability and stability are what concerns us most.

2.6.3.2 *Heat Load*

Table 6 summarizes the total static and dynamic heat loads of CEPC Booster and Collider cryomodules at the nominal operating conditions at different temperature levels. The total equivalent entropic capacity is 78.6 kW at 4.5 K.

Table 6: CEPC cryogenic system heat load.

	Unit	BOOSTER			COLLIDER		
		40-80K	5-8K	2K	40-80K	5-8K	2K
Module static heat load	W	140	20	3	200	40	8
Module dynamic heat load	W	140	10	30.88	200	40	62.4
HOM loss per module	W	52.8	3.2	7.2	390	39	13
Connection boxes	W	50	10	10	50	10	10
Total heat load	kW	11.45	1.22	1.47	78.2	11.9	8.48
Overall net cryogenic capacity multiplier		1.54	1.54	1.54	1.54	1.54	1.54
4.5K equiv. heat load with multiplier	kW	1.34	1.74	7.3	9.12	16.97	42.13
Total 4.5K equiv heat load with multiplier	kW	10.38			68.22		
Total heat load of booster and collider	kW	78.6					

2.6.3.3 *Refrigerator*

Eight individual refrigerators will be employed for the CEPC cryogenic system. The cryogenic plant capacities are equivalent to 12 kW at 4.5 K for each cryogenic station. The refrigerator main components include compressors, oil removal equipment, and the cold box which is vacuum insulated and houses the aluminum plate-fin heat exchangers and several stages of turbo-expanders.

The fundamental cooling process - expanding compressed helium gas to do work against low-temperature expansion engines, then recycling the lower pressure exhaust gas through a series of heat exchangers and subsequent compression - is a variant of the Carnot process that has been in use for many decades.

The key issue is to improve the plant efficiency as much as possible. There are many problems to be solved.

1. Large scale refrigerator cooling scheme optimization.
    a) 4.5K refrigerator cooling scheme optimization
    b) 2K refrigerator cooling scheme optimization
    c) Coolant configuration at wide temperature range
    d) 2K system dynamic simulation
    e) refrigerator multi-mode operation dynamic simulation
    f) control strategy optimization
2. Helium turbine technology
    a) turbine impeller optimization and mold technology
    b) turbine dynamic and static gas levitation technology
    c) Nonlinear instability mechanism of helium gas bearing
    d) Helium gas bearing stiffness and damping
    e) coordinated control of the multi-stage turbines during cooling down
3. low pressure cold compressor stability research
    a) Magnetic suspension bearing support technology
    b) Magnetic suspension bearing dynamic couple simulation
    c) Magnetic suspension bearing stability research
    d) Low pressure cold compressor surge recovery technology
4. Integration technology of the large scale refrigerator
    a) intensification heat transfer technology of multi stream low temperature heat exchanger
    b) intensification heat transfer technology of low pressure heat exchanger
    c) the auto compensation technology of low temperature pipes hot expand and cold shrink
    d) thermal-mechanical analysis of the low leakage cold box with complex pipe net.

2.6.3.4 *Flow Diagram*

A two-phase line (liquid-helium supply and vapor return) connects each helium vessel and connects to the major gas return header once per module. A small diameter warm-up/cool-down line connects the bottoms of the helium vessels. The cavities are immersed in baths of saturated superfluid helium, gravity filled from a 2 K two-phase header. Saturated superfluid helium flows along the two-phase header, which has phase separators located at one or both ends; the two-phase header is connected to the pumping return line. For the flow refer to Fig 1.
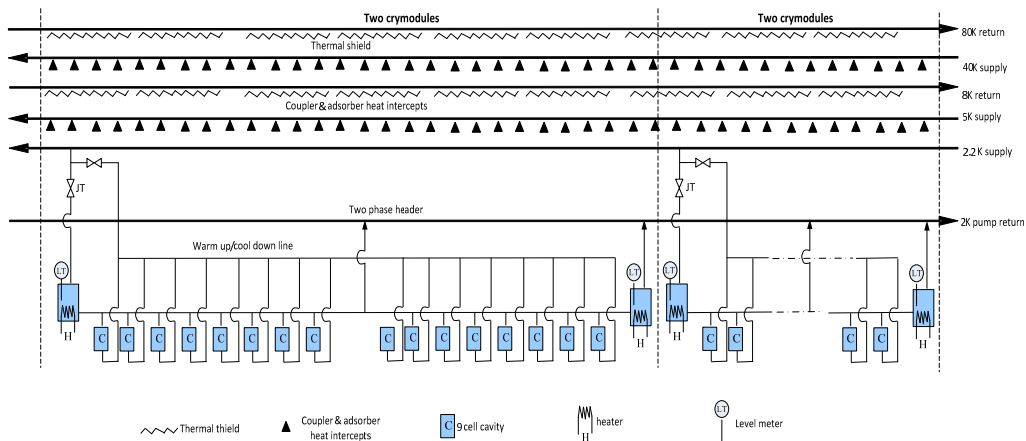
Figure 1: The flow cooling scheme of CEPC.

2.6.3.5 *Summary*

The CEPC ring is separated into 8 sections by 8 straight sections. The cryogenic systems are installed at these straight sections. Each section has one 12 kW @ 4.5 K refrigerator and relevant ancillary equipment to provide 2 K LHe for superconducting cavities. The total gas helium storage capacity of the whole CEPC cryogenic system will reach 90000 cubic meters and the install power needs more than 17.63 MW.

The design and construction of the CEPC cryogenic system is complex and not easy, especially the localization of the refrigerator needs strenuous effort from an excellent team.

2.6.4 Magnet System

2.6.4.1 *Introduction*

The CEPC accelerators include the Linac, the Booster and the Main Ring, so the accelerator magnet system includes all the magnets required for these three accelerators. Also included in the scope are the magnets for beam transport lines and injection and extraction. The circumference of the Booster and the Main Ring is similar, about 54.4 km. The Booster has 5,120 dipoles, 1,528 quadrupoles and 1,248 sextupoles. The Main Ring has 1,984 dipoles, 2,304 quadrupoles and 1,984 sextupoles. The length of the dipole magnets for the Booster and Main Ring are 8 m and 18 m respectively; this means that more than 65% of the Booster and Main Ring circumference will consist of dipole magnets. So the magnet cost becomes an important issue in the design of the magnets, especially the dipole magnets.

At present, the preliminary design of the main magnets such as dipole, quadrupole and sextupole magnets of the booster and main ring has been finished. Design for correctors and special magnets (kickers, septum, Lambertson, etc.) will be completed as the physical requirements are provided.

2.6.4.2 *Dipole Magnets*

Since the field of the dipole magnets both for the booster and the main ring is very low, as in LEP's dipole magnets, steel-concrete cores will be used to make the yokes of

the dipole magnets. There are two advantages to steel-concrete cores; one is the cost reduction since 80% of the steel is substituted by concrete if a filling factor of 0.2 is adopted. Another advantage is an increase in the working magnetic induction in the iron, thus the magnets are less sensitive to differences in iron quality and in particular to the coercive force. In addition, as the main ring is a storage ring, the magnets will work in DC mode, an alternative dipole magnet design with solid iron yoke for the main ring was also proposed, as shown in Fig. 2. To make fabrication and delivery convenient, the cores of the magnets will be split into two parts of about 4 m length for booster and four parts of about 4.5 m length for main ring. For economic reasons, the excitation bars of the magnets are made from 99.5% pure aluminum.
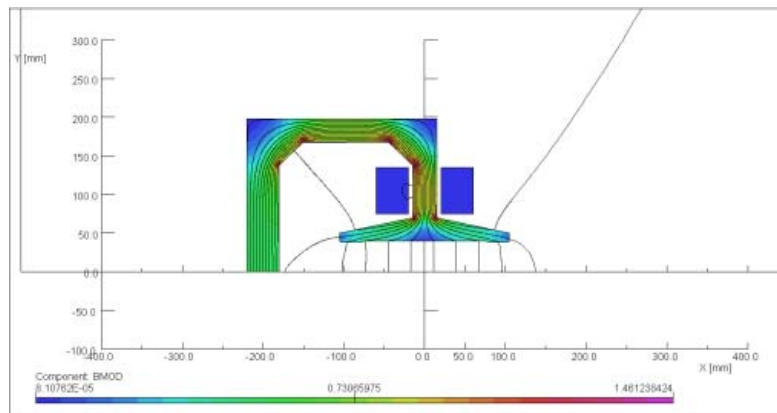
Figure. 2: Dipole magnet design with solid iron cores.

2.6.4.3 *Quadrupole and Sextupole Magnets*

The field level of the quadrupole and sextupole magnets for the booster and the main ring is neither high nor low, so the design of the magnets is similar to the magnets of BEPC. The cores of the magnets are made by low carbon silicon laminations, but for the economic reasons, the coils of the magnets will be made by aluminum conductors instead of copper conductors. In order to reduce Joule loss, the cross section of the coils is designed as large as possible. And for the coil installation, the cores of the quadrupole magnets must be divided into four parts while that of sextupole magnets divided into six parts.

2.6.4.4 *Superconducting Quadrupole Magnets*

There are two types of high gradient quadrupole magnets (QD and QF) in the CEPC Interaction Region. The magnetic field at the pole region exceeds 7T. These two magnets are inside the detector solenoid magnet which has a field of about 3.5T. So the superconducting quadrupole magnets are iron-free magnets, the magnet design is based on a typical quadrupole block coil, which are made of Rutherford Type Nb_3Sn cables, and are clamped by stainless steel collars. Two types of anti-solenoid coils are equipped within QD and QF respectively. Each pair of quadrupole and anti-solenoid coil is at the same longitudinal position (along the beam line) and in the same cryostat.

The cross section of the superconducting quadrupole coil is shown in Fig. 3 (inner quadrupole coil; outer anti-solenoid coil).
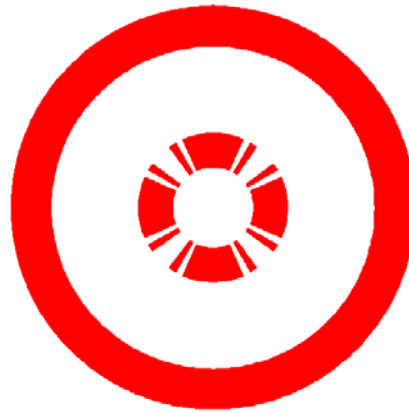
Figure 3: Cross section of quadrupole coil and anti-solenoid coil.

2.6.4.5 *R&D Program of the Magnets for CEPC*

In the R&D stage of CEPC project, three prototype magnets will be developed to study the key technical issues of the magnet design and production.

The first one is the prototype dipole magnet for the Booster, the following key technical issues will be carefully studied. 1) The magnetic and mechanical design of the dipole magnet with very low field. 2) The method of earth field shielding. 3) The eddy current effect induced by the field ramping. 4) The fabrication procedures of 4-5m long steel-concrete cores with small cross section. 5) The in situ assembly of 16m long magnets and in situ welding of hollow aluminum conductors.

The second one is the prototype quadrupole magnet for the Main Ring. 1) The magnetic and mechanical design of the quadrupole magnet with economical cross section and size. 2) Development and mass production of high quality hollow aluminum conductors. 3) The fabrication procedures of the coils wound by hollow aluminum conductors. 4) The magnetic field measurement of a long quadrupole magnet with small aperture.

The third one is the prototype superconducting quadrupole magnet for Interaction Region of the Main Ring. 1) The magnetic and mechanical design of the superconducting quadrupole magnet with very high field. 2) Development of Nb_3Sn Rutherford cable. 3) The fabrication procedures of the coils wound by Nb_3Sn Rutherford cable. 4) The design and development of the cryomodule for the very high field quadrupole magnet. 5) The assembly and the test of the magnet.

2.6.5 **Vacuum System**

2.6.5.1 *Introduction*

Beam lifetime and stability are of major importance in any storage ring. The interaction of the stored particles with the molecules of the residual gas leads to particle losses and gives rise to background in the detector. Calculating the expected pressure is an essential part of the vacuum system design. The gas load is determined by thermal desorption and also from the dynamical gas load produced by synchrotron radiation.

There are two 120 GeV circulating beams, each 16.6 mA. These beams emit intense synchrotron radiation in a forward-directed narrow cone. This energetic photon flux produces strong outgassing from the vacuum chamber and a large dynamic pressure

increase, which limits the beam lifetime and may cause increased background in the experiments. Therefore, the pumping must maintain the specified operating pressure under the condition of a large dynamic photodesorption gas load.

For CEPC, E=120 GeV, I=2×0.0166 A, ρ=6094 m, the total synchrotron radiation power P_{SR}=100 MW and a linear power density of P_L=2.62 kW/m. The total dynamic gas load of Qgas=1.93×10^{-4} Torr-L/s, and a linear SR gas load of Q_L=5.04×10^{-9} Torr-L/s/m.

2.6.5.2 *Vacuum Chamber*

The synchrotron radiation power deposited calls for a water-cooled high electrical conductivity chamber (aluminum or copper). Copper is preferred in CEPC because of its naturally lower molecular yields, lower electrical resistance, and its lower radiation, giving more efficiency in preventing photons from escaping through the vacuum chamber wall, damaging the magnets and other components. Since the chamber walls in the arc sections are subjected to very high thermal loads, copper with its excellent thermal conductivity is preferred. Vacuum chambers in the straight sections will be fabricated from stainless steel.
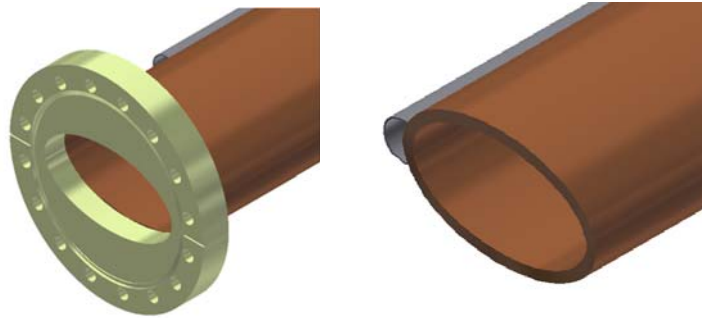
Figure 4: CEPC copper dipole vacuum chamber.

The cross-section of the CEPC dipole vacuum chamber is elliptical, 100 mm wide by 55 mm high (Figure 4). The standard length of this dipole chamber is 8 m, and the chamber wall thickness is 6 mm. The expected radiation dose outside the vacuum chamber is lower than 1×10^{-8} rad/year. A cooling channel attached to the outer wall of the beam duct carries away the heat produced by synchrotron radiation hitting the chamber wall. Finite-element analysis of a dipole chamber subjected to this power shows that the highest temperature reaches 72°C, the maximum stress is 141MPa, and the maximum deformation is 1.2×10^{-3} mm, which is in the safety range.

The copper chamber manufacturing procedure follows these steps:
- Extrusion of the beam pipe and cooling channel,
- Machining of the components to be welded,
- Chemical cleaning,
- Electron-beam welding,
- Welding of the end flanges and water connections,
- Leak checks,
- NEG coating of the inside chamber.

2.6.5.3 *Bellows Module with RF Shielding*

The primary function of the bellows module is to allow for thermal expansion of the chambers and for lateral, longitudinal and angular offsets due to tolerances and alignment, while providing a uniform chamber cross section to reduce the impedance seen by beam. Figure 5 shows the schematic drawing of the RF shielding bellows module.
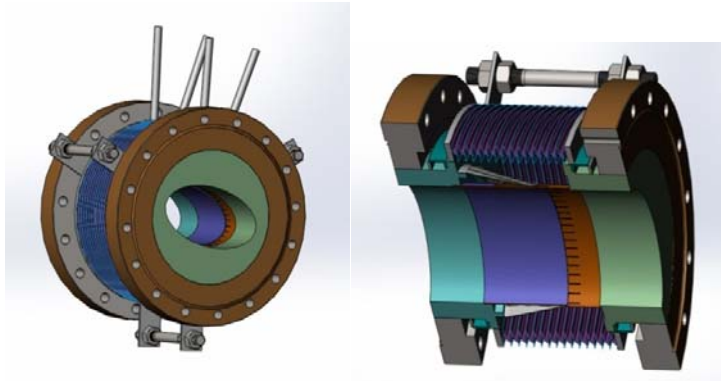
Figure 5: RF shielding bellows module.

2.6.5.4 *Pumping System*

The 54.4 km circumference of the ring will be subdivided into 260 sectors by means of all metal gate valves. These allow pumping down from atmospheric pressure, leak detecting, bakeout, and vacuum interlock protection, to be done in sections of manageable length and volume. Considering that the superconducting RF cavities may require moving out of position for servicing, two gate valves will be installed near each RF cavity to avoid other sectors exposing to atmosphere. Each sector has several roughing valves and an intake gas valve. Roughing down to approximately 10^{-7} Torr will be achieved by oil free turbo-molecular pump groups. The main pumping is achieved with Non Evaporable Getter (NEG)-coated copper chambers in the arc sections. Sputter ion pumps will be used to maintain pressure and pump off CH_4 and noble gases that can't be pumped off by the NEG pump. For the pumping system of the interaction regions where the detectors are located, depending on the space available, NEG pumps, sublimation pumps and sputter ion pumps will be used.

2.6.5.5 *Vacuum Measurement and Control*

The size of CEPC excludes the installation of vacuum gauges at short intervals. Only some special sections such as the injection regions, RF cavities and interaction regions are equipped with cold cathode gauges and residual gas analyzers. For the remainder of the ring only the current of the sputter ion pumps, placed every 20 m, will be monitored continuously and should provide adequate pressure measurements down to 10^{-9} Torr. Some mobile diagnosis equipment can be brought to places of interest during pump down, leak detection and bake-out when the machine is accessible. All metal corner valves (manually operated) will be provided every 80 m. High pressure gauges will be installed in each sector in order to protect the NEG against damage during activation.

The control of the vacuum system will be part of the general computer control systems and includes the control of the sputter ion pumps, vacuum gauges, sector valves, and the monitoring of the water cooling of the vacuum chambers. The vital interlocks (sectors valve, RF cavities, water cooling) will be hard-wired. Other controls will only be needed locally and temporarily, and therefore will be handled by mobile terminals.

Due to the high radiation levels in the tunnel, all the vacuum electronic devices will be located at the service building.

2.6.6 Instrumentation

The beam instrumentation system, consisting of various beam monitors and signal processing electronics, is one of the important parts of CEPC. This system must provide precise and sufficient information, so that accelerator physicists and machine operators can improve the injection efficiency, optimize the lattice parameters, monitor the beam behavior and increase the luminosity. Good instrumentation is also crucial for an efficient commissioning phase.

The requirements of the CEPC beam instrumentation system are different from two-ring colliders. We need to monitor beam status quickly and accurately, measure and control the bunch current efficiently, and cure beam instabilities. The beam orbit measurement is important, especially in the interaction region. It can help us know the beam position, offset and crossing angle and it is advantageous for increasing the luminosity. There are several subsystems, including BPMs for beam position, the DCCT for average beam current measurement, the tune measurement system, the photon monitoring system which includes a CCD camera for monitoring the beam profile, a streak camera for measurement of bunch length measurement and beam loss monitor.

Table 7: Main technical parameters of CEPC Beam Instrumentation Systems.

Subsystems		Parameters	Quantity
BPM	Bunch by Bunch	Measurement area (x × y): ±40 mm×±20 mm Accuracy：1 mm Resolution：0.1 mm	2324
	Closed orbit	Measurement area (x × y): ±20 mm×±10 mm Accuracy：0.1 mm Resolution：<0.001 mm Measurement time of COD：＜4 s	
BLM		Dynamic range:10^6-10^8 Counting rates: ≤10 MHz Radiation environment: <10^8 Rad Response time: ~ns	2400
Tune		Resolution：0.0001 (0.1kHz) Accuracy：0.0005 (0.5kHz)	2
DCCT		Dynamic measurement range：0.0~1.5 A Linearity：0.1 % Zero drift: <0.05 mA Remarks: shielding needed	2
BCM		Measurement range：10 mA / per bunch Relative precision：1/4095 Smallest bunch spacing：0.5 m	2
Feedback system	Transverse	Damping rate > 20 ms^{-1} Oscillation amplitude < 1 mm	2
	Longitudinal	Damping rate > 0.5 s^{-1} Energy error < 0.6%	2
Synchrotron light monitor	Beam size measurement	Resolution：10% beam size	1
	Bunch length measurement	Resolution：0.5 ps (using streak camera) Measurement time：1s	1
Vacuum chamber displacement measurement		Resolution:0.001mm	500

There are many common instrumentations to monitor the beam of CEPC, and we have experience to design part of those systems, so more R&D efforts will be done to distinguish the positron from the electron, deliver the signal from tunnel to control room and adopt the beam loss monitor (BLM) to CEPC beam.

The positrons and electrons pass through the same monitor, and we should distinguish them by polarity. The signal from BPM detector is split into 2 parts, one part is connected to discriminator and control logic to generate the strobe pulse for gating switch, another part is sent to SPDT switch input port via a "fixed delay line". After the switch, the signal is processed by different logic, as shown in Figure 6. The "discriminator and control logic" is used to check the e+ and e- pickup up signal and furthermore generate a control signal to switch the SPDT gate. There are three different discrimination techniques that we plan to use, including "amplitude and discriminator

method", "amplitude and high speed ADC method" and "system clock and trigger method".
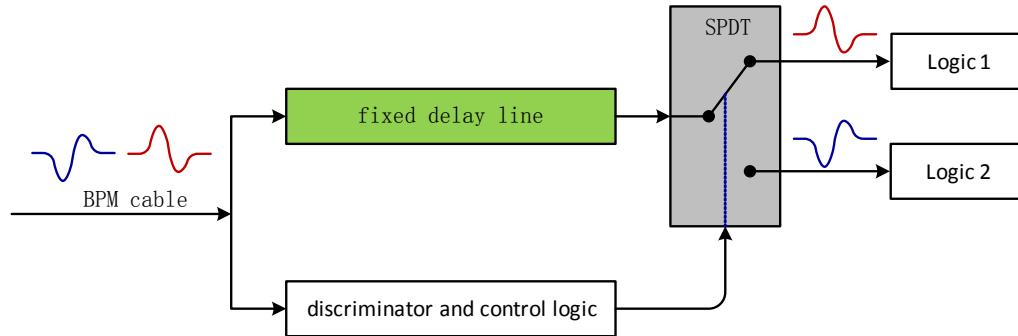
Figure 6: BPM signal working principle

The PIN-photodiode detector is selected to monitor beam loss for fast responding, non-expensive, good radiation resistance, large dynamic range, high sensitivity and small sizes. The Pin-photodiodes detector consists of two PIN-photodiodes mounted face-to-face. In the CEPC where beam energy is 120 GeV, the synchrotron radiation photon undergoes mainly a photoelectric effect or a Compton effect; the emitted electron may reach the second diodes, resulting in coincident signals. A thin copper (or lead) layer between the two diodes can reduce the probability for the emitted electron to reach the second diode. In this way the background counts due to synchrotron radiation can be reduced. Also to reduce these coincidence rate, additional lead shield will be needed around the BLMs. The optimum thickness of the layer and lead shield should be calculated and tested.

There are unique problems specific to the large size of the ring. Considering the long distances, it is not a good choice to use copper cables to send signals; we should digitize the analogy signals in the tunnel and use optical fibres to send data from electronics near the monitors to the local stations in an auxiliary tunnel.

2.6.7 Radiation Protection

The radiation shielding is important for CEPC, not only for the synchrotron radiation power is up to more than 1 kW/m, and the beam energy is 120 GeV, which can cause nuclear cascade and produce kinds of secondary particles, but also for its big scale and influence to the public, whose circumference is larger than 50 km. During the process of shielding design, rigorous dose limit should be adopted and the ALARA principle should be applied; meanwhile, a state-of-the-art radiation monitoring and alarm system as well as a rigorous access control system to protect personnel should be well designed.

The major issues for the shielding design are source term estimation, bulk shielding, duct streaming, synchrotron radiation (SR) and activation. The beam energy is 120 GeV, except the gamma and the neutron should be shielded outside the shielding walls; muon and other rare secondary particles should also be considered. Synchrotron radiation is a kind of electromagnetic radiation emitted by charged particles when they move at close to the speed of light in a magnetic field. For CEPC, the SR emitted power per unit length is huge, up to 1 kW/m. Hence, SR will cause very high radiation dose rates in many accelerator components and also in the air in the tunnel. This will cause heating of the vacuum chamber, radiation damage to machine elements, formation of

ozone and nitrogen oxides in the air, and further lead to corrosion of machine components. At present, two vacuum chambers are proposed: (1) aluminum covered by lead shielding and (2) fabricated entirely of copper. In order to have a detailed and accurate shielding design, the methodology, benchmarking and data evaluation related to these issues should be verified.

Radiation dose monitoring program will provide continuous measurements of the ambient dose equivalent and the ambient dose rate equivalent in the underground areas together with the surface building areas. This system will permanently monitor the level of radioactivity in water and air released from the facility installations. The radiation monitoring system provides remote supervision, long term database storage and off-line data analysis. A typical frame diagram is given in Figure 7. The key issue for this system is research on different data communication paths according to the monitoring conditions.
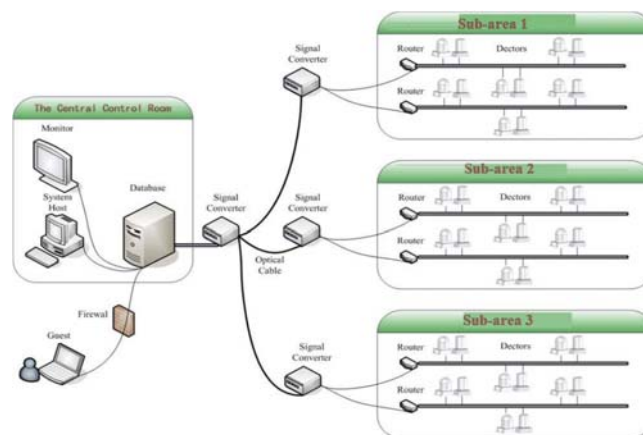
Figure 7: Frame diagram of the radiation monitoring system.

The personnel safety interlock system consists of a Programmable Logic Controller (PLC) system and Access Control System (ACS), PLC monitor interlocking equipment, and ACS administrative interlocking information. During the system design, the design criteria such as fail safe, redundancy, multilayer protection, and people oriented should be considered in mind. Figure 8 shows the layout of the PSIS. But for such large equipment, the optimized logical relationship, proper zone division, rigorous operation specification and the safety education should be deeply invested and researched.

Figure 8: Layout of the PSIS.

2.7   Outline and Status of the FCC-ee Design Study

Michael Benedikt, Frank Zimmermann
CERN, Route de Meyrin, 1211 Geneva 23, Switzerland
Mail to: michael.benedikt@cern.ch , frank.zimmermann@cern.ch

2.7.1   Motivation and Scope

The Update of the European Strategy for Particle Physics in 2013 [1] declared as its second highest priority that "…to propose an ambitious post-LHC accelerator project….., CERN should undertake design studies for accelerator projects in a global context,…with emphasis on proton-proton and electron-positron high-energy frontier machines…". In response to this request, the global Future Circular Collider (FCC) study is designing a 100-TeV proton collider (FCC-hh) in a new ~100 km tunnel near Geneva, a high-luminosity electron-positron collider (FCC-ee) as a potential intermediate step, and a lepton-hadron option (FCC-he). The FCC study comprises accelerators, technology, infrastructure, detector, physics, concepts for worldwide data services, international governance models, and implementation scenarios. The FCC study is mandated to deliver a Conceptual Design Report and preliminary cost estimate by the time of the next European Strategy Update expected for 2019.

As of July 2015, 58 institutes from 22 countries have formally joined the FCC collaboration, which is based on a common Memorandum of Understanding (MoU) and on institute-specific addenda. All FCC member institutes are represented in the FCC Collaboration Board.

In the frame of its HORIZON 2020 programme, the European Commission is funding the design of core parts of the FCC hadron collider through the "EuroCirCol" project. EuroCirCol comprises of 14 beneficiary institutes from the EU, Switzerland and Japan, plus several US laboratories as associates.

After a successful kick-off meeting at the University of Geneva, Switzerland, in February 2014 [2], the first annual meeting at Washington DC in March 2015 [3] reviewed the progress of all FCC activities one year after the study launch.

2.7.1 Physics Requirements

The FCC-ee should achieve highest possible luminosities over a wide range of beam energies, from 35 GeV to ≈200 GeV, supporting extremely high precision tests of the standard model as well as unique searches for rare decays.

The FCC-ee physics programme [4] includes: (1) α_{QED} studies (with energies as low as 35 GeV) to measure the running coupling constant close to the Z pole; (2) operation on the Z pole (45.5 GeV), where FCC-ee would serve as a 'TeraZ' factory for high precision M_Z & Γ_Z measurements and allow searches for extremely rare decays (enabling the hunt for sterile right-handed neutrinos); (3) running at the H pole (63 GeV) for H production in the s channel, with mono-chromatization, e.g. to map the width of the Higgs; (4) operation at the W pair production threshold (~80 GeV) for high precision M_W measurements; (5) operation in ZH production mode (maximum rate of H's) at 120 GeV; (6) operation at and above the $t\bar{t}$ threshold (~175 GeV); and (7) operation at energies above 175 GeV per beam should a physics case for the latter be made.

Scaling from LEP and LEP2 some beam polarization is expected for beam energies up to ≥80 GeV [5], which will be exploited for precise energy calibration using resonant depolarization.

The collider may be optimized for operation at 120 GeV (Higgs factory), and at 45.5 GeV (TeraZ factory) as second priority.

2.7.2 Layout and Parameters

The FCC-ee layout must be compatible with the tunnel infrastructure for the hadron collider FCC-hh. Some of its key elements are: (a) a double ring with separate beam pipes, magnet-strength tapering (to compensate for the energy sawtooth due to synchrotron radiation), and independent optics control for the counter-circulating electron and positron beams, colliding at a total crossing angle of 30 mrad; (b) top-up injection based on a fast-cycling booster synchrotron housed in the same large tunnel with bypasses around the particle-physics detectors; and (c) local chromatic correction of the final-focus systems.

The range of FCC-ee beam parameters is indicated in Table 1, for simplicity showing numbers for (only) three different operation modes. The beam current varies greatly with beam energy, ranging from a few mA, as at LEP2, to 1.5 A, similar to the B factories. As a design choice, the total synchrotron radiation power has been limited to 100 MW, about 4 times the synchrotron-radiation power of LEP2. For a roughly four times larger machine this results in comparable radiation power per unit length. The present numbers might translate into a total wall plug power around 300 MW. The estimated luminosity numbers scale linearly with the synchrotron-radiation power. Other important choices to be made, or to be confirmed, are the number of collisions points (2 or 4), the crossing angle (30 mrad in total), and the collision scheme (crab waist?).

Table 1: Key parameters for FCC-ee, at three beam energies, compared with LEP2. The parameter ranges indicated reflect a sensitivity to the number of IPs and to the choice of collision scheme ("baseline" [6] with varying arc cell length and small crossing angle, or a crab-waist scheme based on a larger crossing angle and constant cell length [7]).

| Parameter	FCC-ee			LEP2
energy/beam [GeV]	45	120	175	105
bunches/beam	13000- 60000	500- 1400	51- 98	4
beam current [mA]	1450	30	6.6	3
luminosity/IP x 10^{34}cm^{-2}s^{-1}	21 - 280	5 - 11	1.5 - 2.6	0.0012
vertical IP β* [mm]	1	1	1	50
geom. hor. emittance [nm]	0.1-30	1	2	22
energy loss/turn [GeV]	0.03	1.67	7.55	3.34
synchrotron power [MW]	100			22
RF voltage [GV]	0.2-2.5	3.6-5.5	11	3.5

Presently there is a trend to transit from the original baseline [6], in which the arc cell length is varied so as to maintain almost constant geometrical emittance at all beam energies, to the crab-waist scheme, for which the smallest possible transverse emittances are desired at all energies. On the *Z* pole, the crab-waist approach could achieve about ten times more luminosity than the baseline [7] whereas at the high energy operation points the performance of the two optics variants is about equal. Figure 1 displays the expected luminosity per IP as a function of c.m. energy, assuming crab-waist collisions at two points.
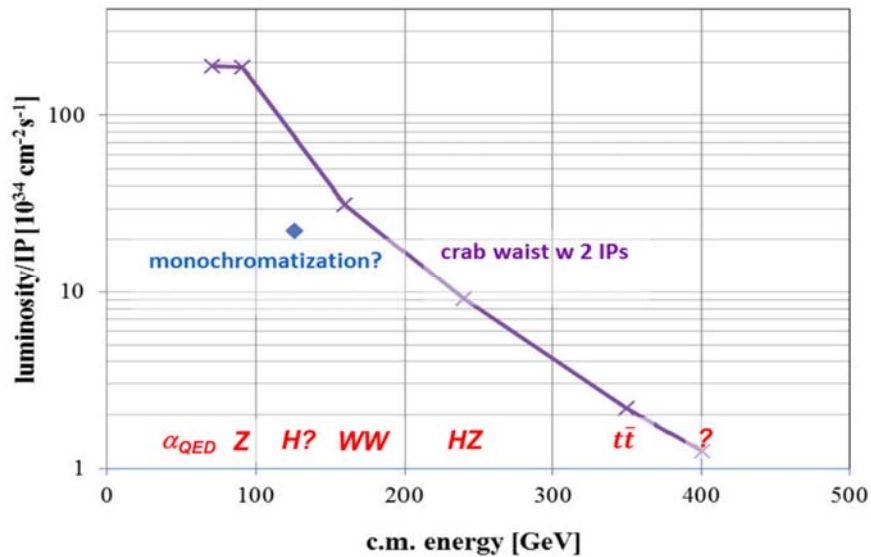
Figure 1: Projected FCC-ee luminosity per interaction point (IP) as a function of centre-of-mass energy, for a scenario with crab-waist collisions at two IPs.

2.7.3 Site Study

A tunnel optimization tool was developed in collaboration with a UK company [8]. All available information, in particular geology, from French and Swiss sources was fed into this device. A snapshot of the tool's web interface is shown in Fig. 2. Preliminary conclusions are that a tunnel of 90 – 100 km circumference fits the geological situation of the Geneva basin well, better than a tunnel of ≤80 km circumference, and that the LHC, and in particular its location, could be suitable as potential injector for the hadron collider.
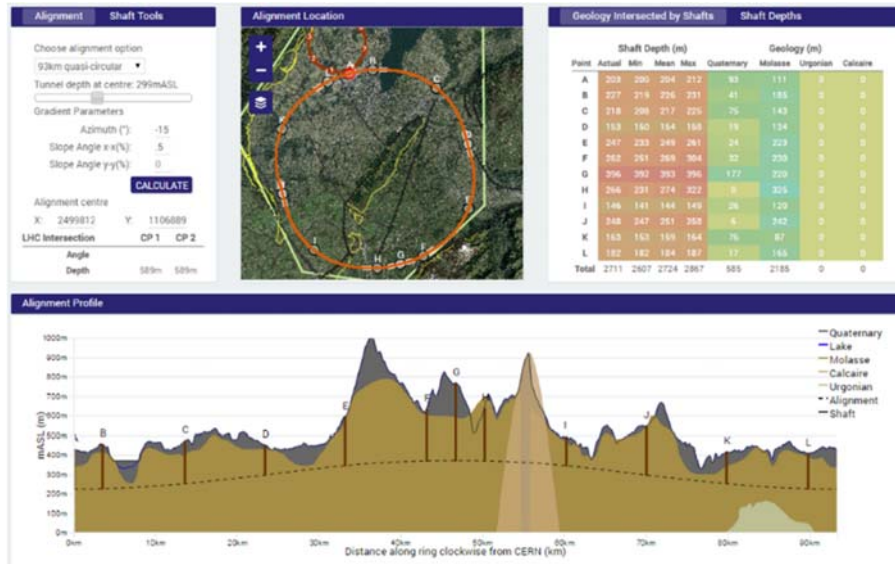
Figure 2: Web interface of the FCC tunnel optimization tool. The example is for a ring of 93 km circumference, largely located in the favorable "molasse" layer.

2.7.4 SC RF System

The superconducting RF system is the key technology of the FCC-ee [9]. The RF system requirements are characterized by two regimes – (1) high gradients for H and $t\bar{t}$ up to ≈11 GV when operating with a few tens of bunches, and (2) high beam loading with currents of about 1.5 A at the Z pole. The project aims at SC RF cavities with gradients of ≈20 MV/m, but lower gradients (e.g. 10-15 MV/m) are also acceptable. An RF frequency of 400 MHz has been chosen, equal to the one of the FCC-hh hadron collider.

The conversion efficiency from wall plug to RF power is an important figure for the overall power consumption of the facility. The FCC R&D target is 75% or higher. An efficiency of 65% was achieved for LEP2. Recent innovations in klystron design may allow for much higher values still [10].

Possible staging scenarios for the RF system, for the beam parameters, and for the optics have been developed [11, 12]. In particular, it is planned to share the RF systems for $t\bar{t}$ running, either by transverse displacements of the RF cavities or by means of electrostatic separators, in order to achieve the voltage required for $t\bar{t}$ running without installing more RF cavities than those required for *ZH* operation.

2.7.5 SuperKEKB Test Bed

SuperKEKB [13] will be an important demonstrator for a number of key concepts of the *FCC-ee* design. Simply speaking, all elements not yet tested at LEP2, KEKB or PEP-II will be demonstrated by SuperKEK.

In various regards SuperKEKB actually goes beyond FCC-ee. For example, SuperKEKB will implement top-up injection at higher current with a shorter beam lifetime. The β_y^* of SuperKEKB will be 300 μm, to be compared with 1 or 2 mm at FCC-ee (see Fig. 3). The design beam lifetime is 5 minutes, limited by Touschek scattering, while the *FCC-ee* beam lifetime is more than 20 minutes, due to radiative Bhabha scattering (and to some extent beamstrahlung). SuperKEKB aims at a vertical-to -horizontal emittance ratio of 0.25% with colliding beams, similar to FCC-ee. The off-momentum design acceptance of SuperKEKB is ±1.5%. Such a value would also be sufficient for FCC-ee operation at the $t\bar{t}$ threshold, where beamstrahlung may have a noticeable effect on the beam lifetime [14]. The SuperKEKB-injector e$^+$ production rate of 2.5×10^{12}/s is even higher than required for *FCC-ee* crab-waist running on the *Z* pole ($<1.5 \times 10^{12}$/s). The SuperKEKB beam commissioning will start in early 2016.
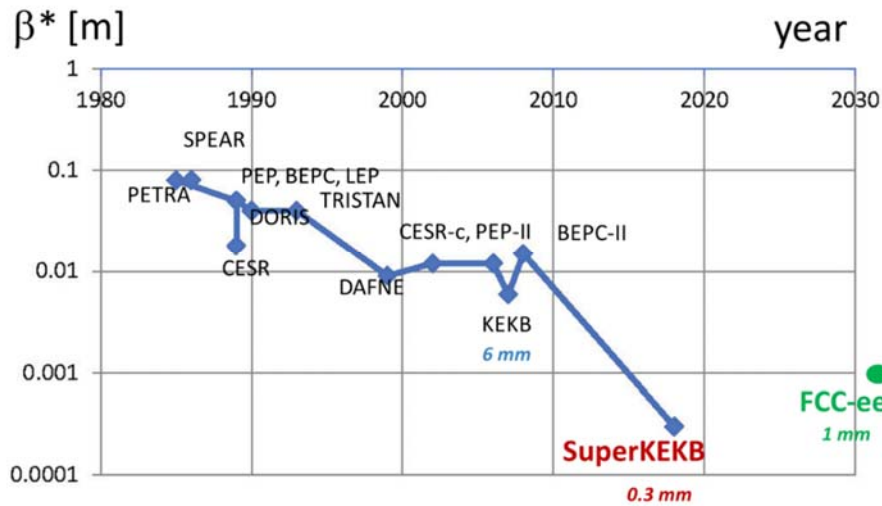
Figure 3: β_y^* evolution in circular e^+e^- colliders over 50 years, including the upcoming SuperKEKB and FCC-ee.

2.7.6 Outlook

Figure 4 illustrates that the preparation of the FCC as next circular collider is timely. Figure 5 shows the study time line towards the FCC Conceptual Design Report. FCC-ee beam-dynamics challenges and ongoing studies are discussed in a companion paper [15].

The FCC collaboration is looking forward to design convergence at its 2016 annual meeting, which will be held in Rome, Italy, from 11 to 15 April 2016 [16].
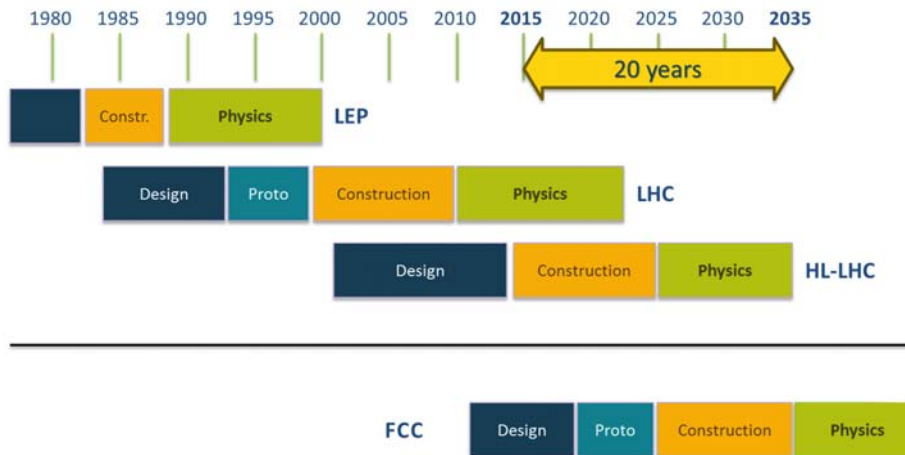
Figure 4: Time line of CERN Circular Colliders and the FCC.

Figure 5: Study time line towards the FCC Conceptual Design Report.

2.7.7 Acknowledgements

2.7.8 References

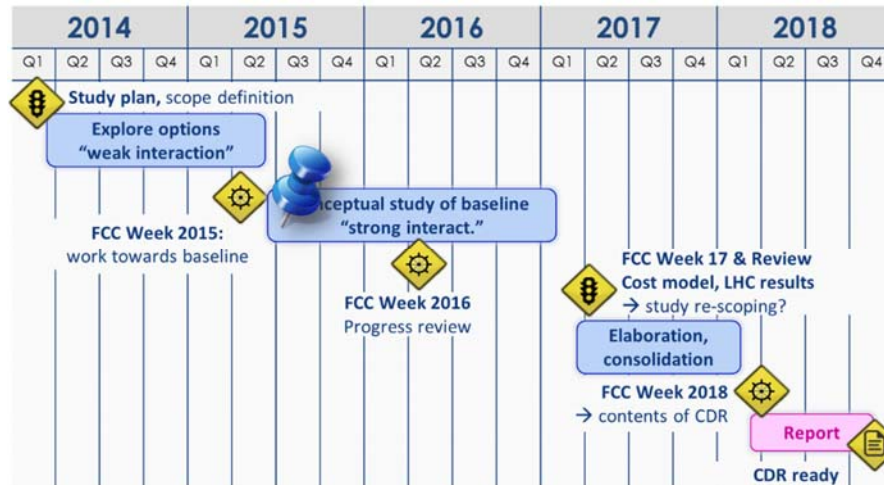1. Sixteenth European Strategy Session of Council, Brussels, 30 May 2013, CERN-Council-S/107/Rev. (2013)
2. Future Circular Collider Study Kickoff Meeting, University of Geneva, 12-15 February 2014, http://indico.cern.ch/event/282344/
3. A. Blondel, P.Janot, et al., e.g. Ref. [3]
4. U. Wienands, "Is polarization possible at TLEP?," 4th TLEP workshop, CERN, 4-5 April 2013, http://indico.cern.ch/event/240814/timetable/#20130405
5. J. Wenninger et al., "Future Circular Collider Study – Lepton Collider Parameters," FCC-ACC-SPC-0003 rev. 2.0 (2014).
6. A. Bogomyagkov, E. Levichev, and D. Shatilov, "Beam-Beam Effects Investigation and Parameter Optimization for Circular e^+e^- Collider TLEP to study the Higgs Boson," Phys. Rev. ST Accel. Beams 17, 041004 (2014).
7. J.A. Osborne, C. Cook, "Future Circular Collider (FCC) Civil Engineering Feasibility Study," Review of FCC Tunnel Footprint and Implementation (Chair P. Lebrun), CERN, 11 June 2015
8. A. Butterworth,"The RF System for FCC-ee," EPS-HEP 2015, Vienna, July 2015
9. I. Syratchev, "High Efficiency Klystron Development," High Gradient workshop, Beijing, June 2015
10. U. Wienands, "Staging Scenarios for FCC-ee," at Aspen Winter Conference "Exploring the Physics Frontier with Circular Colliders," 31 January 2015.
11. M. Benedikt et al., "Combined Operation and Staging for the FCC-ee Lepton Collider," Proc. IPAC'15 Richmond (2015)
12. 2016 FCC Annual Meeting, Rome, 11-15 April 2016
13. Articles on SuperKEKB in this ICFA Newsletter.
14. V. Telnov, "Restriction on the energy and Luminosity of e^+e^- Storage Rings due to Beamstrahlung," Phys.Rev.Lett 110, 114801 (2013).

15. M. Benedikt et al., "Beam Dynamics Challenges for FCC-ee," in this ICFA Newsletter
16. Updated information will be posted at http://cern.ch/fcc.

2.8 Beam Dynamics Challenges for FCC-ee

Michael Benedikt, Katsunobu Oide* and Frank Zimmermann
CERN, Route de Meyrin, 1211 Geneva 23, Switzerland
* also KEK, Tsukuba, Japan
Mail to: michael.benedikt@cern.ch , katsunobu.oide@cern.ch ,
frank.zimmermann@cern.ch

Anton Bogomyagkov and Eugene Levichev
BINP, Novosibirsk, Russia
Mail to: a.v.bogomyagkov@inp.nsk.su , e.b.levichev@inp.nsk.su

Mauro Migliorati
Sapienza University, Roma, Italy
Mail to: mauro.migliorati@uniroma1.it

Uli Wienands
SLAC National Accelerator Laboratory, Menlo Park, U.S.A.
Mail to: uli@slac.stanford.edu

2.8.1 Introduction

The goals of FCC-ee include reaching luminosities of up to a few 10^{36} cm^{-2}s^{-1} per interaction point at the *Z* pole or some 10^{34} cm^{-2}s^{-1} at the *ZH* production peak, and pushing the beam energy up to $\geq$175 GeV, in a ring of 100 km circumference, with a total synchrotron-radiation power not exceeding 100 MW. A parameter baseline as well as high-luminosity crab-waist options were described in [1] and [2], respectively. The extremely high luminosity and resulting short beam lifetime (due to radiative Bhabha scattering) are sustained by top-up injection. The FCC-ee design status and typical beam parameters for different modes of operation are reported in [3].

One distinct feature of the FCC-ee design is its conception as a double ring, with separate beam pipes for the two counter-rotating (electron and positron) beams, resembling, in this aspect, the high-luminosity B factories PEP-II, KEKB and SuperKEKB as well as the LHC. The two separate rings do not only permit operation with a large number of bunches, up to a few 10,000's at the *Z* pole, but also allow for a well-centered orbit all around the ring as well as for a nearly perfect mitigation of the energy sawtooth, e.g. by tapering the strength of all magnets according to the local beam energy, and for an independent optics control for the two beams. A side benefit at low energies is a reduction of the machine impedance by a factor of twos.

A long list of optics and beam dynamics challenges for FCC-ee includes the following: (1) final focus optics design with a target vertical IP beta function of 1 or 2 mm, 50 or 25 times smaller than for LEP2, incorporating sextupoles for crab-waist; (2) synchrotron radiation in the final focus systems and the arcs, with effects on the detector (background, component lifetime) and on the beam (vertical emittance blow up and dynamic aperture); (3) beam-beam effects, including single-turn and multi-turn

beamstrahlung; (4) design of the interaction region with a strong detector solenoid with possible compensation solenoids, a large crossing angle and a pair of final-focusing quadrupoles; (5) compatibility of the layout with the design of the hadron collider sharing the same tunnel; (6) RF acceleration system for high voltage (ZH, tt) and high current (Z, WW) with possible staging scenario; (7) impedance, HOM losses and instabilities, especially for high-current "low-energy" operation at the Z pole; (8) the top-up injection scheme; (9) achieving the dynamic aperture required for adequate beam lifetime and for the top-up injection, comprising the optimization of the arc optics; (10) vertical emittance control, including alignment and field errors, lattice nonlinearities, as well as beam-beam effects; (11) energy calibration and transverse polarization; (12) adapting to a non-planar tunnel; and (13) the development of a mono-chromatization for direct H production in the s channel. In the following we consider some of these challenges.

2.8.2 Collider Layout

Figure 1 presents one possible FCC-ee collider layout, with two collision points. The latter are located at diametrically opposed positions of the ring. The incoming beam line is less bent than the outgoing beam line in order to minimize the synchrotron radiation emitted in the direction of the experimental detector. This leads to a rather large separation of the inner and outer beam lines on each side of each interaction point (IP), most likely necessitating two separate tunnels over a distance of 5-6 km around each IP. The outer tunnel might accommodate the detector-bypass for the booster ring, as sketched in the figure, and it might later host the hadron collider. The outer and inner beam lines cross in the long straight sections half way between the two experiments. This provides a perfect two-fold symmetry of the FCC-ee collider ring, with a correspondingly decreased number of systematic resonances.
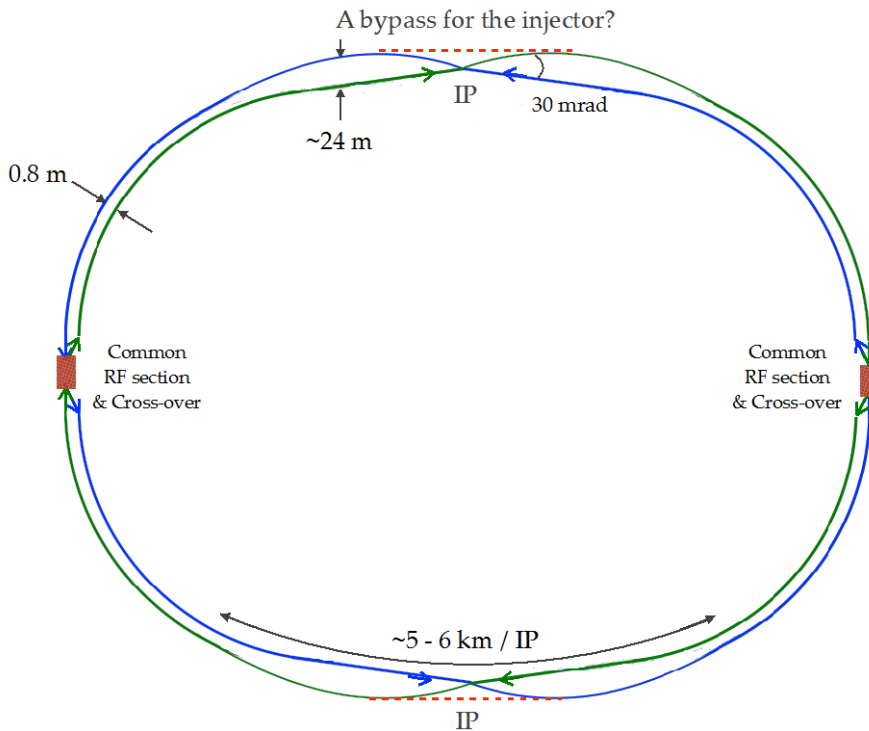

Figure 1: One possible FCC-ee layout (K. Oide).

2.8.3 Staging

Staging scenarios are being considered, in which the RF system is varied in steps, starting at low energy, e.g. *Z* pole operation (45.5 GeV/ beam), with fewer cavities (and correspondingly lower impedance), installing the full 400-MHz RF system for *ZH* running (120 GeV/beam), and later, for $t\bar{t}$ operation (175 GeV per beam) sharing the RF cavities for both beams, as indicated in Fig. 1, or adding higher harmonic 800 MHz cavities [4,5]. Complementary staging possibilities exist for the arc optics (varying cell length, or emittance) and for the vertical IP beta function, β_y^*.

2.8.4 Final-Focus Optics

Various final-focus optics for FCC-ee have been developed and evaluated [6,7]. A recent design is illustrated in Fig. 2, which shows the incoming half of one possible final focus optics, corresponding to the layout of Fig. 1 at a total crossing angle of 30 mrad. As indicated at the bottom, the critical photon energies for this design are below 100 keV over the last 900 m before the IP, and less than 1 kW of synchrotron radiation power is emitted here, so that all design requirements inferred from LEP experience [8,9] appear to be met. The crab waist collision scheme can be realized by a dedicated crab-waist sextupole [7] or by a "virtual" crab-waist sextupole as in Fig. 2 (based on the odd-dispersion scheme for chromaticity correction [10], where only one of two vertical chromatic correction sextupoles is located at a place with nonzero dispersion).
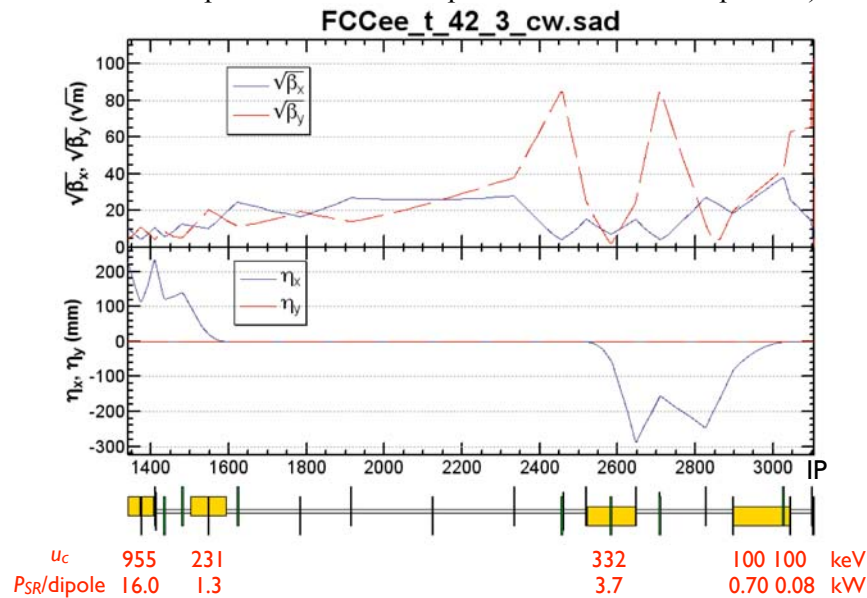

Figure 2: Incoming FCC-ee IR optics with low synchrotron radiation (K. Oide).

2.8.5 Interaction Region

The part of the interaction region closest to the IP is particularly challenging, due to the combination of a small β_y^* of 1-2 mm and a large crossing angle of 30 mrad, which

enhances the effect of fringe fields, kinematic nonlinearities, and synchrotron radiation. Additional complications arise from the detector solenoid field, and the need for shielding solenoids (around the final quadrupoles) as well as for an anti-solenoid (to compensate the solenoid-induced betatron coupling), together with synchrotron radiation emitted in these elements, and especially in their fringe fields [7]. Figure 3 shows one proposed configuration.
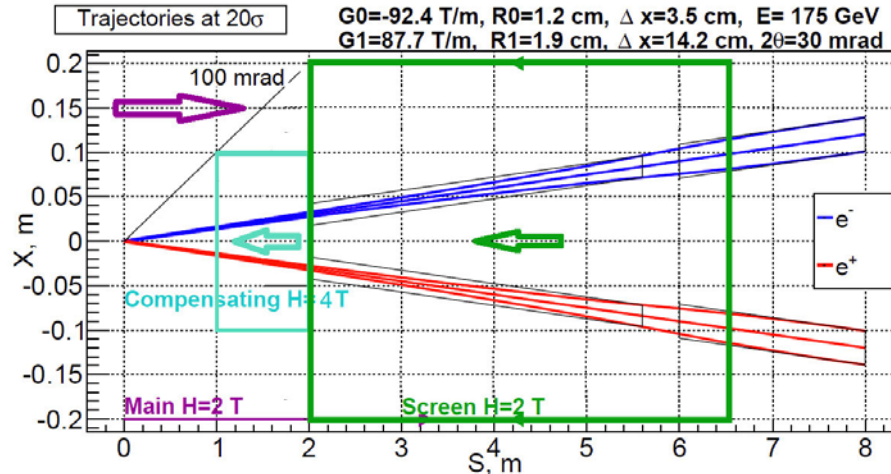
Figure 3: Example IR layout including main, compensating and screening solenoids (A. Bogomyagkov, S. Sinyatkin).

2.8.6 Machine Detector Interface and IR Synchrotron Radiation

Tools based on GEANT have been developed to model the machine detector interface and beam-related detector background in FCC-ee [8,9]. LEP Experiences call for critical photon energies below 100 keV and total power levels below 1 kW emitted in the direction of the particle-physics detector.

2.8.7 Dynamic Aperture

Off-momentum dynamic aperture is an important design constraint. A large acceptance improves the beam lifetime at the top threshold where beamstrahlung is important [11], and also provides space for off-momentum (top-up) injection.

The minimum required momentum acceptance, in view of beamstrahlung, is ±1.5% at 175 GeV and ±1.0% at 120 GeV, for the presently assumed beam parameters in case of crab-waist collisions.

Over the past years, the off- and on-momentum dynamic aperture of several alternative collider optics have been steadily improved, e.g. by optimizing the arc-cell phase advance and by adjusting the strengths of the arc sextupoles.

Synchrotron-radiation damping must be taken into account when simulating the dynamic aperture. Figure 4 shows an example result.

The dynamic aperture and the dynamic energy acceptance are almost acceptable in the latest optics designs. The radiation damping plays an important role for the dynamic aperture. The quadrupole fringe fields and kinematic terms can be compensated by two

IR octupoles. The dynamic aperture is limited by the combined effect of IR sextupoles and arc sextupoles.

A potential issue is the energy sawtooth due to synchrotron radiation, varying from a negligible value to about 2% per half-turn from the Z energy to the $t\bar{t}$ beam energy. In the two-ring scenario based on separated magnetic systems, this effect can be mitigated by varying the magnet strengths according to the local beam energy. Detailed studies of possible powering schemes are required to ensure that the momentum aperture remains sufficiently large. If during $t\bar{t}$ running the RF sections are combined for both beams, the two optics in the common regions can be matched simultaneously, as is routinely done for energy-recovery linacs.

Synchrotron radiation in the quadrupole magnets is another important effect for FCC-ee as it already was for LEP2 [12]. Indeed, this effect sets a minimum length for the arc quadrupoles. For large-amplitude particles it also leads to a breakdown of the geometric and chromo-geometric cancellations between paired sextupoles.
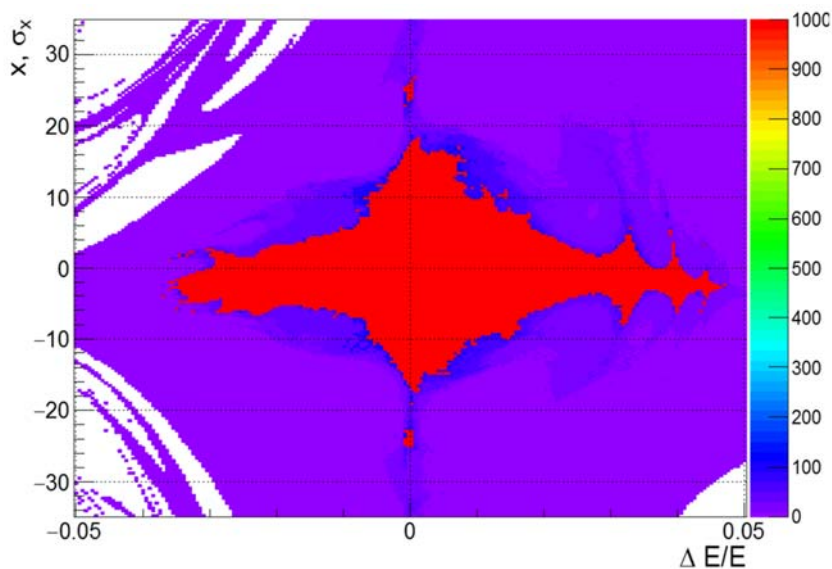
Figure 4: Simulated horizontal dynamic aperture as a function of initial relative momentum offset, ranging from -5% to +5%, for one FCC-ee candidate optics at 175 GeV beam energy, obtained by tracking over 1000 turns, including synchrotron motion, radiation damping, and crab-waist sextupoles. The color code indicates the number of turns survived (P. Piminov, A. Bogomyagkov).

2.8.8 Beam-Beam Effects

The crab-waist collision scheme is predicted to increase the maximum value of the vertical beam-beam tune shift at which the vertical beam size starts to blow up by about a factor of two, as compared with a standard (head-on) collision scheme.

A novel phenomenon for circular colliders is beamstrahlung, which at high energies affects the beam lifetime [11], and at low beam energies increases the bunch length and the energy spread [13,14]. Both effects are taken into account in the FCC-ee design optimization.

According to LEP experience and confirmed by some simulations, the beam-beam limit for classical head-on collisions increases with beam energy or damping decrement

[15]. For FCC-ee crab-waist collisions, reducing the number of IPs from 4 to 2 may increase the maximum tune shift per IP only by a moderate 5-10% and the corresponding luminosity per IP by a similar factor [16].

2.8.9 Top-Up Injection

Top-up injection is an integral part of any high-luminosity circular collider [17]. Longitudinal injection can profit from faster damping and may have less impact on the particle-physics detector (since the design dispersion at the collision point is zero). Longitudinal injection has successfully been used at LEP [18,19]. Initial design considerations for the FCC-ee longitudinal injection include multipole kicker injection and septum-less injection schemes [20]. An alternative vertical injection scheme could potentially take advantage of the extremely small vertical emittance.

2.8.10 Mono-Chromatization

An interesting options presently under study is the possibility of direct Higgs production in the s channel, at a beam energy of 63 GeV. In order to obtain an acceptable Higgs event rate and to precisely measure the width of this particle mono-chromatization will be required. The mono-chromatization can be realized, e.g., by introducing horizontal IP dispersion of opposite sign for the two colliding beams [21,22]. The mono-chromatization factor should be larger than 10.

2.8.11 Impedance and Instabilities

Impedance effects are a concern, in particular for the high-current operation at the Z pole. The energy loss at the RF cavities can be as large as the energy loss due to synchrotron radiation [23]. Fortunately, most of the power will be dissipated in the tapers outside the low-temperature cavity cells. Higher-order mode (HOM) heating of the cavities is a related concern, calling for efficient HOM dampers operating at room temperature. As this has the potential to limit the beam current—thus the maximum luminosity achievable at the Z pole—we will continue to investigate means to reduce the loss factor.

In addition the heavy-beam loading and residual HOM-driven instabilities require strong longitudinal feedback loops, perhaps similar to those for PEP-II, while a transverse bunch-by-bunch feedback must suppress resistive-wall, HOM-driven, and ion instabilities. Both the B factories as well as the LHC have demonstrated transverse damping times on the order of 10 turns, which gives a measure of the maximum undamped growth rate allowable.

At LEP the transverse mode coupling instability at injection limited the achievable bunch intensity. By contrast, at FCC-ee the beam is always at full collision energy.

2.8.12 Polarization and Energy Calibration

Scaling from LEP some natural transverse polarization due to the Sokolov-Ternov effect is expected up to the W threshold (80 GeV / beam) or above. In this energy range resonant depolarization of a few dedicated non-colliding bunches will provide an exquisite measurement of the average beam energy [24]. Extrapolation to the beam

energy at the IPs, taking into account the energy sawtooth as well as possible beam-beam effects, may lead to some systematic uncertainties. For higher beam energy and as a cross-check other techniques, such as Compton backscattering schemes and also measuring the spin precession of an injected polarized beam [25], are being considered. These techniques would also allow for a cross calibration.

The potentially harmful effect of an orbit kink on the polarization and on the vertical emittance can be avoided by a special orbit inclination technology [26]: Twists between arc segments match the horizontal plane of oscillations with the bending planes of the segments. Spin matching is provided by weak solenoids which produce roughly half of the full twist. The other half of the twist is obtained from a unity/minus-unity insertion appropriately rotated around the longitudinal axis [26].

2.8.13 Conclusions and Outlook

Over the past years the optics development and beam dynamics studies for FCC-ee have made great progress. A double ring collider with crab waist collisions promises superb performance over a large range of beam energies, and allows for an elegant staging.

The primary design challenges arise from the tight focusing, the large energy acceptance required, the wide range of beam parameters and beam energies to be accommodated, severe constraints on the final-focus synchrotron radiation, the effects of the detector solenoids and their compensation, polarization issues, and the required compatibility with the layout of the FCC-hh hadron collider.

We expect to arrive at a complete design, meeting all constraints, by the end of 2016.

2.8.14 Acknowledgements

2.8.15 References

1. J. Wenninger et al., "Future Circular Collider Study — Lepton Collider Parameters," FCC-ACC-SPC-0003 rev. 2.0 (2014).
2. A. Bogomyagkov, E. Levichev, and D. Shatilov, "Beam-Beam Effects Investigation and Parameter Optimization for Circular e^+e^- Collider TLEP to study the Higgs Boson," Phys. Rev. ST Accel. Beams 17, 041004 (2014).
3. M. Benedikt, F. Zimmermann, "Outline and Status of the FCC-ee Design Study," this ICFA Newsletter.
4. U. Wienands, "Staging Scenarios for FCC-ee," at Aspen Winter Conference "Exploring the Physics Frontier with Circular Colliders," 31 January 2015.
5. M. Benedikt et al., "Combined Operation and Staging for the FCC-ee Collider," Proc. IPAC'15 Richmond
6. R. Martin et al. "Status of the FCC-ee Interaction Region Design," Proc. IPAC'15.
7. A. Bogomyagkov et al., Interaction Region of the Future Electron-Positron Collider FCC-ee," Proc. IPAC'15 Richmond.
8. H. Burkhardt, "Synchrotron Radiation in Interaction Region + Comment on BBREM

(Rad. Bhabha) Lifetime," FDCC Week 2015, Washington http://indico.cern.ch/event/340703/session/25/contribution/15#preview:919299

9. H. Burkhardt, M. Boscolo, "Tools for Flexible Optimisation of IR Designs with Application to FCC," Proc. IPAC'15 Richmond.

10. K. Oide, "Final Focus System with Odd-Dispersion Scheme," Proc. 5th International Conference on High-Energy Accelerators, Hamburg, Germany, 20 - 24 Jul 1992, pp.861-863 and KEK-92-58 (1992).

11. V. Telnov, "Restriction on the energy and Luminosity of e^+e^- Storage Rings due to Beamstrahlung," Phys.Rev.Lett 110, 114801 (2013).

12. F. Barbarin, F.C. Iselin, J.M. Jowett, "Particle Dynamics in LEP at Very High Energy," Proc. 4th European Particle Accelerator Conference, London, UK, 27 Jun - 1 Jul 1994, pp.193-195

13. K. Yokoya, "Scaling of High-Energy e+e- Ring Colliders," KEK Accelerator Seminar, 15 March 2012.

14. K. Ohmi, F. Zimmermann, "FCC-ee/CepC Beam-Beam Simulations with Beamstrahlung," Proc. IPAC2014, p. 3766.

15. R. Assmann, K. Cornelis, "The Beam-Beam Interaction in the Presence of Strong Radiation Damping," Proc. EPAC2000 Vienna, p. 1187.

16. D. Shatilov, "Beam-Beam Effects in High-Energy Colliders: Crab Waist vs. Head-On," Proc. ICFA HF2014, 9–12 October 2014, Beijing (2014); and private communication (2015).

17. A. Blondel, F. Zimmermann, "A High. Luminosity e+e- Collider in the LHC tunnel to study the Higgs Boson," CERN-OPEN-2011-047, arXiv:1112.2518v1 (2011).

18. P. Collier, Synchrotron Phase Space Injection into LEP, Proc. 16th Biennial Particle Accelerator Conference and International Conference on High-Energy Accelerators, Dallas, TX, USA, 1 - 5 May 1995, pp.551-553

19. P. Baudrenghien, P. Collier, "Double Batch Injection into LEP," Proc. 5th European Particle Accelerator Conference, Sitges, Barcelona, Spain, 10 - 14 Jun 1996, pp.415-417

20. M. Aiba et al., "Top-Up Injection for FCC-ee," CERN-ACC-2015-065 (2015).

21. J. Jowett, "Feasibility of a Monochromator Scheme in LEP," LEP Note 544 (1985).

22. A. Faus-Golfe, J. Le Duff, "Versatile DBA and TBA lattices for a Tau-Charm Factory with and without Beam Monochromatization, Nuclear Inst. and Methods in Physics Research, A, Volume 372, Issue 1 (1996) p. 6-18

23. M. Migliorati, "Impedance and Collective Effects," FCC Week 2015, Washington http://indico.cern.ch/event/340703/session/81/contribution/158/material/slides/0.pdf

24. U. Wienands, "Is polarization possible at TLEP?," 4th TLEP workshop, CERN, 4-5 April 2013, http://indico.cern.ch/event/240814/timetable/#20130405

25. I.A. Koop, "Scenario for Precision Beam Energy Calibration in FCC-ee," CERN-ACC-2015-081 (2015).

26. I.A. Koop, "Mitigating the Effect of an Orbit Kink on Vertical Emittance and Polarization," CERN-ACC-2015-090 (2015).

3 Workshop and Conference Reports

3.1 Summary Report of the ICFA Mini-workshop on High Field Magnets for pp Colliders

Qingjin Xu

IHEP, Beijing 100049, China

Mail to: xuqj@ihep.ac.cn

Motivated by the upcoming needs of the 20-T level accelerator magnets for recently proposed circular pp colliders, an ICFA mini-workshop on high field magnets has been held in Shanghai China from June 14th (Sunday) to 17th (Wednesday), with more than 50 participants from worldwide labs and industries. Totally 8 sessions were arranged from Monday morning to Tuesday afternoon: 4 of them focused on superconducting accelerator magnets, 3 on superconducting materials, and the last one was roundtable discussion for conclusions and outlook. A technical tour to SSTC (Shanghai Superconductor Technology Co., Ltd.) was arranged on Wednesday.

The 4 sessions on superconducting accelerator magnets started with a welcome address given by Yifang Wang (Director of IHEP, Beijing), followed by overview and preliminary design study of the CEPC-SppC project given by Qing Qin (Deputy director of IHEP) and Jingyu Tang (IHEP). GianLuca Sabbi (LBNL) gave the first talk on magnet technology, reviewed the development history and present status of the superconducting accelerator magnets. Robert Palmer (BNL) presented a cost model for high field accelerator magnets to optimize the total cost of the 100 TeV pp collider. Daniel Dietderich (LBNL) summarized the conductor requirements from high field magnet designers. Xiaorong Wang and Daniel Dietderich (LBNL), Ramesh Gupta (BNL), Tengming Shen (FNAL), Honghai Song (MSU), Yunfei Tan (CHMFL) and Wei Wu (IMP) presented the main R&D activities on superconducting magnets at each laboratory.

The last session on Monday was devoted to SppC magnets: Qingjin Xu (IHEP) gave a talk introducing the preliminary R&D plan and design study of the SppC 20-T magnets. Ramesh Gupta (BNL) and Xiaorong Wang (LBNL) presented 20-T dipole design with common coil configuration and block coil configuration respectively. Kai Zhang (IHEP) and (Yinan Hu) presented mechanical design study and quench protection study for 20-T level superconducting magnets.

The first 3 sessions on Tuesday focused on advanced superconducting materials for high field magnets: Nb_3Sn, Bi-2212, ReBCO and MgB_2. Xuan Peng (Hyper Tech) reviewed history and recent progress of the Nb_3Sn superconductors. Xiaguang Sun (WST) introduced development status of Nb_3Sn wires at WST. Xifeng Pan(NIN), Akiyasu YAMAMOTO (U. Tokyo) and Xuan Peng (Hyper Tech) presented MgB_2 development for accelerator and medical applications. Eric Hellstrom (FSU) reviewed history and recent progress of the Bi-2212 superconductors. Zhenghe Han (THU), Tengming Shen (FNAL) and Peng Song (THU) presented their Bi-2212 related R&D experiences. Yijie Li (SJTU) introduced progress of ReBCO coated conductor program at SJTU and SSTC. Guilin Cui (Furukawa) presented latest technology and manufacturing Innovations at SuperPower. Valery PETRYKIN (SuperOX Japan) gave an overview of 2G-HTS wire production at SuperOX Japan. Yi Li (THU) presented

study of flux motion and electromagnetic performance in HTS magnets. The last talk of the workshop was given by Zhiyong Hong (SSTC) about a general introduction to SSTC and its future strategy.

The round table discussion was chaired by Weiren Chou (FNAL) and the main topics focused on cost and size of 20-T level accelerator magnets. The cost of superconductors is expected to be largely reduced in future, i.e., for ReBCO superconductors, people are expecting to reduce its price to 1/10 of the present level in 10 years, and the performance of superconductors is expected to be improved, i.e., the critical current density (J_c) of Nb$_3$Sn/BiSSCO round wires and ReBCO tapes will very possibly be tripled or even more in 10 years. The size of the SppC magnets has been limited to 900 mm in the CEPC-SppC Pre-CDR, to be put into the 1.5-m diameter cryostat, assuming the tunnel width is 6 m and CEPC accelerator will not be removed during SppC construction. Magnet designers at the workshop had an excited discussion about the possibility of the 20-T twin-aperture magnets with 900-mm diameter. Some think 900mm is feasible and others think more space is needed to contain the large forces of the 20-T magnets. Both sides agree more detailed conceptual design is necessary to answer this question. Also, there is a suggestion to just enlarge the left side of the tunnel where the dipole would be placed, instead of changing the whole diameter of the tunnel, or to change the shape of the tunnel cross section, with lowering ceiling and raising width, i.e., from present 6 m to 6.5 m or 7 m, without changing its area. There are also some discussions about different coil configurations for high field dipole magnets. SppC chose common coil configuration as its starting point for the preliminary design study; the other configurations would still be candidates for R&D in future.

All presentations of the workshop are available for downloading on the following website: http://indico.ihep.ac.cn/event/4900/timetable/#all.detailed.

2015 ICFA MINI-WORKSHOP ON HIGH FIELD MAGNETS FOR PP COLLIDERS
June 14-17th, 2015   Shanghai, China

Organizer:Insitute of High Energy Physics Chinese Academy of Sciences
Co-organizer:Shanghai Superconductor Technology Co., Ltd.

4 Forthcoming Beam Dynamics Events

4.1 The 9th International Accelerator School for Linear Colliders

The 9th International Accelerator School for Linear Colliders will take place at the **Delta Whistler Village Suites, Whistler, British Columbia, Canada from October 26 to November 6, 2015**. (http://www.linearcollider.org/school/2015/) The school will offer three parallel courses: linear collider beam physics, linear collider technology, and XFEL. The third one is a new addition to the school. We have recruited a group of best known experts in this field to teach these courses. Attached below is a list of teachers and an updated curriculum.

From more than 100 applications, the school admitted 49 students from around the world (18 from Asia, 9 from North America and 22 from Europe). But several of them will be unable to attend due to personal reason or problems to obtain a visa to enter Canada. The student list can be found on the school web site.

In addition to lectures, there will be homework sessions as well as a final exam. All lecture slides will be made available online. There will also be a site visit to TRIUMF, where the students will see real accelerators and learn how to make them work in a control room.

Lecturers of the 2015 LC Accelerator School (v4)

Topic	Lecture	Lecturer
Introduction	I1	Daniel Schulte (CERN)
ILC	I2	Masao Kuriki (Hiroshima U.)
CLIC	I3	Frank Tecker (CERN)
XFEL	I4	Claudio Pellegrini (UCLA)
Linac basics	AB1	Daniel Schulte (CERN)
Instrumentation basics	AB2	Hermann Schmickler (CERN)
Linac	A1	Daniel Schulte (CERN)
Sources	A2	Masao Kuriki (Hiroshima U.)
Damping rings	A3	Yannis Papaphillipou (CERN)
Beam delivery & beam-beam	A4	Andrei Seryi (John Adams Inst.)
Room temperature RF	B1	Walter Wuensch (CERN)
Superconducting RF	B2	Takayuki Saeki (KEK)
Instrumentation	B3	Hermann Schmickler (CERN)
LLRF & high power RF	B4	Themis Mastoridis (CalPoly)
XFEL theory	C1	Zhirong Huang (SLAC) Panos Baxevanis (Stanford U.)
XFEL beam physics	C2	Tor Raubenheimer (SLAC)
Superconducting RF	C3a	Takayuki Saeki (KEK)
Room temperature RF	C3b	Walter Wuensch (CERN)
Instrumentation	C3c	Hermann Schmickler (CERN)
Undulators	C3d	Efim Gluskin (ANL)
Seeding lasers	C3e	Stephen Milton (CSU)
Final exam coordinator		Kaoru Yokoya (KEK)

Ninth International Accelerator School for Linear Colliders – Curriculum (v8, 10/11/2015)

26 October – 6 November, 2015, Delta Whistler Village Suites, Whistler, BC, Canada

Daily Schedule

Breakfast   07:30 – 09:00
Morning   09:00 – 12:30, including ½-hour break
Lunch   12:30 – 14:00
Afternoon   14:00 – 17:30, including ½-hour break
Tutorial & homework   17:30 – 18:30
Dinner   19:00 – 20:00
Tutorial & homework   20:00 – 22:00

List of Courses (black: required, red, blue and purple: elective)

	Morning	Afternoon	Evening
Mon 26 Oct		Arrival, registration	Reception
Tues 27 Oct	Introduction to science, ILC and CLIC		Tutorial & homework
Wed 28 Oct	Introduction to science and XFEL	Joint lecture: Linac basics	Tutorial & homework
Thurs 29 Oct	Joint lecture: Instrumentation basics	Course A: Linear collider physics Course B: Linear collider technology Course C: XFEL physics & technology	Tutorial & homework
Fri 30 Oct	Excursion: TRIUMF site visit and Vancouver sightseeing		Tutorial & homework
Sat 31 Oct	Course A: Linear collider physics Course B: Linear collider technology Course C: XFEL physics & technology	Course A: Linear collider physics Course B: Linear collider technology Course C: XFEL physics & technology	Tutorial & homework
Sun 1 Nov	Course A: Linear collider physics Course B: Linear collider technology Course C: XFEL physics & technology	Course A: Linear collider physics Course B: Linear collider technology Course C: XFEL physics & technology	Tutorial & homework
Mon 2 Nov	Course A: Linear collider physics Course B: Linear collider technology Course C: XFEL physics & technology	Course A: Linear collider physics Course B: Linear collider technology Course C: XFEL physics & technology	Tutorial & homework
Tues 3 Nov	Course A: Linear collider physics Course B: Linear collider technology Course C: XFEL physics & technology	Course A: Linear collider physics Course B: Linear collider technology Course C: XFEL physics & technology	Tutorial & homework
Wed 4 Nov	Course A: Linear collider physics Course B: Linear collider technology Course C: XFEL physics & technology	Joint session with LCWS	Tutorial & homework
Thurs 5 Nov	Course A: Linear collider physics Course B: Linear collider technology Course C: XFEL physics & technology	Study time	Study time
Fri 6 Nov	Final exam	Free time	Banquet; Student Award Ceremony
Sat 7 Nov	Departure		

Program

	Tuesday, 27 October	Wednesday, 28 October	Thursday, 29 October	Friday, 30 October
Morning 09:00 – 12:30	**Welcome –** *S Kościelniak (TRIUMF)* **Introduction –** *W Chou (Fermilab)* **Lecture I1 – Introduction to linear colliders (1.5 hrs)** *Daniel Schulte (CERN)* **Lecture I2 – ILC (3 hrs)** *Masao Kuriki (Hiroshima Univ.)*	**Lecture I4 – Introduction to XFEL (3 hrs)** *Claudio Pellegrini (SLAC/UCLA)*	**Joint lecture AB2 –Instrumentation basics (3 hrs)** *Hermann Schmickler (CERN)*	Excursion: (08:00 – 19:00) TRIUMF site visit Vancouver sightseeing
Afternoon 14:00 – 17:30	**Lecture I2 – ILC** (cont'd) *Masao Kuriki (Hiroshima Univ.)* **Lecture I3 – CLIC** **(1.5 hrs)** *Frank Tecker (CERN)*	**Joint lecture AB1 – Linac basics (3 hrs)** *Daniel Schulte (CERN)*	**Lecture A1 – Linac (9 hrs)** *Daniel Schulte (CERN)* **Lecture B1 – NC RF (9 hrs)** *Walter Wuensch (CERN)* **Lecture C1 – XFEL theory (6 hrs)** *Zhirong Huang & Panos Baxevanis (SLAC)*	
Evening 19:00 – 22:00	Tutorial & homework	Tutorial & homework	Tutorial & homework	Tutorial & homework

Program (cont'd)

	Saturday, 31 October	Sunday, 1 November	Monday, 2 November	Tuesday, 3 November
Morning 09:00 – 12:30	Lecture A1 – Linac (cont'd) Daniel Schulte (CERN) Lecture B1 – NC RF (cont'd) Walter Wuensch (CERN) Lecture C1 – XFEL theory (cont'd) Zhirong Huang & Panos Baxevanis (SLAC)	Lecture A2 – Sources (6 hrs) Masao Kuriki (Hiroshima Univ.) Lecture B2 & C3a – SC RF (12 hrs / 6 hrs) Takayuki Saeki (KEK)	Lecture A3 – Damping rings (12 hrs) Yannis Papaphilippou (CERN) Lecture B2 – SC RF (cont'd) Takayuki Saeki (KEK) Lecture C3b – NC RF (6 hrs) Walter Wuensch (CERN)	Lecture A3 – Damping rings (cont'd) Yannis Papaphilippou (CERN) Lecture B3 & C3e – Instrumentation (6 hrs) Hermann Schmickler (CERN)
Afternoon 14:00 – 17:30	Lecture A1 – Linac (cont'd) Daniel Schulte (CERN) Lecture B1 – NC RF (cont'd) Walter Wuensch (CERN) Lecture C2 – XFEL beam physics (3 hrs) Tor Raubenheimer (SLAC)	Lecture A2 – Sources (cont'd) Masao Kuriki (Hiroshima Univ.) Lecture B2 & C3a – SC RF (cont'd) Takayuki Saeki (KEK)	Lecture A3 – Damping rings (cont'd) Yannis Papaphilippou (CERN) Lecture B2 – SC RF (cont'd) Takayuki Saeki (KEK) Lecture C3b – NC RF (cont'd) Walter Wuensch (CERN)	Lecture A3 – Damping rings (cont'd) Yannis Papaphilippou (CERN) Lecture B3 & C3e – Instrumentation (cont'd) Hermann Schmickler (CERN)
Evening 19:00 – 22:00	Tutorial & homework	Tutorial & homework	Tutorial & homework	Tutorial & homework

	Wednesday, 4 November	Thursday, 5 November	Friday, 6 November	Saturday, 7 November
Morning 09:00 – 12:30	Lecture A4 – BDS & beam-beam (6 hrs) Andrei Seryi (John Adams Inst.) Lecture B4 – LLRF (6 hrs) Themis Mastoridis (CalPoly) Lecture C3d – Undulators (3 hrs) Efim Gluskin (ANL)	Lecture A4 – BDS & beam-beam (cont'd) Andrei Seryi (John Adams Inst.) Lecture B4 – LLRF (cont'd) Themis Mastoridis (CalPoly) Lecture C3e – Seeding lasers (3 hrs) Stephen Milton (CSU)	08:00 – 12:30 Final exam (4.5 hrs)	Departure
Afternoon 14:00 – 17:30	Joint session with LCWS (13:30 – 18:00)	Study time	Free time	
Evening 19:00 – 22:00	Tutorial & homework	Study time	Banquet at 19:00; Student Award Ceremony	

Notes on the Program:

1. There are a total of 11 school days in this year's program, excluding the arrival day (October 26) and the departure day (November 7). The time is divided as follows: 2-1/2 days for required courses, 5-1/2 days for elective courses, one day for excursion and site visit, 1/2 day for a joint session with the Linear Collider Workshop (LCWS), 1/2 day for study time and a final examination day.
2. The required course consists of six lectures: introduction, ILC, CLIC, XFEL, linac basics and instrumentation basics. Every student must take this course.
3. There are three elective courses: Course A (the red course) is linear collider beam physics, Course B (the blue course) is linear collider technology, and Course C (the purple course) is XFEL beam physics and technology. They will run in parallel. Each student will choose one of these.
4. The linear collider beam physics course consists of lectures on four topics: (1) linac, (2) sources, (3) damping rings, and (4) beam delivery system and beam-beam effects.
5. The linear collider technology course also consists of lectures on four topics: (1) normal conducting RF, (2) superconducting RF, (3) instrumentation, and (4) LLRF and high power RF.
6. The XFEL course is a new addition to this year's school. It has three parts: (1) FEL theory, (2) FEL beam physics, and (3) FEL technology, which consists of five lectures: NC RF, SRF, instrumentation, undulators and seeding lasers.
7. There will be homework assignments, but homework is not counted in the grade. There will be a final examination. Some of the exam problems will be taken from variations of the homework assignments. The exam papers will be graded immediately after the exam and results announced in the evening of November 6 at the student award ceremony.
8. There is a tutorial and homework period every evening. It is part of the curriculum and students are required to attend. Lecturers will be available in the evening of their lecture day during this period.
9. Lecturers have been asked to cover the basics as well as possible. Their teaching material will be made available online to the students ahead of time. Students are strongly encouraged to study this material prior to the beginning of the school.
10. Lecturers of the elective courses are required to provide lecture syllabus as soon as possible in order to help students make their selection.
11. All lecturers are responsible for the design of homework and exam problems as well as the answer sheet. They are also responsible for grading the exams.
12. The award ceremony will honor the top (~10) students based on their exam scores.

5 Announcements of the Beam Dynamics Panel

5.1 ICFA Beam Dynamics Newsletter

5.1.1 Aim of the Newsletter

The ICFA Beam Dynamics Newsletter is intended as a channel for describing unsolved problems and highlighting important ongoing works, and not as a substitute for journal articles and conference proceedings that usually describe completed work. It is published by the ICFA Beam Dynamics Panel, one of whose missions is to encourage

international collaboration in beam dynamics.

Normally it is published every April, August and December. The deadlines are 15 March, 15 July and 15 November, respectively.

5.1.2 Categories of Articles

The categories of articles in the newsletter are the following:
1. Announcements from the panel.
2. Reports of beam dynamics activity of a group.
3. Reports on workshops, meetings and other events related to beam dynamics.
4. Announcements of future beam dynamics-related international workshops and meetings.
5. Those who want to use newsletter to announce their workshops are welcome to do so. Articles should typically fit within half a page and include descriptions of the subject, date, place, Web site and other contact information.
6. Review of beam dynamics problems: This is a place to bring attention to unsolved problems and should not be used to report completed work. Clear and short highlights on the problem are encouraged.
7. Letters to the editor: a forum open to everyone. Anybody can express his/her opinion on the beam dynamics and related activities, by sending it to one of the editors. The editors reserve the right to reject contributions they judge to be inappropriate, although they have rarely had cause to do so.

The editors may request an article following a recommendation by panel members. However anyone who wishes to submit an article is strongly encouraged to contact any Beam Dynamics Panel member before starting to write.

5.1.3 How to Prepare a Manuscript

Before starting to write, authors should download the template in Microsoft Word format from the Beam Dynamics Panel web site:

http://www-bd.fnal.gov/icfabd/news.html

It will be much easier to guarantee acceptance of the article if the template is used and the instructions included in it are respected. The template and instructions are expected to evolve with time so please make sure always to use the latest versions.

The final Microsoft Word file should be sent to one of the editors, preferably the issue editor, by email.

The editors regret that LaTeX files can no longer be accepted: a majority of contributors now prefer Word and we simply do not have the resources to make the conversions that would be needed. Contributions received in LaTeX will now be returned to the authors for re-formatting.

In cases where an article is composed entirely of straightforward prose (no equations, figures, tables, special symbols, etc.) contributions received in the form of plain text files may be accepted at the discretion of the issue editor.

Each article should include the title, authors' names, affiliations and e-mail addresses.

5.1.4 Distribution

A complete archive of issues of this newsletter from 1995 to the latest issue is available at

http://icfa-usa.jlab.org/archive/newsletter.shtml.

This is now intended as the primary method of distribution of the newsletter.

Readers are encouraged to sign-up for electronic mailing list to ensure that they will hear immediately when a new issue is published.

The Panel's Web site provides access to the Newsletters, information about future and past workshops, and other information useful to accelerator physicists. There are links to pages of information of local interest for each of the three ICFA areas.

Printed copies of the ICFA Beam Dynamics Newsletters are also distributed (generally some time after the Web edition appears) through the following distributors:

Weiren Chou	chou@fnal.gov	North and South Americas
Rainer Wanzenberg	rainer.wanzenberg@desy.de	Europe[++] and Africa
Toshiyuki Okugi	toshiyuki.okugi@kek.jp	Asia[**] and Pacific

[++] Including former Soviet Union.

[**] For Mainland China, Jiu-Qing Wang (wangjq@mail.ihep.ac.cn) takes care of the distribution with Ms. Su Ping, Secretariat of PASC, P.O. Box 918, Beijing 100039, China.

To keep costs down (remember that the Panel has no budget of its own) readers are encouraged to use the Web as much as possible. In particular, if you receive a paper copy that you no longer require, please inform the appropriate distributor.

5.1.5   Regular Correspondents

The Beam Dynamics Newsletter particularly encourages contributions from smaller institutions and countries where the accelerator physics community is small. Since it is impossible for the editors and panel members to survey all beam dynamics activity worldwide, we have some Regular Correspondents. They are expected to find interesting activities and appropriate persons to report them and/or report them by themselves. We hope that we will have a "compact and complete" list covering all over the world eventually. The present Regular Correspondents are as follows:

Liu Lin	Liu@ns.lnls.br	LNLS Brazil
Sameen Ahmed Khan	Rohelakan@yahoo.com	SCOT, Oman
Jacob Rodnizki	Jacob.Rodnizki@gmail.com	Soreq NRC, Israel
Rohan Dowd	Rohan.Dowd@synchrotron.org.au	Australian Synchrotron

We are calling for more volunteers as Regular Correspondents.

5.2 ICFA Beam Dynamics Panel Members

Name	eMail	Institution
Rick Baartman	baartman@lin12.triumf.ca	TRIUMF, 4004 Wesbrook Mall, Vancouver, BC, V6T 2A3, Canada
Marica Biagini	marica.biagini@lnf.infn.it	INFN-LNF, Via E. Fermi 40, C.P. 13, Frascati, Italy
John Byrd	jmbyrd@lbl.gov	Center for Beam Physics, LBL, 1 Cyclotron Road, Berkeley, CA 94720-8211, U.S.A.
Yunhai Cai	yunhai@slac.stanford.edu	SLAC, 2575 Sand Hill Road, MS 26 Menlo Park, CA 94025, U.S.A.
Swapan Chattopadhyay	swapan@fnal.gov	Northern Illinois University, Dept. of Physics, DeKalb, Illinois, 60115, U.S.A.
Weiren Chou (Chair)	chou@fnal.gov	Fermilab, MS 220, P.O. Box 500, Batavia, IL 60510, U.S.A.
Wolfram Fischer	wfischer@bnl.gov	Brookhaven National Laboratory, Bldg. 911B, Upton, NY 11973, U.S.A.
Yoshihiro Funakoshi	yoshihiro.funakoshi@kek.jp	KEK, 1-1 Oho, Tsukuba-shi, Ibaraki-ken, 305-0801, Japan
Jie Gao	gaoj@ihep.ac.cn	Institute for High Energy Physics, P.O. Box 918, Beijing 100039, China
Ajay Ghodke	ghodke@cat.ernet.in	RRCAT, ADL Bldg. Indore, Madhya Pradesh, 452 013, India
Ingo Hofmann	i.hofmann@gsi.de	High Current Beam Physics, GSI Darmstadt, Planckstr. 1, 64291 Darmstadt, Germany
Sergei Ivanov	sergey.ivanov@ihep.ru	Institute for High Energy Physics, Protvino, Moscow Region, 142281 Russia
In Soo Ko	isko@postech.ac.kr	Pohang Accelerator Lab, San 31, Hyoja-Dong, Pohang 790-784, South Korea
Elias Metral	elias.metral@cern.ch	CERN, CH-1211, Geneva 23, Switzerland
Yoshiharu Mori	mori@rri.kyoto-u.ac.jp	Research Reactor Inst., Kyoto Univ. Kumatori, Osaka, 590-0494, Japan
George Neil	neil@jlab.org	TJNAF, 12000 Jefferson Ave., Suite 21, Newport News, VA 23606, U.S.A.
Toshiyuki Okugi	toshiyuki.okugi@kek.jp	KEK, 1-1 Oho, Tsukuba-shi, Ibaraki-ken, 305-0801, Japan
Mark Palmer	mapalmer@fnal.gov	Fermilab, MS 221, P.O. Box 500, Batavia, IL 60510, U.S.A.
Chris Prior	chris.prior@stfc.ac.uk	ASTeC Intense Beams Group, STFC RAL, Chilton, Didcot, Oxon OX11 0QX, U.K.
Yuri Shatunov	Yu.M.Shatunov@inp.nsk.su	Acad. Lavrentiev, Prospect 11, 630090 Novosibirsk, Russia
Jiu-Qing Wang	wangjq@ihep.ac.cn	Institute for High Energy Physics, P.O. Box 918, 9-1, Beijing 100039, China
Rainer Wanzenberg	rainer.wanzenberg@desy.de	DESY, Notkestrasse 85, 22603 Hamburg, Germany

The views expressed in this newsletter do not necessarily coincide with those of the editors.
The individual authors are responsible for their text.